

Measurement of Cross Sections and Leptonic Forward-Backward Asymmetries at the Z Pole and Determination of Electroweak Parameters

The L3 Collaboration

Abstract

We report on the measurement of the leptonic and hadronic cross sections and leptonic forward-backward asymmetries at the Z peak with the L3 detector at LEP. The total luminosity of 40.8 pb^{-1} collected in the years 1990, 1991 and 1992 corresponds to $1.09 \cdot 10^6$ hadronic and $0.98 \cdot 10^5$ leptonic Z decays observed. These data allow us to determine the electroweak parameters. From the cross sections we derive the properties of the Z boson:

$$m_Z = 91195 \pm 9 \text{ MeV} \quad \Gamma_Z = 2494 \pm 10 \text{ MeV}$$

$$\Gamma_{\text{had}} = 1748 \pm 10 \text{ MeV} \quad \Gamma_\ell = 83.49 \pm 0.46 \text{ MeV},$$

assuming lepton universality. We obtain an invisible width of $\Gamma_{\text{inv}} = 496.5 \pm 7.9 \text{ MeV}$ which, in the Standard Model, corresponds to a number of light neutrino species of $N_\nu = 2.981 \pm 0.050$.

Using also the three leptonic forward-backward asymmetries and the average tau polarization, we determine the effective vector and axial-vector coupling constants of the neutral weak current to charged leptons to be:

$$\bar{g}_V^\ell = -0.0378_{-0.0042}^{+0.0045} \quad \bar{g}_A^\ell = -0.4998 \pm 0.0014.$$

Within the framework of the Standard Model, and including our measurements of the $Z \rightarrow b\bar{b}$ forward-backward asymmetry and partial decay width, we derive an effective electroweak mixing angle of $\sin^2 \bar{\theta}_W = 0.2326 \pm 0.0012$. We obtain an estimate for the strong coupling constant, $\alpha_s = 0.142 \pm 0.013$, and for the top-quark mass, $m_t = 158_{-40}^{+32} \pm 19$ (Higgs) GeV, where the second error arises due to the uncertainty in the Higgs-boson mass.

(Submitted to *Zeitschrift für Physik C*)

1 Introduction

In 1992, the LEP e^+e^- collider at CERN ran at the center-of-mass energy 91.29 GeV, where the cross section for Z-boson production in e^+e^- annihilation is maximum. A total luminosity of 22.4 pb^{-1} was recorded with the L3 detector at LEP corresponding to 678,000 hadronic and 59,000 leptonic Z decays selected.

In this article we report on the measurements of the reactions:

1. $e^+e^- \rightarrow \text{hadrons}(\gamma)$,
2. $e^+e^- \rightarrow \mu^+\mu^-(\gamma)$,
3. $e^+e^- \rightarrow \tau^+\tau^-(\gamma)$,
4. $e^+e^- \rightarrow e^+e^-(\gamma)$,

where the (γ) indicates the presence of radiative photons. These measurements are used to determine the parameters of the Standard Model (SM) [1, 2].

Earlier measurements of the reactions 1–4 have been reported by the LEP experiments [3–5]. The inclusion of the 1992 data doubles the peak event sample. Detailed studies are performed with this large sample of events with the aim of decreasing the systematic errors. These studies allow us to exploit the full statistical accuracy of our data.

Since the data analysis is improved compared to our earlier work of the years 1990 and 1991 [3, 4], we also reanalyze that data. Here we present the results derived from the data collected by L3 in the years 1990, 1991 and 1992, which correspond to a total luminosity of 40.8 pb^{-1} , or $1.09 \cdot 10^6$ hadronic and $0.98 \cdot 10^5$ leptonic Z decays observed.

The organization of this article is: in Section 2 we briefly describe the L3 detector. The measurement of luminosity is discussed in Section 3. Section 4 presents the analysis of the reactions 1–4. Our results on the leptonic and hadronic cross sections and leptonic forward-backward asymmetries are given in Section 5. The determination of the electroweak parameters is described in Section 6. A summary and conclusion are given in Section 7.

2 The L3 Detector

The L3 detector [6] is designed to measure the energy and direction of leptons, photons and jets with high precision. The detector consists of a central tracking chamber (TEC), a high resolution electromagnetic calorimeter composed of bismuth germanate crystals (BGO), a cylindrical array of scintillation counters (SCNT), a uranium and brass hadron calorimeter with proportional wire chamber readout (HCAL), and a precise muon spectrometer (MUCH). All elements are installed inside a magnet of 12 m diameter, which provides a uniform field of 0.5 T along the beam direction.

In the L3 detector e^+e^- interactions are recorded based on several independent triggers [6]. The trigger decisions are derived from the energy depositions in the calorimeters, tracks in the central tracking chamber or the muon spectrometer, or from multiple hits in the scintillation counters. The decays of the Z into hadrons or charged leptons usually fulfill at least two trigger requirements which allows us to determine the individual and combined trigger efficiencies.

The response of the L3 detector is modeled with the GEANT 3.15 [7] detector simulation program which includes the effects of energy loss, multiple scattering and showering in the detector materials and in the beam pipe. Hadronic showers are simulated with the GHEISHA 8 [8] program.

3 Measurement of Luminosity

The total luminosity, \mathcal{L} , is determined by measuring the number of small-angle Bhabha scatterings, $e^+e^- \rightarrow e^+e^-(\gamma)$. For this purpose two cylindrical calorimeters with an inner radius of 68.2 mm and an outer radius of 191.4 mm are located on either side of the interaction point at $z = \pm 2.7$ m. Each is a finely segmented and azimuthally symmetric array of 304 BGO crystals which is split in the vertical plane.

Event Selection

The Bhabha event selection is based on the energy depositions in adjacent crystals of the two calorimeters which are grouped to form clusters. The selection criteria are:

1. One cluster is required to have the reconstructed radial (R) and azimuthal (ϕ) impact coordinates, determined in the plane transverse to the beam, more than one crystal size away from the calorimeter edges:

- a) $84.4 < R < 176.2$ mm
- b) $|\phi - 90^\circ| > 11.25^\circ$ and $|\phi - 270^\circ| > 11.25^\circ$.

We impose no restrictions on the reconstructed impact coordinates on the opposite side.

2. The reconstructed energy on one side, E_{\max} , must be greater than $0.8E_{\text{beam}}$, and that on the other side must be greater than $0.4E_{\text{beam}}$, where E_{beam} is the energy of the e^+e^- beams in LEP.
3. The coplanarity angle between the two clusters, $\Delta\phi$, corrected for the bending of the particle trajectory in the magnetic field, must satisfy $|\Delta\phi - 180^\circ| < 10^\circ$.

Figure 1 shows the distributions of the average radial impact coordinate, R , and the maximum energy, E_{\max} , comparing the data to fully simulated Monte-Carlo events.

Two samples of Bhabha events are maintained. In the first (second) sample, the tight fiducial volume cut is imposed on the cluster on the $+z$ ($-z$) side. The average of the two samples is used to calculate the luminosity. This procedure greatly reduces the systematic effects on the luminosity measurement due to calorimeter misalignments and e^+e^- interaction point displacements. The asymmetric energy cut ensures that the acceptance is not sensitive to detector inefficiencies. In addition, most of the radiative Bhabha events are retained. Almost all the background from random beam-gas coincidences has an energy less than $0.8E_{\text{beam}}$ in each calorimeter and is therefore substantially reduced by the energy requirement.

The coplanarity requirement is used to further suppress beam related background. The remaining background in the signal region is subtracted separately for each LEP fill, using the sidebands of the coplanarity distribution, $10^\circ < |\Delta\phi - 180^\circ| < 30^\circ$, after imposing the requirement that the energy on neither side is within 5% of E_{beam} [3]. The residual background level of 0.1% is mainly due to random coincidences of beam-gas interactions.

Theoretical Cross Section

To determine the visible cross section, $e^+e^- \rightarrow e^+e^-(\gamma)$ events are simulated at a fixed center-of-mass energy, \sqrt{s} , of 91.18 GeV using the event generator BHLUMI 2.01 [9, 10]. For center-of-mass energies, $\sqrt{s'}$, off the Z peak, the visible cross section is rescaled by s/s' . The event

generator BABAMC [11] is used to include missing electroweak corrections. A contribution of 0.02% from the process $e^+e^- \rightarrow \gamma\gamma(\gamma)$ is taken into account [12].

Including all contributions, the visible cross section at the Z peak is 90.3 nb for 1992, 90.7 nb for 1991 and 84.7 nb for 1990. The differences are due to shifts in the detector position along the beam axis. Inside our angular acceptance the theoretical error on the Bhabha cross section is estimated to be 0.25% [10, 13].

Luminosity Determination

The selection quantities show good agreement between the data and the Monte-Carlo prediction (Figure 1). The small excess of data events at high energies in the energy distribution is due to real Bhabha interactions contaminated with a spurious beam-gas interaction. Studying the effect of changes in the selection requirements on the total luminosity, we assign a systematic error of 0.3% on the luminosity due to event selection.

Radiative Bhabha events are used to investigate the quality of the Monte-Carlo event generator. The photon is identified as the smaller energy cluster in events with two separate clusters on the same side. Figure 2 shows the distribution of the measured energy, E_γ , of the photon candidates, and the Monte Carlo prediction. The agreement is good.

The geometry and position of the calorimeters is measured to an accuracy of 0.2 mm except for the position along the beam axis which is surveyed with an accuracy of 0.5 mm. This results into a systematic uncertainty of 0.4% on the luminosity.

The luminosity trigger is described in detail in [3, 6]. The trigger inefficiency is found to be negligible for the selected event sample. The contributions to the systematic error on the luminosity measurement are summarized in Table 1. Combining them in quadrature we assign a systematic error of 0.6% to the measured total luminosity.

Source of Systematic Uncertainty	Contribution to $\delta\mathcal{L}/\mathcal{L}$ [%]
Selection Cuts	0.3
Monte Carlo Statistics	0.1
Geometry of the Calorimeters	0.4
Background Subtraction	negligible
Trigger Inefficiency	negligible
Total Experimental Systematic Uncertainty	0.5
Theoretical Systematic Uncertainty	0.25
Total Systematic Uncertainty	0.6

Table 1: Systematic uncertainties on the luminosity measurement.

4 Analysis of Z Decays

We analyze all the visible Z decays by measuring the reactions $e^+e^- \rightarrow \text{hadrons}(\gamma)$, $e^+e^- \rightarrow \mu^+\mu^-(\gamma)$, $e^+e^- \rightarrow \tau^+\tau^-(\gamma)$, and $e^+e^- \rightarrow e^+e^-(\gamma)$. Below we describe the event selection applied to the 1991 and 1992 data and the determination of the total cross sections and forward-

backward asymmetries. The selection criteria for the 1990 data differ slightly [3], as the end-cap electromagnetic calorimeter was added in 1991.

4.1 $e^+e^- \rightarrow \text{hadrons}(\gamma)$

Event Selection

The selection of the hadronic Z decays is mainly based on calorimetric information. The process is identified by the large amount of energy deposited in the detector, and a high particle multiplicity in the final state. Energy depositions in adjacent cells of the calorimeters are grouped to form clusters [14]. Since a hadronic event contains on average about 40 clusters we easily reject the low-multiplicity leptonic Z decays. The selection criteria are:

1. The total energy observed in the detector, including the momenta of muons measured in the muon spectrometer, E_{vis} , is restricted to the range $0.5 < E_{\text{vis}}/\sqrt{s} < 2.0$.
2. The energy deposited in the hadron calorimeter, E_{had} , must be larger than 2.5 GeV.
3. The energy imbalance along the beam direction, E_{\parallel} , must satisfy $|E_{\parallel}|/E_{\text{vis}} < 0.6$.
4. The transverse energy imbalance, E_{\perp} , must satisfy $E_{\perp}/E_{\text{vis}} < 0.5$.
5. The number of energy clusters, N_{clusters} , reconstructed in the calorimeters is required to satisfy:
 - a) $N_{\text{clusters}} \geq 13$ for $|\cos \theta_t| \leq 0.74$ (event in the barrel region),
 - b) $N_{\text{clusters}} \geq 17$ for $|\cos \theta_t| > 0.74$ (event in the end-cap region),
 where θ_t is the polar angle of the event thrust axis.

Figure 3 shows the distributions of the visible energy, the parallel and perpendicular energy imbalance, and the number of clusters, comparing the data to fully simulated Monte-Carlo events. All cuts except the indicated one have been applied.

Cross Section

The hadron calorimeter covers 99.5% of the full solid angle which results in a selection efficiency for $e^+e^- \rightarrow \text{hadrons}(\gamma)$ events of $(99.19 \pm 0.10)\%$, determined from Monte-Carlo events. The uncertainty on this number is estimated by comparing different fragmentation models as implemented in the Monte-Carlo event generators JETSET 7.3 [15] and HERWIG 5.3 [16].

For all distributions we find a good agreement between the data and the Monte-Carlo prediction, especially in the region of the cut position. The systematic error originating from the event selection estimated by varying the above selection cuts is found to be small, 0.06%. The deviation in the distribution of the number of clusters for $N_{\text{clusters}} > 70$ is attributed to the imperfect simulation of low energy hadrons in the calorimeters. We have verified that the events in this region are hadronic events.

Applying the selection to $e^+e^- \rightarrow \tau^+\tau^-(\gamma)$ events simulated by the KORALZ 3.8 [17] Monte Carlo, we find a background contribution of $(0.20 \pm 0.02)\%$. The background from all other Z decays is negligible. The non-resonant background contribution, e.g., two-photon processes, beam-gas interactions and cosmic rays, is estimated by extrapolating the observed event rate at low visible energy, $0.2 < E_{\text{vis}}/\sqrt{s} < 0.5$, into the signal region. We find a \sqrt{s} -independent

contamination of (35 ± 15) pb. The total background subtraction leads to a systematic error on the cross section of 0.08%.

Hadronic events are triggered by the energy, central track, muon or scintillator multiplicity triggers. The cross section is corrected for the overall trigger inefficiency of $(0.16 \pm 0.03)\%$. The contributions to the systematic error on the cross-section measurement are summarized in Table 2. We assign a systematic error of 0.15% on the total cross section of the reaction $e^+e^- \rightarrow \text{hadrons}(\gamma)$, excluding the error on the luminosity measurement.

The number of selected events and the total cross sections for the different center-of-mass energy points are listed in Table 9 of Section 5. The cross sections are compared to the result of a fit to the complete data set in Figure 13 of Section 6.

Source of Systematic Uncertainty	Contribution to $\delta\sigma_{\text{had}}/\sigma_{\text{had}}$ [%]
Selection Cuts	0.06
Monte-Carlo Acceptance and Efficiency	0.10
Background Subtraction	0.08
Trigger Inefficiency	0.03
Total Systematic Uncertainty	0.15

Table 2: Systematic uncertainties on the total hadron cross section, σ_{had} , excluding the luminosity error.

4.2 $e^+e^- \rightarrow \mu^+\mu^-(\gamma)$

Event Selection

The event selection for the process $e^+e^- \rightarrow \mu^+\mu^-(\gamma)$ requires two identified muons within the fiducial angular region of $|\cos\theta| < 0.8$. In the L3 detector, muons are primarily identified by a track in the muon spectrometer. For particles traversing at least 2 out of the 3 muon chamber layers, the track is reconstructed and its momentum as well as its charge is measured.

Muons are also identified by their minimum ionizing particle (MIP) signature in the inner subdetectors, if less than 2 muon chambers are hit. Including these muons in our sample makes the selection less sensitive to the exact knowledge of the uncertainties in the efficiency and geometry of individual subdetectors. Figure 4 shows a 45 GeV muon with its typical MIP signature in the detector.

A muon candidate is denoted as a MIP, if at least one of the following conditions is fulfilled:

1. A track in the central tracking chamber must point within 5° in azimuth to a cluster in the electromagnetic calorimeter with an energy less than 2 GeV.
2. On a road from the vertex through the barrel hadron calorimeter, at least 5 out of a maximum of 32 cells must be hit, with an average energy of less than 0.4 GeV per cell.
3. A track in the central chamber or a low energy electromagnetic cluster must point within 10° in azimuth to a muon chamber hit.

In addition, both the electromagnetic and the hadronic energy in a cone of 12° half-opening angle around the MIP candidate, corrected for the energy loss of the particle, must be less than 5 GeV.

To reject the background from hadronic Z decays we require each event to have less than 15 energy clusters in the calorimeters. To reduce the cosmic-ray background at least one of the particles should have an associated scintillation counter hit in a time-of-flight corrected time window of ± 3 ns around the beam crossing. Additional cosmic-ray rejection is achieved by requiring one muon to be associated with a central chamber track, which must have a distance of closest approach to the beam axis (DCA) of less than 5 mm. An acollinearity angle cut, $\xi < 40^\circ$, is applied on the directions of the two muons.

To reduce the background from the $\tau^+\tau^-(\gamma)$ final states and two-photon processes, the highest momentum measured in the muon spectrometer, P_{\max} , must exceed $\frac{2}{3}E_{\text{beam}}$. For events without reconstructed tracks in the muon chambers, we make an acollinearity angle cut of $\xi < 5^\circ$ and require two tracks in the central tracking chamber, one of which must have a transverse momentum larger than 3 GeV.

The final event sample consists to 81.8% of events with two tracks in the muon chambers, 11.6% with one reconstructed muon chamber track, and 6.6% of events with both muons identified by their MIP signature. Figure 5 shows the distributions of the $\cos\theta$ of the two muon candidates in an event, the highest momentum reconstructed in the muon spectrometer, and the acollinearity angle, comparing the data to fully simulated Monte-Carlo events.

Cross Section

The efficiency of the selection is determined from $e^+e^- \rightarrow \mu^+\mu^-(\gamma)$ Monte-Carlo events generated with KORALZ to be $(92.64 \pm 0.15)\%$ inside the fiducial volume, where the error is statistical. A systematic error of 0.10% must be added, which reflects the uncertainty in the determination of the subdetector inefficiencies.

The selection quantities show good agreement between the data and the Monte-Carlo prediction (Figure 5). The systematic error due to the event selection is estimated by varying the selection criteria. Significant contributions arise from the cuts on the muon momentum (0.30%) and the polar angle defining the fiducial volume (0.25%).

Using $e^+e^- \rightarrow \tau^+\tau^-(\gamma)$ Monte-Carlo events generated by KORALZ, we determine this background to be $(1.28 \pm 0.08)\%$. The contribution of all other Z decays to the background is negligible. A contribution (0.05%) of the non-resonant $e^+e^- \rightarrow e^+e^-\mu^+\mu^-$ two-photon process [18] is found only for the subsample of events with no reconstructed track in the muon chambers. The sidebands of the DCA distribution for the central chamber tracks in the region from 5 mm to 20 mm are used to determine the cosmic-ray contamination. We estimate the cosmic-ray background for the nominal value of the DCA cut, 5 mm, to be $(0.15 \pm 0.05)\%$.

Dimuon events are triggered by the central track or muon triggers. The trigger inefficiency is negligible for the events with two tracks reconstructed in the muon spectrometer. For the samples of events with one or zero reconstructed muons in the muon chambers, we rely mainly on the charged track trigger. The trigger inefficiency is determined to be $(1.9 \pm 0.5)\%$ and $(8.0 \pm 1.5)\%$, respectively. The cross section is corrected for the overall trigger inefficiency of $(0.75 \pm 0.15)\%$.

The contributions to the systematic error on the cross-section measurement are summarized in Table 3, including the Monte-Carlo extrapolation to the full solid angle. We assign a systematic error of 0.5% on the total cross section of the reaction $e^+e^- \rightarrow \mu^+\mu^-(\gamma)$, excluding the error on the luminosity measurement.

The number of selected events and the total cross sections for the different center-of-mass energy points are listed in Table 10 of Section 5. The cross sections are compared to the result of a fit to the complete data set in Figure 14 of Section 6.

Source of Systematic Uncertainty	Contribution to $\delta\sigma_\mu/\sigma_\mu$ [%]
Selection Cuts	0.39
Monte-Carlo Acceptance and Efficiency	0.25
Background Subtraction	0.11
Trigger Inefficiency	0.15
Total Systematic Uncertainty	0.50

Table 3: Systematic uncertainties on the total dimuon cross section, σ_μ , excluding the luminosity error.

Forward-Backward Asymmetry

The forward-backward asymmetry, A_{fb} , is defined as:

$$A_{\text{fb}} = \frac{\sigma_{\text{f}} - \sigma_{\text{b}}}{\sigma_{\text{f}} + \sigma_{\text{b}}},$$

where σ_{f} (σ_{b}) is the cross section for events with the fermion scattered into the hemisphere which is forward (backward) with respect to the e^- beam direction.

Events with hard initial bremsstrahlung are removed from the sample by requiring that the acollinearity angle of the event is less than 15° . This allows the angular distribution in the region $|\cos\theta| < 0.8$ to be approximated by the lowest-order Born formula:

$$\frac{d\sigma}{d\cos\theta} \propto \frac{3}{8}(1 + \cos^2\theta) + A_{\text{fb}} \cos\theta,$$

where θ is the polar angle of the scattered fermion with respect to the e^- beam direction. A comparison with calculations including higher order corrections, as implemented in the analytical program ZFITTER [19], shows that this approximation in the determination of the asymmetry does not introduce any significant systematic bias.

The asymmetry at a given center-of-mass energy point is determined by a maximum likelihood fit to our data where the likelihood function is defined as the product over the selected events labeled i of the differential cross section evaluated at their respective $\cos\theta_i$ value:

$$L \equiv \prod_i \left(\frac{3}{8}(1 + \cos^2\theta_i) + A_{\text{fb}} \cos\theta_i \right).$$

This method does not require an exact knowledge of the acceptance as a function of the polar angle provided that the acceptance is independent of the muon charge.

For the measurement of the asymmetry we use only those events where at least one muon is reconstructed in the muon spectrometer. From the sample with two reconstructed muons only the events with unlike charges are used. The probability for a reversed assignment of the charges in the event is $(2.5 \pm 0.2) \cdot 10^{-5}$, derived from the number of like sign events. For the events with only one reconstructed muon the probability is $(0.85 \pm 0.14)\%$.

We have studied possible asymmetries in the acceptances for μ^- and μ^+ in the forward or backward hemispheres. The effect of discrepancies in the observed momentum spectra on the measured asymmetry is estimated to be at most 0.0015. Since the asymmetry of Z decays into tau pairs is expected and measured to be close to that of Z decays into muon pairs, the remaining background of tau-pair events does not change the observed muon asymmetry. The influence of the cosmic-ray background is small (0.0010).

The contributions to the systematic error on the asymmetry measurement are summarized in Table 4. We assign an absolute error of 0.002 on the forward-backward asymmetry of the reaction $e^+e^- \rightarrow \mu^+\mu^-(\gamma)$.

The differential cross section, $d\sigma_\mu/d\cos\theta$, of the reaction $e^+e^- \rightarrow \mu^+\mu^-(\gamma)$ for events collected at 91.29 GeV (1992 data) is shown in Figure 6. The result for the forward-backward asymmetry obtained from a fit to this distribution agrees with the result from the maximum-likelihood method. The forward-backward asymmetries for the different center-of-mass energy points are listed in Table 13 of Section 5. The asymmetries are compared to the result of a fit to the complete data set in Figure 17 of Section 6.

Source of Systematic Uncertainty	Contribution to δA_{fb}^μ
Charge Confusion	$0.0022A_{\text{fb}}^\mu$
Acceptance Asymmetries	0.0015
Cosmic-Ray Background	0.0010
Total Systematic Uncertainty	0.0020

Table 4: Systematic uncertainties on the dimuon forward-backward asymmetry, A_{fb}^μ .

4.3 $e^+e^- \rightarrow \tau^+\tau^-(\gamma)$

Event Selection

The visible decay products of a tau form a jet, which consists of either an electron, a muon, a charged hadron or a few highly collimated charged and neutral hadrons. Although there does not exist a unique event signature, the aim is to select $\tau^+\tau^-(\gamma)$ events of all tau decay modes. This is achieved by excluding other final states from a sample of selected Z decays.

Tau pairs are selected within a fiducial volume defined by $|\cos\theta_t| < 0.73$ where the polar angle, θ_t , is given by the thrust axis of the event. The event is required to have at least two jets, corresponding to the two taus, with minimal visible energies of 7 and 3 GeV. The acollinearity angle between the directions of the two highest energy jets, ξ , must be smaller than 14.3° .

High multiplicity hadronic Z decays are removed by requiring less than 13 reconstructed energy clusters in the calorimeters. In addition, there should be no track in the central tracking chamber with an azimuthal angle, $\Delta\phi$, larger than 14.3° with respect to the axis of the nearest jet. In order to reject $e^+e^- \rightarrow e^+e^-(\gamma)$ events, the two highest energy clusters in the electromagnetic calorimeter with an electromagnetic shower shape must have energies below $0.90E_{\text{beam}}$ and $0.65E_{\text{beam}}$. In order to reduce the background of $e^+e^- \rightarrow \mu^+\mu^-(\gamma)$ events, the momentum measured in the muon chambers must be less than $0.9E_{\text{beam}}$ for the highest energy, and $0.4E_{\text{beam}}$ for the second highest energy muon candidate in the event. The requirement of at least 2 GeV of energy deposited in the electromagnetic calorimeter rejects dimuon events,

where the muons are not reconstructed in the muon chambers, as well as minimum ionizing cosmic-ray events. The cosmic-ray background is further reduced by requiring a scintillation counter hit within 2.5 ns of the beam crossing.

Figure 7 shows the distributions of the acollinearity angle between the two jet directions and the largest azimuthal angle between a track in the central chamber and the axis of its nearest jet, comparing the data to fully simulated Monte-Carlo events.

Cross Section

The efficiency of the selection is determined from $e^+e^- \rightarrow \tau^+\tau^-(\gamma)$ Monte-Carlo events generated with KORALZ to be $(78.79 \pm 0.11)\%$ inside the fiducial volume, where the error is statistical. Because the acceptance depends on the decay modes of the two taus in the event, an additional systematic uncertainty of 0.25% must be added due to the uncertainties on the tau branching fractions.

The distribution of the number of clusters is evaluated from the data based on a sample of tau-pair events selected using the multiplicity of tracks in the central chamber instead of clusters in the calorimeters. This study leads to a correction on the total cross section of $(0.8 \pm 0.4)\%$. The other selection quantities show good agreement between the data and the Monte-Carlo prediction (Figure 7). Their systematic uncertainties are derived from varying the corresponding cuts. A total systematic error of 0.6% is assigned to the event selection.

In this sample a background of $(2.75 \pm 0.12)\%$, determined by Monte Carlo, remains from the other Z decay channels. The contamination of cosmic rays is estimated to be $(0.15 \pm 0.05)\%$. The background from two-photon processes is negligible, (0.9 ± 0.5) pb.

Tau-pair events are triggered by the energy, central track, muon or scintillator multiplicity triggers. The cross section is corrected for the overall trigger inefficiency of $(0.10 \pm 0.05)\%$. The contributions to the systematic error on the cross-section measurement are summarized in Table 5, including the Monte-Carlo extrapolation to the full solid angle. We assign a systematic error of 0.7% on the total cross section of the reaction $e^+e^- \rightarrow \tau^+\tau^-(\gamma)$, excluding the error on the luminosity measurement.

The number of selected events and the total cross sections for the different center-of-mass energy points are listed in Table 11 of Section 5. The cross sections are compared to the result of a fit to the complete data set in Figure 15 of Section 6.

Source of Systematic Uncertainty	Contribution to $\delta\sigma_\tau/\sigma_\tau$ [%]
Selection Cuts	0.60
Monte-Carlo Acceptance and Efficiency	0.21
Tau-Decay Branching Fractions	0.25
Background Subtraction	0.14
Trigger Inefficiency	0.05
Total Systematic Uncertainty	0.70

Table 5: Systematic uncertainties on the total tau-pair cross section, σ_τ , excluding the luminosity error.

Forward-Backward Asymmetry

The determination of the forward-backward asymmetry is carried out in the same way as for the $e^+e^- \rightarrow \mu^+\mu^-(\gamma)$ events, i.e., independent of the acceptance at each value of the scattering angle. The charge of a tau is derived from the sum of the charges of its decay products as measured in the central tracking chamber. As the background of $e^+e^- \rightarrow e^+e^-(\gamma)$ events is mainly concentrated at the edges of the barrel electromagnetic calorimeter, events used in the asymmetry determination are restricted to $|\cos \theta_t| < 0.7$.

For the determination of the forward-backward asymmetry we take only those events where the charges of the two tau jets have unequal sign (85% of the 1992 data sample). The probability for a reversed assignment of the charges in these events is determined from the ratio of like and unlike sign events in the data to be $(1.20 \pm 0.05)\%$. We correct the observed asymmetry for the charge confusion and assign a residual systematic error on the asymmetry of $0.001A_{\text{fb}}^\tau$ due to charge confusion.

The systematic uncertainty due to the subtraction of the $e^+e^- \rightarrow e^+e^-(\gamma)$ background in conjunction with a variation of the fiducial volume cut in $|\cos \theta_t|$ is estimated to be at most 0.003. Since the asymmetry of Z decays into muon pairs is expected and measured to be close to that of Z decays into tau pairs, the remaining background of dimuon events does not change the observed tau asymmetry. The uncertainty introduced by the cosmic-ray background is less than 0.001.

The contributions to the systematic error on the asymmetry measurement are summarized in Table 6. We assign an absolute error of 0.003 on the forward-backward asymmetry of the reaction $e^+e^- \rightarrow \tau^+\tau^-(\gamma)$.

The differential cross section, $d\sigma_\tau/d\cos\theta$, of the reaction $e^+e^- \rightarrow \tau^+\tau^-(\gamma)$ for events collected at 91.29 GeV (1992 data) is shown in Figure 8. The result for the forward-backward asymmetry obtained from a fit to this distribution agrees with the result from the maximum-likelihood method. The forward-backward asymmetries for the different center-of-mass energy points are listed in Table 13 of Section 5. The asymmetries are compared to the result of a fit to the complete data set in Figure 18 of Section 6.

Source of Systematic Uncertainty	Contribution to $\delta A_{\text{fb}}^\tau$
Charge Confusion	$0.001A_{\text{fb}}^\tau$
Fiducial Volume	0.003
Cosmic-Ray Background	0.001
Total Systematic Uncertainty	0.003

Table 6: Systematic uncertainties on the tau-pair forward-backward asymmetry, A_{fb}^τ .

4.4 $e^+e^- \rightarrow e^+e^-(\gamma)$

Event Selection

The selection of $e^+e^- \rightarrow e^+e^-(\gamma)$ events makes use of the fact that such events deposit a large amount of electromagnetic energy concentrated in a small number of BGO clusters. The events must satisfy at least one of the following three requirements:

1. There must be at least two clusters in the electromagnetic calorimeter. The highest energy cluster must have an energy measured in the BGO, E_{\max} , larger than $0.9E_{\text{beam}}$. The second cluster must have an energy larger than 2 GeV.
2. The sum of the energy of the four highest energy clusters in the electromagnetic calorimeter, E_{BGO} , must be larger than 70% of the center-of-mass energy.
3. When there is no second cluster in the electromagnetic calorimeter with an energy larger than 2 GeV, we require a cluster in the hadron calorimeter with electromagnetic shower shape and at least 7.5 GeV energy opposite to the leading cluster. This recovers events (0.4% of the final sample) with energy leaking through the BGO support structure.

The acollinearity angle, ξ , between the directions of the two clusters of highest energy is required to be less than 25° . We also require less than 15 clusters in total to suppress the hadronic Z decays.

The cross section and forward-backward asymmetry are measured at large polar angles, where the relative contribution of the s-channel Z exchange is dominant.

Two event samples are maintained as in the luminosity analysis. The first sample consists of the selected events where the highest energy cluster on the $+z$ side has a polar angle $\theta > 44.69^\circ$. The second sample consists of the selected events where the highest energy cluster on the $-z$ side has a polar angle $\theta < 135.31^\circ$. These angles correspond to a distance of 1.5 crystal widths away from the edges of the barrel electromagnetic calorimeter. The average cross section of the two samples has a reduced sensitivity to beam offsets and differences in the beam spot shapes between data and Monte-Carlo events. A symmetric fiducial volume cut, $44^\circ < \theta < 136^\circ$, for the two highest energy clusters, which excludes the outermost ring of barrel crystals, gives consistent results once the beam spot parameters in the simulation are tuned to the experimental values.

Figure 9 shows the distribution of the energy of the highest energy cluster and the energy sum of the four highest energy clusters, comparing the data to fully simulated Monte-Carlo events.

Cross Section

The efficiency of the selection, $(97.29 \pm 0.10)\%$, is determined using Monte-Carlo events generated with the program BHAGENE3 [20], which generates up to three radiative photons in the final state. As a cross-check we also use events generated to first order with the program BABAMC [11]. The efficiencies estimated with the two event generators agree to within 0.1%.

The exact knowledge of the geometry of the barrel electromagnetic calorimeter is important for the angular cuts. By comparing the survey measurements with the data from the central tracking chamber and the hadron calorimeter we estimate the error in the definition of the fiducial volume to be less than 0.05° , which corresponds to a systematic error of 0.15% in the measured cross section.

The selection quantities show good agreement between the data and the Monte-Carlo prediction (Figure 9). The systematic uncertainties of the selection are estimated from variations of the cuts around their nominal values. The energy cuts contribute with 0.21% and the angular cuts with 0.16% to the total systematic error.

The background, estimated using fully simulated Monte Carlo events, consists of $(1.53 \pm 0.09)\%$ $\tau^+\tau^-(\gamma)$ events and (16.4 ± 0.1) pb of $e^+e^- \rightarrow \gamma\gamma(\gamma)$ events at the Z peak. The background of hadronic events is below 0.1%.

The $e^+e^- \rightarrow e^+e^-(\gamma)$ events are triggered by the energy, central track or scintillator multiplicity triggers. The cross section is corrected for the overall trigger inefficiency of $(0.06 \pm 0.01)\%$. The contributions to the systematic error on the cross-section measurement are summarized in Table 7. We assign a systematic error of 0.3% on the total cross section of the reaction $e^+e^- \rightarrow e^+e^-(\gamma)$, excluding the error on the luminosity measurement.

The number of selected events and the cross sections for the different center-of-mass energy points are listed in Table 12 of Section 5. The measured cross sections are compared to the result of a fit to the complete data set in Figure 16 of Section 6.

Source of Systematic Uncertainty	Contribution to $\delta\sigma_e/\sigma_e$ [%]
Selection Cuts	0.26
Monte-Carlo Acceptance and Efficiency	0.11
Background Subtraction	0.13
Trigger Inefficiency	0.01
Total Systematic Uncertainty	0.31

Table 7: Systematic uncertainties on the $e^+e^- \rightarrow e^+e^-(\gamma)$ cross section, σ_e , excluding the luminosity error.

Forward-Backward Asymmetry

The asymmetry measurement uses the events passing the symmetric fiducial volume cut. The charges of the outgoing particles are determined by the tracks in the central tracking chamber. We require two tracks corresponding to the two leptons. In the plane transverse to the beam direction, one of the two has to match to the highest energy cluster within 25 mrad and the second track to the second cluster within 50 mrad. We define two separators which should have positive values if the first track is a positron and negative values if it is an electron:

1. $\Delta\rho = \rho_1 - \rho_2$, where $\rho = \hat{\rho} \sin \theta$. This separator is the difference of the signed curvatures, $\hat{\rho} \propto q/p_\perp$, corrected for their θ dependence, of the two tracks as measured by the central tracking chamber. For single tracks of 45 GeV momentum, the lever arm of 31 cm in the central chamber leads to a resolution on the curvature of 75% after including the average interaction point as a constraint in the track fit.
2. $\sin \Delta\phi = \sin(\hat{\phi}_1 - \hat{\phi}_2)(\sin \theta_1 + \sin \theta_2)/2$, where $\hat{\phi}$ is the azimuthal angle of a straight line fitted to the hits forming a track. The factor $(\sin \theta_1 + \sin \theta_2)/2$ corrects for the θ dependence of the difference in these azimuthal angles. This separator, exploiting the good angular resolution of the central tracking chamber, is useful for events without hard photon radiation.

As shown in Figure 10a, the events cluster in the $(\Delta\rho, \sin \Delta\phi)$ plane around two centers, C_+ and C_- , with coordinates $C_\pm = \pm(7.1 \cdot 10^{-3} \text{m}^{-1}, 1.9 \cdot 10^{-3})$. The Gaussian widths of the clusters in the coordinates, $\Delta\rho$ and $\sin \Delta\phi$, are $\sigma_{\Delta\rho} = 3.4 \cdot 10^{-3} \text{m}^{-1}$ and $\sigma_{\Delta\phi} = 0.56 \cdot 10^{-3}$, respectively. These widths are used to calculate the distances, d_+ and d_- , of each event in the $(\Delta\rho/\sigma_{\Delta\rho}, \sin \Delta\phi/\sigma_{\Delta\phi})$ plane to the two centers. The quantity $\mathcal{P} = d_-/(d_+ + d_-)$, whose distribution is shown in Figure 10b, determines the charge flow in the event. If $\mathcal{P} > 0.5$,

meaning the event is closer to C_+ than to C_- , the first track is recognized as a positron. If $\mathcal{P} < 0.5$, meaning the event is closer to C_- , the first track is recognized as an electron.

This procedure has been studied with the $\mu^+\mu^-(\gamma)$ sample where the charge is determined independently with much higher precision by the muon spectrometer. We have reversed charge assignment for $(3.1 \pm 0.2)\%$ of the events in the 1992 data sample and for $(4.0 \pm 0.3)\%$ of the events in the 1991 data sample. As this charge confusion is the main source of systematic error in the asymmetry measurement we have studied a subset of the events with much lower charge confusion by selecting events with tracks outside the lower precision regions close to the cathode and anode planes of the central tracking chamber. After correction for the reversed charge assignment the asymmetries of the two samples agree to within 0.0020.

The polar angles of the scattered leptons are determined from the reconstructed center of the cluster in the electromagnetic calorimeter and the average position of the e^+e^- interaction point. The polar angle, θ , is measured with a resolution of 1° , which is dominated by the longitudinal width of the interaction region, $\sigma_z = 8$ mm.

The forward-backward asymmetry, A_{fb}^e , is measured by counting the events in the forward and backward hemispheres. The data are corrected bin-by-bin for the $\cos\theta$ dependent acceptance and charge confusion. The efficiency of the track selection is estimated using the data itself by comparing the events selected for the asymmetry measurement and for the cross-section measurement, where only calorimetric information is used. To reduce the sensitivity to beam spot offsets, the asymmetry is measured twice using the scattered e^- or the e^+ . The average of the two measurements determines the asymmetry, A_{fb}^e , of the event sample.

The contributions to the systematic error on the asymmetry measurement are summarized in Table 8. We assign an absolute error of 0.002 on the forward-backward asymmetry of the reaction $e^+e^- \rightarrow e^+e^-(\gamma)$.

The differential cross section, $d\sigma_e/d\cos\theta$, of the reaction $e^+e^- \rightarrow e^+e^-(\gamma)$ for events collected at 91.29 GeV (1992 data) is shown in Figure 11. The forward-backward asymmetries for the different center-of-mass energy points are listed in Table 13 of Section 5. The measured asymmetries are compared to the result of a fit to the complete data set in Figure 19 of Section 6.

Source of Systematic Uncertainty	Contribution to δA_{fb}^e
Charge Confusion	0.0020
Width of Interaction Region in z	0.0010
Tau-Pair Background	0.0005
Total Systematic Uncertainty	0.0023

Table 8: Systematic uncertainties on the $e^+e^- \rightarrow e^+e^-(\gamma)$ forward-backward asymmetry, A_{fb}^e .

5 Cross-Section and Forward-Backward Asymmetry Results

Tables 9 to 13 summarize our measurements of the cross sections and forward-backward asymmetries from the 1990, 1991 and 1992 data. These are used as input to the analysis described in Section 6. The quoted cross sections are total cross sections extrapolated to the full solid angle of 4π , except for the process $e^+e^- \rightarrow e^+e^-(\gamma)$, where the measured total cross sections, σ_e , and the measured forward-backward asymmetries, A_{fb}^e , are within a restricted fiducial volume of $44^\circ < \theta < 136^\circ$ and with an acollinearity-angle cut of $\xi < 25^\circ$.

For completeness, we also give the s-channel contribution to the process $e^+e^- \rightarrow e^+e^-(\gamma)$ extrapolated to the full solid angle. Using the analytical program ALIBABA [21], which calculates this process in the framework of the SM, we correct the measured total cross sections and forward-backward asymmetries for the t-channel and s/t-interference contributions expected in the SM. The calculations to derive the extrapolated s-channel cross section, σ_e^s , and its statistical error, $\delta\sigma_e^s$, are as follows:

$$\begin{aligned}\sigma_e^s &= \left[\sigma_e - \sigma_e^{t+s/t}(44^\circ < \theta < 136^\circ, \xi < 25^\circ)_{\text{SM}} \right] \cdot \left(\frac{\sigma_e^s}{\sigma_e^s(44^\circ < \theta < 136^\circ, \xi < 25^\circ)} \right)_{\text{SM}} \\ \delta\sigma_e^s &= \delta\sigma_e \cdot \left(\frac{\sigma_e^s}{\sigma_e^s(44^\circ < \theta < 136^\circ, \xi < 25^\circ)} \right)_{\text{SM}}.\end{aligned}$$

In the case of the forward-backward asymmetry, $A_{\text{fb}} = (\sigma_f - \sigma_b)/(\sigma_f + \sigma_b)$, we perform the analogous calculation for σ_f and σ_b . The extrapolated s-channel cross sections, σ_e^s , without any cuts, and s-channel asymmetries, $A_{\text{fb}}^{e,s}$, with an acollinearity angle cut of $\xi < 25^\circ$, are also given (Tables 12 and 13). The additional systematic errors introduced by this procedure are estimated to be 0.2% in the case of cross sections and 0.002 in the case of asymmetries. They are given by the uncertainties in the corrections due to the allowed range of values for the SM parameters used for the ALIBABA calculations, $m_Z = 91.195 \pm 0.009$ GeV, $\alpha_s = 0.123 \pm 0.006$ [4], and taking $m_t = 150 \pm 50$ GeV, $m_H = 300_{-240}^{+700}$ GeV.

All results are corrected for the 51 MeV spread in the center-of-mass energy, which is due to the finite spread of the particle energy in the LEP beams [22]. The correction is largest for cross sections on the peak, where it increases the observed cross section by 0.14%. The split of the 1991 data sample taken at the peak energy is introduced because the accuracy in the calibration of the LEP beam energy changed during the 1991 run [22].

1990 Data			
\sqrt{s} [GeV]	N_{events}	\mathcal{L} [nb^{-1}]	σ_{had} [nb]
88.231	1525	339.4	4.46 ± 0.12
89.236	3600	422.9	8.52 ± 0.15
90.238	6147	330.9	18.68 ± 0.26
91.230	79157	2624.0	30.44 ± 0.13
92.226	8182	374.4	22.01 ± 0.27
93.228	5922	480.3	12.38 ± 0.17
94.223	3752	465.7	8.06 ± 0.14
Totals	108285	5037.6	
Systematic Uncertainty			$\pm 0.3\%$

1991 Data			
\sqrt{s} [GeV]	N_{events}	\mathcal{L} [nb^{-1}]	σ_{had} [nb]
91.254	155192	5124.9	30.45 ± 0.10
88.480	4051	781.9	5.22 ± 0.09
89.470	8531	846.7	10.15 ± 0.12
90.228	14341	793.3	18.21 ± 0.18
91.222	90686	3010.8	30.33 ± 0.13
91.967	16070	657.6	24.64 ± 0.24
92.966	10869	758.2	14.44 ± 0.16
93.716	7953	793.6	10.10 ± 0.13
Totals	307693	12783.0	
Systematic Uncertainty			$\pm 0.15\%$

1992 Data			
\sqrt{s} [GeV]	N_{events}	\mathcal{L} [nb^{-1}]	σ_{had} [nb]
91.294	677596	22424.7	30.451 ± 0.047
Systematic Uncertainty			$\pm 0.15\%$

Table 9: Cross sections for $e^+e^- \rightarrow \text{hadrons}(\gamma)$, extrapolated to the full solid angle. The quoted systematic error excludes the uncertainty of 0.6% in the luminosity.

1990 Data			
\sqrt{s} [GeV]	N_{events}	\mathcal{L} [nb $^{-1}$]	σ_{μ} [nb]
88.231	66	388.6	0.268 ± 0.033
89.236	104	421.0	0.388 ± 0.038
90.238	217	364.9	0.931 ± 0.063
91.230	2675	2822.4	1.478 ± 0.028
92.226	282	394.8	1.116 ± 0.066
93.228	160	496.6	0.506 ± 0.040
94.223	123	480.4	0.405 ± 0.036
Totals	3627	5368.7	
Systematic Uncertainty			$\pm 0.8\%$

1991 Data			
\sqrt{s} [GeV]	N_{events}	\mathcal{L} [nb $^{-1}$]	σ_{μ} [nb]
91.254	5182	5039.5	1.510 ± 0.021
88.480	135	779.4	0.259 ± 0.022
89.470	280	849.9	0.486 ± 0.029
90.228	471	793.2	0.871 ± 0.040
91.222	2778	2925.6	1.393 ± 0.026
91.967	567	699.9	1.190 ± 0.050
92.966	368	758.2	0.718 ± 0.037
93.716	267	829.8	0.478 ± 0.029
Totals	9547	12675.5	
Systematic Uncertainty			$\pm 0.5\%$

1992 Data			
\sqrt{s} [GeV]	N_{events}	\mathcal{L} [nb $^{-1}$]	σ_{μ} [nb]
91.294	20752	20748.5	1.466 ± 0.010
Systematic Uncertainty			$\pm 0.5\%$

Table 10: Cross sections for $e^+e^- \rightarrow \mu^+\mu^-(\gamma)$, extrapolated to the full solid angle. The quoted systematic error excludes the uncertainty of 0.6% in the luminosity.

1990 Data			
\sqrt{s} [GeV]	N_{events}	\mathcal{L} [nb^{-1}]	σ_{τ} [nb]
88.231	36	337.4	0.219 ± 0.036
89.236	86	404.2	0.445 ± 0.048
90.238	138	319.4	0.912 ± 0.078
91.230	1887	2717.7	1.472 ± 0.034
92.226	190	365.9	1.097 ± 0.080
93.228	133	471.7	0.592 ± 0.051
94.223	94	476.7	0.411 ± 0.042
Totals	2564	5093.0	
Systematic Uncertainty			$\pm 0.9\%$

1991 Data			
\sqrt{s} [GeV]	N_{events}	\mathcal{L} [nb^{-1}]	σ_{τ} [nb]
91.254	3720	4902.6	1.507 ± 0.025
88.480	95	779.4	0.236 ± 0.024
89.470	229	850.0	0.532 ± 0.035
90.228	359	793.3	0.886 ± 0.047
91.222	2102	2882.3	1.449 ± 0.032
91.967	425	689.3	1.226 ± 0.059
92.966	248	758.2	0.642 ± 0.041
93.716	225	829.9	0.535 ± 0.036
Totals	7403	12484.0	
Systematic Uncertainty			$\pm 0.7\%$

1992 Data			
\sqrt{s} [GeV]	N_{events}	\mathcal{L} [nb^{-1}]	σ_{τ} [nb]
91.294	15300	20327.4	1.472 ± 0.012
Systematic Uncertainty			$\pm 0.7\%$

Table 11: Cross sections for $e^+e^- \rightarrow \tau^+\tau^-(\gamma)$, extrapolated to the full solid angle. The quoted systematic error excludes the uncertainty of 0.6% in the luminosity.

1990 Data				
\sqrt{s} [GeV]	N_{events}	\mathcal{L} [nb $^{-1}$]	σ_e [nb]	σ_e^s [nb]
88.231	120	380.1	0.334 ± 0.030	0.186 ± 0.052
89.236	237	466.3	0.533 ± 0.034	0.472 ± 0.057
90.238	310	359.3	0.896 ± 0.050	1.037 ± 0.082
91.230	3020	2960.9	1.053 ± 0.019	1.469 ± 0.031
92.226	276	397.4	0.716 ± 0.043	1.137 ± 0.070
93.228	198	505.5	0.406 ± 0.029	0.659 ± 0.048
94.223	104	485.7	0.223 ± 0.022	0.344 ± 0.037
Totals	4265	5555.2		
Systematic Uncertainty			$\pm 0.4\%$	$\pm 0.5\%$

1991 Data				
\sqrt{s} [GeV]	N_{events}	\mathcal{L} [nb $^{-1}$]	σ_e [nb]	σ_e^s [nb]
91.254	5626	5548.4	1.033 ± 0.014	1.444 ± 0.023
88.480	312	781.9	0.405 ± 0.023	0.297 ± 0.040
89.470	487	860.4	0.574 ± 0.026	0.528 ± 0.043
90.228	620	793.3	0.794 ± 0.032	0.869 ± 0.052
91.222	3222	3076.2	1.069 ± 0.019	1.492 ± 0.031
91.967	580	735.7	0.800 ± 0.033	1.242 ± 0.054
92.966	316	758.2	0.423 ± 0.024	0.687 ± 0.040
93.716	248	831.6	0.304 ± 0.019	0.486 ± 0.032
Totals	11351	13089.6		
Systematic Uncertainty			$\pm 0.3\%$	$\pm 0.4\%$

1992 Data				
\sqrt{s} [GeV]	N_{events}	\mathcal{L} [nb $^{-1}$]	σ_e [nb]	σ_e^s [nb]
91.294	22726	22189.4	1.055 ± 0.007	1.491 ± 0.011
Systematic Uncertainty			$\pm 0.3\%$	$\pm 0.4\%$

Table 12: Cross sections for $e^+e^- \rightarrow e^+e^-(\gamma)$. σ_e is the efficiency corrected cross section for both leptons inside the angular range $44^\circ < \theta < 136^\circ$ with an acollinearity angle cut of $\xi < 25^\circ$. σ_e^s is the s -channel contribution to the cross section extrapolated to the full solid angle (no acollinearity cut), see text. The quoted systematic error excludes the uncertainty of 0.6% in the luminosity.

1990 Data				
\sqrt{s} [GeV]	A_{fb}^{μ}	A_{fb}^{τ}	A_{fb}^e	$A_{\text{fb}}^{e,s}$
88.231	-0.391 ± 0.117	-0.36 ± 0.20	0.520 ± 0.095	-0.141 ± 0.344
89.236	-0.044 ± 0.109	0.00 ± 0.15	0.296 ± 0.070	-0.193 ± 0.136
90.238	-0.184 ± 0.074	-0.13 ± 0.11	0.155 ± 0.064	-0.132 ± 0.091
91.230	0.006 ± 0.021	0.077 ± 0.028	0.101 ± 0.021	-0.014 ± 0.025
92.226	0.110 ± 0.066	0.09 ± 0.09	0.040 ± 0.069	0.033 ± 0.071
93.228	0.095 ± 0.091	0.07 ± 0.11	0.083 ± 0.081	0.092 ± 0.082
94.223	0.134 ± 0.099	0.04 ± 0.13	0.144 ± 0.118	0.112 ± 0.129
Systematic Uncertainty	± 0.005	± 0.005	± 0.004	± 0.005

1991 Data				
\sqrt{s} [GeV]	A_{fb}^{μ}	A_{fb}^{τ}	A_{fb}^e	$A_{\text{fb}}^{e,s}$
91.254	0.028 ± 0.014	0.037 ± 0.021	0.110 ± 0.016	-0.002 ± 0.019
88.480	-0.197 ± 0.097	-0.106 ± 0.128	0.384 ± 0.063	-0.232 ± 0.156
89.470	-0.191 ± 0.063	-0.152 ± 0.083	0.333 ± 0.051	-0.081 ± 0.098
90.228	-0.101 ± 0.050	-0.137 ± 0.070	0.253 ± 0.046	-0.037 ± 0.071
91.222	-0.002 ± 0.020	-0.032 ± 0.029	0.125 ± 0.022	0.014 ± 0.026
91.967	0.058 ± 0.043	0.042 ± 0.063	0.167 ± 0.048	0.147 ± 0.051
92.966	0.117 ± 0.056	0.161 ± 0.080	0.070 ± 0.066	0.080 ± 0.067
93.716	0.089 ± 0.065	0.058 ± 0.082	0.150 ± 0.074	0.147 ± 0.077
Systematic Uncertainty	± 0.002	± 0.005	± 0.004	± 0.005

1992 Data				
\sqrt{s} [GeV]	A_{fb}^{μ}	A_{fb}^{τ}	A_{fb}^e	$A_{\text{fb}}^{e,s}$
91.294	0.007 ± 0.007	0.015 ± 0.010	0.104 ± 0.007	0.001 ± 0.008
Systematic Uncertainty	± 0.002	± 0.003	± 0.002	± 0.003

Table 13: Forward-backward asymmetries, A_{fb}^{ℓ} , for $e^+e^- \rightarrow \ell^+\ell^-(\gamma)$, $\ell = \mu, \tau, e$, including a cut on the acollinearity angle, $\xi < 15^\circ$ for muons, $\xi < 14.3^\circ$ for taus, and $\xi < 25^\circ$ for electrons. A_{fb}^e is the asymmetry determined from counting in the angular range of $44^\circ < \theta < 136^\circ$ for both leptons. $A_{\text{fb}}^{e,s}$ is the s -channel contribution to the forward-backward asymmetry extrapolated to the full solid angle ($\xi < 25^\circ$), see text.

6 Determination of Electroweak Parameters

Three different approaches are used to extract the electroweak parameters from the measured total cross sections and forward-backward asymmetries.

The first two approaches determine the electroweak parameters making a minimum of assumptions about any underlying theory, for example the Standard Model (SM). The first approach uses only the total cross-section data to determine the parameters of the Z boson, its mass, m_Z , total decay width, Γ_Z , and partial decay width to fermion pairs ($f\bar{f}$), Γ_f . The second approach also includes the asymmetry data, which allows the determination of the coupling constants of the neutral weak current. The third approach evaluates all the data within the framework of the SM in order to determine the input parameters of the SM, such as the mass of the top quark.

In all three approaches, a Breit-Wigner ansatz is used to describe the Z boson. The mass, m_Z , and the total width, Γ_Z , of the Z boson are defined by the functional form of the Breit-Wigner denominator, which explicitly takes into account the energy dependence of the total width. The total cross section to lowest order, σ° , for the process $e^+e^- \rightarrow f\bar{f}$, $f \neq e$, is given by the sum of three terms, the Z exchange, σ_Z° , the photon exchange, σ_γ° , and the γZ interference, $\sigma_{\text{int}}^\circ$:

$$\sigma^\circ = \sigma_Z^\circ + \sigma_\gamma^\circ + \sigma_{\text{int}}^\circ \quad (1)$$

$$\sigma_Z^\circ = \frac{12\pi \Gamma_e \Gamma_f}{m_Z^2 \Gamma_Z^2} \frac{s \Gamma_Z^2}{(s - m_Z^2)^2 + s^2 \Gamma_Z^2 / m_Z^2} \quad (2)$$

$$\sigma_\gamma^\circ = \frac{4\pi\alpha^2}{3s} q_e^2 q_f^2 N_C^f \quad (3)$$

$$\sigma_{\text{int}}^\circ = \frac{4\pi\alpha^2}{3} J_f \frac{s - m_Z^2}{(s - m_Z^2)^2 + s^2 \Gamma_Z^2 / m_Z^2}, \quad (4)$$

where q_f is the electric charge of the final-state fermion, N_C^f its color factor, and α the electromagnetic coupling constant. The pure photon exchange is determined by QED.

The first two approaches treat the mass and the total and partial widths of the Z boson as free and independent parameters. The interference of the Z exchange with the photon exchange adds another parameter, the γZ -interference term, J_f , besides those corresponding to mass and widths of the Z. Since in the SM $|\sigma_{\text{int}}^\circ(s)| \ll \sigma^\circ(s)$ for center-of-mass energies, \sqrt{s} , close to m_Z , it is difficult to measure J_f accurately at current LEP energies [23]. The γZ -interference term is usually taken from the SM [3–5, 24, 25], thus making assumptions about the form of the electroweak unification. If instead the γZ -interference term is determined from the data, the errors on correlated parameters, such as the mass of the Z boson, are increased [23].

The second approach determines the vector and axial-vector coupling constants of the neutral weak current to charged leptons, g_V^ℓ and g_A^ℓ , by using the forward-backward asymmetries in addition to the total cross sections. For center-of-mass energies close to m_Z , the forward-backward asymmetry to lowest order, $A_{\text{fb}}^{\circ,\ell}$, for the process $e^+e^- \rightarrow \ell^+\ell^-$, $\ell \neq e$, is given by:

$$A_{\text{fb}}^{\circ,\ell}(s) = \frac{3}{4} A_e A_\ell \left[1 + q_e q_\ell \left(\frac{1}{g_V^e g_V^\ell} - \frac{A_e A_\ell}{g_A^e g_A^\ell} \right) \frac{\sqrt{2}\pi\alpha}{G_F m_Z^2} \cdot \frac{s - m_Z^2}{s} \right] + \mathcal{O}\left(\frac{s - m_Z^2}{s}\right)^2 \quad (5)$$

$$A_\ell = \frac{2 g_V^\ell g_A^\ell}{(g_V^\ell)^2 + (g_A^\ell)^2}. \quad (6)$$

In Equations 2 and 4, the leptonic partial width, Γ_ℓ , and the leptonic γZ -interference term, J_ℓ , are now expressed in terms of g_V^ℓ and g_A^ℓ :

$$\Gamma_\ell = \frac{G_F m_Z^3}{6\sqrt{2}\pi} [(g_V^\ell)^2 + (g_A^\ell)^2] \quad (7)$$

$$J_\ell = \frac{G_F m_Z^2}{\sqrt{2}\pi\alpha} q_e q_\ell g_V^e g_V^\ell, \quad (8)$$

where G_F is the Fermi coupling constant. This approach cannot be applied to the hadronic final state, which is summed over all colors and open quark flavors. Therefore, the parameterization of the first approach is used to express the hadronic cross section in terms of Γ_{had} and J_{had} .

The forward-backward asymmetry measures the vector and axial-vector coupling constants, g_V^ℓ and g_A^ℓ , in a different combination than Γ_ℓ . Its energy dependence distinguishes g_V^ℓ and g_A^ℓ , see Equation 5.

The QED radiative corrections on the total cross sections and forward-backward asymmetries are included by convolution and by the replacement $\alpha \rightarrow \alpha(s) = \alpha/(1 - \Delta\alpha)$ to account for the running of the electromagnetic coupling constant [26,27]. Weak corrections cannot be calculated without assumptions about the underlying electroweak theory, such as the mass of the top quark, m_t , and the mass of the Higgs boson, m_H , in the SM. Therefore, we define the effective coupling constants, \bar{g}_V^ℓ and \bar{g}_A^ℓ , which absorb these weak corrections.

Assuming lepton universality, the effective couplings are expressed in terms of the effective electroweak mixing angle, $\sin^2 \bar{\theta}_W$, and the effective ratio of the neutral to charged weak current couplings, $\bar{\rho} = 1/(1 - \Delta\bar{\rho})$ [28]:

$$\bar{g}_V^\ell = \sqrt{\bar{\rho}} \cdot (I_3^\ell - 2q_\ell \sin^2 \bar{\theta}_W) \quad (9)$$

$$\bar{g}_A^\ell = \sqrt{\bar{\rho}} \cdot I_3^\ell, \quad (10)$$

where I_3^ℓ is the third component of the weak isospin of the lepton, ℓ .

The third approach to determine electroweak parameters uses the framework of the SM. By comparing its predictions with the set of experimental measurements, it is possible to test the consistency of the SM.

The input parameters of the SM are α , the fermion masses, m_H , m_Z , and the mass of the W boson, m_W . QCD adds one more parameter, the strong coupling constant, α_s . The electromagnetic coupling constant and the fermion masses, with the exception of the top-quark mass, are known with sufficient precision. The effect on the radiative corrections due to the mass of the Higgs boson is too small to be measurable. While the Z mass is measured with high precision at LEP, the mass of the W boson is not known with similar precision. Therefore, m_W is replaced by the Fermi coupling constant, G_F , measured in muon decay, using the relation [29]:

$$\frac{G_F}{\sqrt{2}} = \frac{\pi\alpha}{2} \cdot \frac{1}{m_Z^2 \sin^2 \theta_W \cos^2 \theta_W} \cdot \frac{1}{1 - \Delta r}, \quad (11)$$

where $\sin^2 \theta_W$ is defined as:

$$\sin^2 \theta_W = 1 - \frac{m_W^2}{m_Z^2}, \quad (12)$$

and Δr takes into account the electroweak radiative corrections, $\Delta r = \Delta\alpha - \cot^2 \theta_W \Delta\bar{\rho} + \Delta r_{\text{remainder}}$ [29]. With this procedure the relevant unknown parameters of the SM are m_Z , α , and m_t .

The results of the three approaches are given in the subsections below.

In all three analysis procedures we use the analytical program ZFITTER 4.60 [19] for the calculation of the higher-order corrections and the predictions of the SM. ZFITTER includes electroweak radiative corrections to $\mathcal{O}(\alpha)$ and a common exponentiation of initial- and final-state bremsstrahlung. The corrections to $\mathcal{O}(\alpha^2)$ are taken into account in the leading-log approximation and include the production of photon and fermion pairs in the initial state. Furthermore, the $\mathcal{O}(\alpha)$ and $\mathcal{O}(\alpha^2)$ corrections are supplemented with the $\mathcal{O}(\alpha\alpha_s m_t^2/m_W^2)$ and the $\mathcal{O}(\alpha^2 m_t^4/m_W^4)$ corrections from top-quark insertions in the gauge-boson self energies and in the $Zb\bar{b}$ vertex. In the case of the b-quark asymmetries, the $\mathcal{O}(\alpha\alpha_s m_t^2/m_W^2)$ corrections of the $Zb\bar{b}$ vertex are not included as they are not yet available. QCD corrections in final states with quarks are considered up to $\mathcal{O}(\alpha_s^3)$.

The electroweak parameters are determined in a χ^2 fit using the MINUIT program [30]. The χ^2 is constructed from the measurements, their errors including the correlations, and the theoretical expectations.

In the case of the process $e^+e^- \rightarrow e^+e^-(\gamma)$, the existence of the t-channel exchange of the γ and Z bosons and its interference with the s-channel exchange lead to additional complications. Analytical programs to calculate this process, such as the program ALIBABA [21], are not directly suited for fitting purposes, as computationally they are very time consuming. Thus, the following procedure is adopted. During the initialization of a fit, ALIBABA is used once to calculate the predictions of the t-channel and s/t-interference contributions to the measured $e^+e^- \rightarrow e^+e^-(\gamma)$ cross sections and forward-backward asymmetries. ZFITTER is used during the fits to calculate the corresponding s-channel contributions as a function of the varying electroweak parameters. Since the t-channel and s/t-interference contributions also depend to some extent on the fitted parameters such as m_Z , the fits are iterated. This procedure converges after two iterations. The systematic error introduced by this treatment is included in the total error.

In addition to the experimental errors, we take into account the uncertainties in the determination of the LEP center-of-mass energy [22]. The dominant systematic error on m_Z arising from the LEP energy calibration is due to the error on the absolute energy scale, which for the 1990 data is 26 MeV, for the 1991 data before 14 August is 18 MeV and 5.3 MeV thereafter, and for the 1992 data is 18 MeV. This leads to a systematic error of 7 MeV on the Z mass. The systematic error on Γ_Z due to the LEP energy calibration is 5 MeV, which is dominated by the uncertainty in the relative energy scale.

Further details about the fitting procedures can be found in [4].

6.1 Properties of the Z Boson

Using the first approach described above, we carry out fits to the total cross-section data of the reactions $e^+e^- \rightarrow \text{hadrons}$, e^+e^- , $\mu^+\mu^-$ and $\tau^+\tau^-$ to determine the mass and the total and partial widths of Z boson. The results are summarized Table 14. For the mass, m_Z , and the total width, Γ_Z , we find:

$$m_Z = 91195 \pm 6 \pm 7(\text{LEP}) \text{ MeV} \quad (13)$$

$$\Gamma_Z = 2494 \pm 9 \pm 5(\text{LEP}) \text{ MeV}. \quad (14)$$

The first error is experimental, and the second error arises from the uncertainties in the LEP energy calibration. In this fit, the γZ -interference term, J_f , is fixed to its SM value, which leads to an error of less than 1 MeV on m_Z due to the SM dependence of J_f on m_t and m_H .

Parameters [MeV]	Treatment of Charged Leptons		Standard Model
	Non-Universality	Universality	
m_Z	$91195 \pm 6 \pm 7$ (LEP)	$91195 \pm 6 \pm 7$ (LEP)	—
Γ_Z	$2494 \pm 9 \pm 5$ (LEP)	$2494 \pm 9 \pm 5$ (LEP)	2491^{+21}_{-18}
Γ_{had}	1749 ± 11	1748 ± 10	1739^{+16}_{-14}
Γ_e	83.43 ± 0.52	—	$83.7^{+0.6}_{-0.5}$
Γ_μ	83.20 ± 0.79	—	
Γ_τ	84.04 ± 0.94	—	
Γ_ℓ	—	83.49 ± 0.46	
χ^2 / DOF	52/58	53/60	—

Table 14: Results on the mass and total and partial widths of the Z boson derived from the cross-section data. SM expectations are listed using the fitted Z mass, $m_Z = 91.195 \pm 0.009$ GeV, $\alpha_s = 0.123 \pm 0.006$ and taking $m_t = 150 \pm 50$ GeV, $m_H = 300^{+700}_{-240}$ GeV.

If we instead leave the leptonic and hadronic γZ -interference terms as free parameters to be determined from the data, we obtain:

$$m_Z = 91190 \pm 6 \pm 7 \pm 9(J_{\text{had}}) \text{ MeV}. \quad (15)$$

The correlation between the mass of the Z, m_Z , and the hadronic γZ -interference term, J_{had} , is shown in Figure 12. In such a fit, the uncertainty on the γZ -interference term substantially increases the total error on m_Z from 9 to 13 MeV. The errors on the total and partial widths of the Z boson increase only marginally. In order to reduce this additional uncertainty on m_Z , a better determination of J_f is necessary, which can be achieved by accurately measuring cross sections further away from the Z resonance peak [31,32].

If we do not assume universality of charged leptons, we obtain the partial decay widths of the Z boson to the three types of charged leptons separately. The three partial widths are in good agreement with each other (Table 14). Assuming lepton universality, we fit for one leptonic partial width, Γ_ℓ , instead of three, where Γ_ℓ is defined as the partial decay width of the Z into a pair of massless charged leptons. The partial decay widths for the inclusive hadronic and charged leptonic final states are given by:

$$\Gamma_{\text{had}} = 1748 \pm 10 \text{ MeV} \quad (16)$$

$$\Gamma_\ell = 83.49 \pm 0.46 \text{ MeV}. \quad (17)$$

Our results on the total and partial widths of the Z boson are in good agreement with the predictions of the SM.

From the total and partial widths and their correlations, we derive the decay width of the Z boson into invisible particles:

$$\Gamma_{\text{inv}} = \Gamma_Z - \Gamma_{\text{had}} - (3 + \delta_\tau) \Gamma_\ell = 496.5 \pm 7.9 \text{ MeV}, \quad (18)$$

where $\delta_\tau = -0.0023$ includes the effect of the tau mass [28]. Within the SM, the invisible width is exclusively given by the decay of the Z into neutrinos. Thus, Γ_{inv} determines the number, N_ν , of light neutrino species. In order to obtain a result independent of the unknown parameters

of the SM, such as the top-quark and Higgs-boson masses, the following relation is used to evaluate N_ν :

$$N_\nu = \frac{\Gamma_{\text{inv}}}{\Gamma_\ell} \left(\frac{\Gamma_\ell}{\Gamma_\nu} \right)_{\text{SM}}. \quad (19)$$

Most higher-order corrections involving m_t and m_H cancel in the ratio:

$$\left(\frac{\Gamma_\ell}{\Gamma_\nu} \right)_{\text{SM}} = 0.5015 \pm 0.0007, \quad (20)$$

where the error is due to residual m_t and m_H dependence estimated by varying m_t between 100 and 200 GeV, and m_H between 60 and 1000 GeV. The value of N_ν is determined to be:

$$N_\nu = 2.981 \pm 0.050, \quad (21)$$

where the error is dominated by the error in the luminosity measurement. The above results are in agreement with the determination of Γ_{inv} derived from the measurement of the $e^+e^- \rightarrow \nu\bar{\nu}\gamma$ cross section [33].

6.2 Coupling Constants of the Neutral Weak Current

Fits to the hadronic cross-section and leptonic cross-section and forward-backward asymmetry data are performed using the second approach described above, with and without the assumption of lepton universality. Table 15 summarizes the results in terms of the hadronic cross section, $\sigma_{\text{had}}^\circ$, the leptonic asymmetries, $A_{\text{fb}}^{\circ,\ell}$, at $s = m_Z^2$ and unfolded for QED corrections, and the ratio of the hadronic to the leptonic partial widths, R_{had}^ℓ :

$$\sigma_{\text{had}}^\circ = \frac{12\pi}{m_Z^2} \cdot \frac{\Gamma_e \Gamma_{\text{had}}}{\Gamma_Z^2} \quad (22)$$

$$R_{\text{had}}^\ell = \frac{\Gamma_{\text{had}}}{\Gamma_\ell} \quad (23)$$

$$A_{\text{fb}}^{\circ,\ell} = \frac{3}{4} A_e A_\ell. \quad (24)$$

The advantage of these quantities is that they are less correlated than Γ_{had} , \bar{g}_V^ℓ and \bar{g}_A^ℓ [25]. The corresponding correlation matrices are given in Tables 16 and 17.

Figures 13, 14, 15 and 16 show the measured cross sections compared to the result of the fit assuming lepton universality, as well as the ratio between the measured and fitted cross sections. Figures 17, 18 and 19 show the measured forward-backward asymmetries compared to the result of this fit.

The measurement of the average tau polarization, \mathcal{P}_τ , adds important additional information about \bar{g}_V^ℓ and \bar{g}_A^ℓ , because [34]:

$$\mathcal{P}_\tau(s = m_Z^2) = -A_\tau = -\frac{2 \bar{g}_V^\tau \bar{g}_A^\tau}{(\bar{g}_V^\tau)^2 + (\bar{g}_A^\tau)^2} \quad (25)$$

which also determines the relative sign of \bar{g}_V^ℓ and \bar{g}_A^ℓ . We determine the leptonic effective coupling constants using the total cross sections and leptonic forward-backward asymmetries, including our measurement of $\mathcal{P}_\tau = -0.132 \pm 0.033$ [35]. The results are shown in Table 18. The measurements for the three charged lepton species are in good agreement and confirm the

Parameter	Treatment of Charged Leptons		Standard Model
	Non-Universality	Universality	
m_Z [MeV]	$91195 \pm 6 \pm 7$ (LEP)	$91195 \pm 6 \pm 7$ (LEP)	—
Γ_Z [MeV]	$2495 \pm 9 \pm 5$ (LEP)	$2495 \pm 9 \pm 5$ (LEP)	2491^{+21}_{-18}
$\sigma_{\text{had}}^\circ$ [nb]	41.39 ± 0.26	41.42 ± 0.26	$41.43^{+0.08}_{-0.06}$
R_{had}^e	20.96 ± 0.15	—	20.77 ± 0.07
R_{had}^μ	21.02 ± 0.16	—	
R_{had}^τ	20.80 ± 0.20	—	
R_{had}^ℓ	—	20.93 ± 0.10	
$A_{\text{fb}}^{\circ,e}$	0.0104 ± 0.0092	—	$0.014^{+0.005}_{-0.003}$
$A_{\text{fb}}^{\circ,\mu}$	0.0179 ± 0.0061	—	
$A_{\text{fb}}^{\circ,\tau}$	0.0265 ± 0.0088	—	
$A_{\text{fb}}^{\circ,\ell}$	—	0.0184 ± 0.0045	
χ^2 / DOF	84/103	87/107	—

Table 15: Results on the peak hadronic cross section, $\sigma_{\text{had}}^\circ$, and peak leptonic asymmetries, $A_{\text{fb}}^{\circ,\ell}$, unfolded for QED corrections, and ratios of hadronic to leptonic widths, R_{had}^ℓ , derived from the forward-backward asymmetry and cross-section data. SM expectations are listed using the fitted Z mass, $m_Z = 91.195 \pm 0.009$ GeV, $\alpha_s = 0.123 \pm 0.006$ and taking $m_t = 150 \pm 50$ GeV, $m_H = 300^{+700}_{-240}$ GeV.

Parameter	m_Z	Γ_Z	$\sigma_{\text{had}}^\circ$	R_{had}^e	R_{had}^μ	R_{had}^τ	$A_{\text{fb}}^{\circ,e}$	$A_{\text{fb}}^{\circ,\mu}$	$A_{\text{fb}}^{\circ,\tau}$
m_Z	1.000	0.079	-0.004	0.008	0.001	0.000	0.033	0.055	0.038
Γ_Z	0.079	1.000	-0.106	-0.011	-0.006	-0.002	0.004	0.000	0.001
$\sigma_{\text{had}}^\circ$	-0.004	-0.106	1.000	-0.045	0.069	0.055	0.088	-0.009	-0.006
R_{had}^e	0.008	-0.011	-0.045	1.000	0.067	0.052	-0.102	0.002	0.001
R_{had}^μ	0.001	-0.006	0.069	0.067	1.000	0.050	-0.001	0.012	0.000
R_{had}^τ	0.000	-0.002	0.055	0.052	0.050	1.000	-0.001	0.000	0.010
$A_{\text{fb}}^{\circ,e}$	0.033	0.004	0.088	-0.102	-0.001	-0.001	1.000	0.016	0.011
$A_{\text{fb}}^{\circ,\mu}$	0.055	0.000	-0.009	0.002	0.012	0.000	0.016	1.000	0.018
$A_{\text{fb}}^{\circ,\tau}$	0.038	0.001	-0.006	0.001	0.000	0.010	0.011	0.018	1.000

Table 16: Correlation matrix of the parameters m_Z , Γ_Z , $\sigma_{\text{had}}^\circ$, R_{had}^ℓ and $A_{\text{fb}}^{\circ,\ell}$, for $\ell = e, \mu, \tau$, not assuming lepton universality.

Parameter	m_Z	Γ_Z	$\sigma_{\text{had}}^\circ$	R_{had}^ℓ	$A_{\text{fb}}^{\circ,\ell}$
m_Z	1.000	0.079	-0.003	0.006	0.074
Γ_Z	0.079	1.000	-0.108	-0.010	0.002
$\sigma_{\text{had}}^\circ$	-0.003	-0.108	1.000	0.043	0.028
R_{had}^ℓ	0.006	-0.010	0.043	1.000	-0.020
$A_{\text{fb}}^{\circ,\ell}$	0.074	0.002	0.028	-0.020	1.000

Table 17: Correlation matrix of the parameters m_Z , Γ_Z , $\sigma_{\text{had}}^\circ$, R_{had}^ℓ and $A_{\text{fb}}^{\circ,\ell}$, assuming lepton universality.

Parameter	Treatment of Charged Leptons		Standard Model
	Non-Universality	Universality	
m_Z [MeV]	$91195 \pm 6 \pm 7$ (LEP)	$91195 \pm 6 \pm 7$ (LEP)	—
Γ_Z [MeV]	$2494 \pm 9 \pm 5$ (LEP)	$2495 \pm 9 \pm 5$ (LEP)	2491_{-18}^{+21}
Γ_{had} [MeV]	1749 ± 11	1748 ± 10	1739_{-14}^{+16}
\bar{g}_V^e	$-0.0364_{-0.0082}^{+0.0096}$	—	—
\bar{g}_V^μ	$-0.0402_{-0.0211}^{+0.0153}$	—	—
\bar{g}_V^τ	-0.0384 ± 0.0078	—	—
\bar{g}_V^ℓ	—	$-0.0378_{-0.0042}^{+0.0045}$	$-0.0342_{-0.0057}^{+0.0042}$
\bar{g}_A^e	-0.4998 ± 0.0016	—	—
\bar{g}_A^μ	$-0.4987_{-0.0026}^{+0.0030}$	—	—
\bar{g}_A^τ	-0.5014 ± 0.0029	—	—
\bar{g}_A^ℓ	—	-0.4998 ± 0.0014	$-0.5007_{-0.0014}^{+0.0012}$
χ^2 / DOF	86/104	87/108	—

Table 18: Results on the effective coupling constants, \bar{g}_V^ℓ and \bar{g}_A^ℓ , derived from the tau-polarization, forward-backward asymmetry and cross-section data. SM expectations are listed using the fitted Z mass, $m_Z = 91.195 \pm 0.009$ GeV, $\alpha_s = 0.123 \pm 0.006$ and taking $m_t = 150 \pm 50$ GeV, $m_H = 300_{-240}^{+700}$ GeV.

hypothesis of lepton universality. Assuming this hypothesis, we determine the effective coupling constants for charged leptons to be:

$$\bar{g}_V^\ell = -0.0378_{-0.0042}^{+0.0045} \quad (26)$$

$$\bar{g}_A^\ell = -0.4998 \pm 0.0014. \quad (27)$$

The allowed region of values in the $(\bar{g}_V^\ell, \bar{g}_A^\ell)$ plane is shown in Figure 20. Good agreement with the predictions of the SM is observed.

From the above values of the effective coupling constants and their correlation, we derive the effective electroweak mixing angle, $\sin^2 \bar{\theta}_W$, and $\bar{\rho}$:

$$\sin^2 \bar{\theta}_W = 0.2312 \pm 0.0022 \quad (28)$$

$$\bar{\rho} = 0.9992 \pm 0.0056. \quad (29)$$

As in the case of leptons, the $b\bar{b}$ forward-backward asymmetry also gives information about $\sin^2 \bar{\theta}_W$ [36]. Including our measurement of $A_{fb}^b = 0.086 \pm 0.017$ [37], we obtain:

$$\sin^2 \bar{\theta}_W = 0.2319 \pm 0.0018. \quad (30)$$

6.3 Results in the Framework of the Standard Model

The measurements of the hadronic cross sections, leptonic cross sections and forward-backward asymmetries, average tau polarization, $b\bar{b}$ forward-backward asymmetry are used to estimate the mass of the top quark in the framework of the SM. We also include our measurement of the $Z \rightarrow b\bar{b}$ partial width, $\Gamma_b/\Gamma_{\text{had}} = 0.222 \pm 0.008$ [38]. Using the third approach described above, the free parameters in the fit based on the SM are m_Z , m_t and the strong coupling constant, α_s . The results are:

$$m_Z = 91.195 \pm 0.009 \text{ GeV} \quad (31)$$

$$\alpha_s = 0.142 \pm 0.013 \pm 0.002(\text{Higgs}) \quad (32)$$

$$m_t = 142_{-49}^{+37+18}(\text{Higgs}) \text{ GeV}. \quad (33)$$

The second error expresses the shift in the central values of α_s and m_t for a variation in the mass of the Higgs boson, m_H , from 60 to 1000 GeV around the central value of 300 GeV. The correlation between α_s and m_t is shown in Figure 21. The measurement of R_{had}^ℓ alone also constrains the strong coupling constant [39]. Our measurement of R_{had}^ℓ yields $\alpha_s = 0.141 \pm 0.012$. Both α_s values are in agreement with our measurement of the strong coupling constant from hadronic event topologies and tau decays, $\alpha_s = 0.123 \pm 0.006$ [4]. Constraining α_s to this independent result, the determination of m_t improves:

$$m_t = 158_{-40}^{+32} \pm 19(\text{Higgs}) \text{ GeV}, \quad (34)$$

while the result on m_Z is unchanged. The result on m_t is consistent with current limits on the top-quark mass derived from direct searches [40].

From the fitted values of m_Z and m_t , and for $\alpha_s = 0.123 \pm 0.006$ the following quantities are derived:

$$\sin^2 \bar{\theta}_W = 0.2326 \pm 0.0012 \quad (35)$$

$$\sin^2 \theta_W = 0.2260 \pm 0.0042 \quad (36)$$

$$\Delta r = 0.045 \pm 0.013 \quad (37)$$

$$m_W = 80.22 \pm 0.22 \text{ GeV}, \quad (38)$$

where $\sin^2 \theta_W$ is defined as $(1 - m_W^2/m_Z^2)$. The error on these results due to the uncertainty in the mass of the Higgs boson is negligible. The value of the mass of the W boson as obtained above is in good agreement with the direct measurements of m_W [41].

In order to disentangle new physics beyond the SM from the possibly large, unknown top-quark corrections of leading order $G_F m_t^2$, four new parameters, ϵ_1 , ϵ_2 , ϵ_3 and ϵ_b , have been introduced [42]. Their merit lies in separating out the m_t dependent effects in ϵ_1 and ϵ_b , and other (m_H) effects in ϵ_2 and ϵ_3 . The LEP data at the Z resonance constrain ϵ_1 , ϵ_3 and ϵ_b , the latter by the measurements of b quarks. Our measurements of the hadronic cross sections and leptonic cross sections and asymmetries constrain the parameters ϵ_1 and ϵ_3 , which are defined as:

$$\epsilon_1 = \Delta\bar{\rho} \quad (39)$$

$$\epsilon_3 = (1 - s_0^2)\Delta\bar{\rho} + (1 - 2s_0^2)(\sin^2 \bar{\theta}_W/s_0^2 - 1) \quad (40)$$

$$s_0^2(1 - s_0^2) = [\pi\alpha(m_Z^2)]/[\sqrt{2}G_F m_Z^2]. \quad (41)$$

We find the following values for ϵ_1 and ϵ_3 :

$$\epsilon_1 = -0.0008 \pm 0.0056 \quad (42)$$

$$\epsilon_3 = -0.0012 \pm 0.0073. \quad (43)$$

The range of allowed values in the (ϵ_1, ϵ_3) plane is shown in Figure 22. Our values of the parameters ϵ_1 and ϵ_3 are consistent with the predictions of the SM.

7 Summary and Conclusion

We determine the electroweak parameters from the measurements of the reactions $e^+e^- \rightarrow \text{hadrons}(\gamma)$, $e^+e^- \rightarrow \mu^+\mu^-(\gamma)$, $e^+e^- \rightarrow \tau^+\tau^-(\gamma)$ and $e^+e^- \rightarrow e^+e^-(\gamma)$. This includes the data collected by the L3 detector in the year 1992, when LEP was running exclusively at the center-of-mass energy of $\sqrt{s} = 91.29$ GeV. Together with the data collected in 1990 and 1991 in the energy range $88 < \sqrt{s} < 95$ GeV, the total data sample used for this analysis corresponds to $1.09 \cdot 10^6$ hadronic and $0.98 \cdot 10^5$ leptonic Z decays selected.

All our measurements support the hypothesis of lepton universality. From the hadronic and leptonic cross-section data, we determine the properties of the Z boson:

$$m_Z = 91195 \pm 9 \text{ MeV} \quad (44)$$

$$\Gamma_Z = 2494 \pm 10 \text{ MeV} \quad (45)$$

$$\Gamma_{\text{had}} = 1748 \pm 10 \text{ MeV} \quad (46)$$

$$\Gamma_\ell = 83.49 \pm 0.46 \text{ MeV}. \quad (47)$$

The corresponding invisible width of 496.5 ± 7.9 MeV constrains, within the SM, the number of light neutrino species to be:

$$N_\nu = 2.981 \pm 0.050. \quad (48)$$

Including the leptonic forward-backward asymmetries and the average tau polarization, the effective neutral weak current coupling constants for charged leptons are given by:

$$\bar{g}_V^\ell = -0.0378_{-0.0042}^{+0.0045} \quad (49)$$

$$\bar{g}_A^\ell = -0.4998 \pm 0.0014. \quad (50)$$

Within the SM, and including our measurement of the $Z \rightarrow b\bar{b}$ forward-backward asymmetry and partial decay width, we determine:

$$\alpha_s = 0.142 \pm 0.013 \pm 0.002(\text{Higgs}) \quad (51)$$

$$m_t = 142_{-49}^{+37+18}(\text{Higgs}) \text{ GeV}. \quad (52)$$

This value of α_s is in agreement with our measurement of α_s from hadronic event topologies and tau decays, $\alpha_s = 0.123 \pm 0.006$. Constraining α_s to this independent measurement, we derive:

$$m_t = 158_{-40}^{+32} \pm 19(\text{Higgs}) \text{ GeV}. \quad (53)$$

Alternatively, we determine a value for the mass of the W boson:

$$m_W = 80.22 \pm 0.22 \text{ GeV}, \quad (54)$$

or, expressed in terms of the weak mixing angle:

$$\sin^2 \theta_W = 1 - \frac{m_W^2}{m_Z^2} = 0.2260 \pm 0.0042, \quad (55)$$

which corresponds to the following value of the effective electroweak mixing angle:

$$\sin^2 \bar{\theta}_W = 0.2326 \pm 0.0012. \quad (56)$$

All our measurements are in good agreement with the predictions of the SM.

8 Acknowledgments

We wish to express our gratitude to the CERN accelerator divisions for the excellent performance of the LEP machine. We acknowledge the contributions of all the engineers and technicians who have participated in the construction and maintenance of this experiment.

The L3 Collaboration:

M. Acciarri,²⁵ A. Adam,⁴³ O. Adriani,¹⁵ M. Aguilar-Benitez,²⁴ S. Ahlen,⁹ J. Alcaraz,¹⁶ A. Aloisio,²⁷ G. Alverson,¹⁰ M.G. Alvisi,²⁷ G. Ambrosi,³² Q. An,¹⁷ H. Anderhub,⁴⁶ A.L. Anderson,¹⁴ V.P. Andreev,³⁶ T. Angelescu,¹¹ L. Antonov,⁴⁰ D. Antreasyan,⁷ G. Alkhalaf,²⁴ P. Arce,²⁴ A. Arefiev,²⁶ T. Azemoon,³ T. Aziz,⁸ P.V.K.S. Baba,¹⁷ P. Bagnaia,³⁵ J.A. Bakken,³⁴ L. Baksay,⁴² R.C. Ball,³ S. Banerjee,⁸ K. Banicz,⁴³ J. Bao,⁵ R. Barillere,¹⁶ L. Barone,³⁵ A. Baschirotto,²⁵ R. Battiston,³² A. Bay,¹⁸ F. Becattini,¹⁵ U. Becker,¹⁴ F. Behner,⁴⁶ Gy.L. Bencze,¹² J. Berdugo,²⁴ P. Berges,¹⁴ B. Bertucci,³² B.L. Betev,^{40,46} M. Biasini,³² A. Biland,⁴⁶ G.M. Bilei,³² R. Bizzarri,³⁵ J.J. Blaising,⁴ G.J. Bobbink,^{6,2} R. Bock,¹ A. Böhm,¹ B. Borgia,³⁵ D. Bourilkov,⁴⁶ M. Bourquin,⁸ D. Boutigny,¹⁶ B. Bouwens,² E. Brambilla,²⁷ J.G. Branson,³⁷ V. Brigljevic,⁴⁶ I.C. Brock,³³ M. Brooks,²² A. Bujak,⁴³ J.D. Burger,¹⁴ W.J. Burger,¹⁸ C. Burgos,²⁴ J. Busenitz,⁴² A. Buytenhuijs,²⁹ A. Bykov,³⁶ X.D. Cai,¹⁷ M. Capell,¹⁴ M. Caria,³² G. Carlini,²⁷ A.M. Cartacci,¹⁵ J. Casaus,²⁴ R. Castello,²⁵ N. Cavallo,²⁷ M. Cerrada,²⁴ F. Cesaroni,³⁵ M. Chamizo,²⁴ Y.H. Chang,⁴⁸ U.K. Chaturvedi,¹⁷ M. Chemarin,²³ A. Chen,⁴⁸ C. Chen,⁶ G. Chen,^{6,46} G.M. Chen,⁶ H.F. Chen,¹⁹ H.S. Chen,⁶ M. Chen,¹⁴ G. Chiefari,²⁷ C.Y. Chien,⁵ M.T. Choi,⁴¹ S. Chung,¹⁴ C. Civinini,¹⁵ I. Clare,¹⁴ R. Clare,¹⁴ T.E. Coan,²² H.O. Cohn,³⁰ G. Coignet,⁴ N. Colino,¹⁶ A. Contin,⁷ S. Costantini,³⁵ F. Cotorobai,¹¹ B. de la Cruz,²⁴ X.T. Cui,¹⁷ X.Y. Cui,¹⁷ T.S. Dai,¹⁴ R.D. Alessandro,¹⁵ R. de Asmundis,²⁷ A. Degré,⁴ K. Deiters,⁴⁴ E. Dénes,¹² P. Denes,³⁴ F. DeNotaristefani,³⁵ D. DiBitonto,⁴² M. Diemoz,³⁵ H.R. Dimitrov,⁴⁰ C. Dionisi,³⁵ M. Dittmar,⁴⁶ L. Djambazov,⁴⁶ M.T. Dova,^{17,11} E. Drago,²⁷ D. Duchesneau,⁸ P. Duinker,² I. Duran,³⁸ S. Easo,³² H. El Mamouni,²³ A. Engler,³³ F.J. Eppling,¹⁴ F.C. Ernè,² P. Extermann,¹⁸ R. Fabbretti,⁴⁴ M. Fabre,⁴⁴ S. Falciano,³⁵ S.J. Fan,³⁹ A. Favara,¹⁵ J. Fay,²³ M. Felcini,⁴⁶ T. Ferguson,³² D. Fernandez,²⁴ G. Fernandez,²⁴ F. Ferroni,³⁵ H. Fesefeldt,¹ E. Fiandrini,³² J.H. Field,⁸ F. Filthaut,²⁹ P.H. Fisher,⁵ G. Forconi,¹⁴ L. Fredj,⁸ K. Freudenreich,⁴⁶ W. Friebel,⁴⁵ M. Fukushima,¹⁴ M. Gailloud,²¹ Yu. Galaktionov,^{26,14} E. Gallo,¹⁵ S.N. Ganguli,⁸ P. Garcia-Abia,²⁴ S. Gentile,³⁵ N. Gheordanescu,¹¹ S. Giagu,³⁵ S. Goldfarb,²¹ Z.F. Gong,¹⁹ E. Gonzalez,²⁴ A. Gougas,⁵ D. Goujon,¹⁸ G. Gratta,³¹ M.W. Gruenewald,⁶ C. Gu,¹⁷ M. Guanzioli,¹⁷ J.K. Guo,³⁹ V.K. Gupta,³⁴ A. Gurtu,⁸ H.R. Gustafson,³ L.J. Gutay,⁴³ K. Hangarter,¹ A. Hasan,¹⁷ D. Hauschildt,² C.F. He,³⁹ J.T. He,⁶ T. Hebbeker,¹⁶ M. Hebert,³⁷ A. Hervé,¹⁶ K. Hilgers,¹ H. Hofer,⁴⁶ H. Hoorani,¹⁸ S.R. Hou,⁴⁸ G. Hu,¹⁷ G.Q. Hu,³⁹ B. Ille,²³ M.M. Ilyas,¹⁷ V. Innocente,¹⁶ H. Janssen,⁴ B.N. Jin,⁶ L.W. Jones,³ I. Josa-Mutuberria,¹⁶ A. Kasser,²¹ R.A. Khan,¹⁷ Yu. Kamyshkov,³⁰ P. Kapinos,⁴⁵ J.S. Kapustinsky,²² Y. Karyotakis,¹⁶ M. Kaur,¹⁷ S. Khokhar,¹⁷ M.N. Kienzle-Focacci,¹⁸ J.K. Kim,⁴¹ S.C. Kim,⁴¹ Y.G. Kim,⁴¹ W.W. Kinnison,²² A. Kirkby,³¹ D. Kirkby,³¹ S. Kirsch,⁴⁵ W. Kittel,²⁹ A. Klimentov,^{14,26} A.C. König,²⁹ E. Koffeman,² O. Kornadt,¹ V. Koutsenko,^{14,26} A. Koulbardi,³⁶ R.W. Kraemer,³³ T. Kramer,¹⁴ V.R. Krastev,^{40,32} W. Krenz,¹ H. Kuijten,²⁹ K.S. Kumar,¹³ A. Kunin,^{14,26} P. Ladron de Guevara,²⁴ G. Landi,¹⁵ D. Lanske,¹ S. Lanzano,²⁷ A. Lebedev,¹⁴ P. Lebrun,²³ P. Lecomte,⁴⁶ P. Lecoq,⁶ P. Le Coultre,⁴⁶ D.M. Lee,²² J.S. Lee,⁴¹ K.Y. Lee,⁴¹ I. Leedom,¹⁰ C. Leggett,³ J.M. Le Goff,⁶ R. Leiste,⁴⁵ M. Lenti,¹⁵ E. Leonard,³⁵ P. Levchenko,³⁶ C. Li,^{19,17} H.T. Li,⁶ P.J. Li,³⁹ J.Y. Liao,³⁹ W.T. Lin,⁴⁸ Z.Y. Lin,¹⁹ F.L. Linde,⁶ B. Lindemann,¹ L. Lista,²⁷ Y. Liu,¹⁷ W. Lohmann,⁴⁵ E. Longo,³⁵ W. Lu,³¹ Y.S. Lu,⁶ J.M. Lubbers,¹⁶ K. Lübelmeyer,¹ C. Luci,³⁵ D. Lucney,^{7,14} L. Ludovici,³⁵ L. Luminari,³⁵ W. Luster,⁴⁴ J.M. Ma,⁶ W.G. Ma,¹⁹ M. MacDermott,⁴⁶ L. Malgeri,³⁵ R. Malik,¹⁷ A. Malinin,²⁶ C. Mañá,²⁴ M. Maolinbay,⁴⁶ P. Marchesini,⁴⁶ F. Marion,⁴ A. Marin,⁹ J.P. Martin,²³ F. Marzano,³⁵ G.G.G. Massaro,² K. Mazumdar,⁸ P. McBride,¹³ T. McMahon,⁴³ D. McNally,³⁷ M. Merk,³³ L. Merola,²⁷ M. Meschini,¹⁵ W.J. Metzger,²⁹ Y. Mi,²¹ A. Mihul,¹¹ G.B. Mills,²² Y. Mir,¹⁷ G. Mirabelli,³⁵ J. Mnich,¹ M. Möller,¹ B. Monteleoni,¹⁵ R. Morand,⁴ S. Morganti,³⁵ N.E. Moulai,¹⁷ R. Mount,³¹ S. Müller,¹ E. Nagy,¹² M. Napolitano,²⁷ F. Nessi-Tedaldi,⁴⁶ H. Newman,³¹ M.A. Niaz,¹⁷ A. Nippe,¹ H. Nowak,⁴⁵ G. Organtini,³⁵ D. Pandoulas,¹ S. Paoletti,³⁵ P. Paolucci,²⁷ G. Pascale,³⁵ G. Passaleva,^{15,32} S. Patricelli,²⁷ T. Paul,⁵ M. Pauluzzi,³² C. Paus,¹ F. Paus,⁴⁶ Y.J. Pei,¹ S. Pensotti,²⁵ D. Perret-Gallix,⁴ J. Perrier,¹⁸ A. Pevsner,⁵ D. Piccolo,²⁷ M. Pieri,¹⁶ J.C. Pinto,³³ P.A. Piroué,³⁴ F. Plasil,³⁰ V. Plyaskin,²⁶ M. Pohl,⁴⁶ V. Pojidaev,^{26,15} H. Postema,¹⁴ Z.D. Qi,³⁹ J.M. Qian,³ K.N. Qureshi,¹⁷ R. Raghavan,⁸ G. Rahal-Callot,⁴⁶ P.G. Rancoita,²⁵ M. Rattaggi,²⁵ G. Raven,² P. Razis,²⁸ K. Read,³⁰ M. Redaelli,²⁵ D. Ren,⁴⁶ Z. Ren,¹⁷ M. Rescigno,³⁵ S. Reucroft,¹⁰ A. Ricker,¹ S. Riemann,⁴⁵ B.C. Riemers,⁴³ K. Riles,³ O. Rind,³ H.A. Rizvi,¹⁷ S. Ro,⁴¹ A. Robohm,⁴⁶ F.J. Rodriguez,²⁴ B.P. Roe,³ M. Röhner,¹ S. Röhner,¹ L. Romero,²⁴ S. Rosier-Lees,⁴ R. Rosmalen,²⁹ Ph. Rossetti,²¹ W. van Rossum,² S. Roth,¹ A. Rubbia,¹⁴ J.A. Rubio,¹⁶ H. Rykaczewski,⁴⁶ M. Sachwitz,⁴⁵ J. Salicio,¹⁶ J.M. Salicio,²⁴ E. Sanchez,²⁴ G.S. Sanders,²² A. Santocchia,³² M.S. Sarakinos,¹⁴ G. Sartorelli,^{7,17} M. Sassowsky,¹ G. Sauvage,⁴ C. Schäfer,¹ V. Schegelsky,³⁶ D. Schmitz,¹ P. Schmitz,¹ M. Schneegans,⁴ N. Scholz,⁴⁶ H. Schopper,⁴⁷ D.J. Schotanus,²⁹ S. Shotkin,¹⁴ H.J. Schreiber,⁴⁵ J. Shukla,³³ R. Schulte,¹ K. Schultze,¹ J. Schwenke,¹ G. Schwering,¹ C. Sciacca,²⁷ I. Scott,¹³ R. Sehgal,¹⁷ P.G. Seiler,⁴⁴ J.C. Sens,^{16,2} L. Servoli,³² I. Sheer,³⁷ D.Z. Shen,³⁹ S. Shevchenko,³¹ X.R. Shi,³¹ E. Shumilov,²⁶ V. Shoutko,²⁶ D. Son,⁴¹ A. Sopcak,¹⁶ V. Soulimov,²⁷ C. Spartiotis,²⁰ T. Spickermann,¹ P. Spillantini,¹⁵ R. Starosta,¹ M. Steuer,^{7,14} D.P. Stickland,³⁴ F. Sticozzi,¹⁴ H. Stone,³⁴ K. Strauch,¹³ K. Sudhakar,⁸ G. Sultanov,¹⁷ L.Z. Sun,^{19,17} G.F. Susinno,¹⁸ H. Suter,⁴⁶ J.D. Swain,¹⁷ A.A. Syed,²⁹ X.W. Tang,⁶ L. Taylor,¹⁰ Samuel C.C. Ting,¹⁴ S.M. Ting,¹⁴ O. Toker,³² M. Tonutti,¹ S.C. Tonwar,⁸ J. Tóth,¹² A. Tsaregorodtsev,³⁶ G. Tsipolitis,³³ C. Tully,³⁴ K.L. Tung,⁶ T. Tuuva,²⁰ J. Ulbricht,⁴⁶ L. Urbán,¹² U. Uwer,¹ E. Valente,³⁵ R.T. Van de Walle,²⁹ I. Vetlitsky,²⁶ G. Viertel,⁴⁶ P. Vikas,¹⁷ U. Vikas,¹⁷ M. Vivargent,⁴ H. Vogel,³³ H. Vogt,⁴⁵ I. Vorobiev,^{13,26} A.A. Vorobyov,³⁶ An.A. Vorobyov,³⁶ L. Vuilleumier,²¹ M. Wadhwa,⁴ W. Wallraff,¹ J.C. Wang,¹⁴ C.R. Wang,¹⁹ X.L. Wang,¹⁹ Y.F. Wang,¹⁴ Z.M. Wang,^{17,19} A. Weber,¹ J. Weber,⁴⁶ R. Weill,²¹ J. Wenninger,¹⁸ M. White,¹⁴ C. Willmott,²⁴ F. Wittgenstein,¹⁶ D. Wright,³⁴ S.X. Wu,¹⁷ S. Wynhoff,¹ B. Wyslouch,¹⁴ Y.Y. Xie,³⁹ J.G. Xu,⁶ Z.Z. Xu,¹⁹ Z.L. Xue,³⁹ D.S. Yan,³⁹ B.Z. Yang,¹⁹ C.G. Yang,⁶ G. Yang,¹⁷ C.H. Ye,¹⁷ J.B. Ye,¹⁹ Q. Ye,¹⁷ S.C. Yeh,⁴⁸ Z.W. Yin,³⁹ J.M. You,¹⁷ N. Yunus,¹⁷ M. Yzerman,² C. Zaccardelli,³¹ P. Zemp,⁴⁶ M. Zeng,¹⁷ Y. Zeng,¹ D.H. Zhang,² Z.P. Zhang,^{19,17} B. Zhou,⁹ G.J. Zhou,⁶ J.F. Zhou,¹ R.Y. Zhu,³¹ A. Zichichi,^{7,16,17} B.C.C. van der Zwaan,²

-
- 1 I. Physikalisches Institut, RWTH, 52056 Aachen, FRG[§]
III. Physikalisches Institut, RWTH, 52056 Aachen, FRG[§]
 - 2 National Institute for High Energy Physics, NIKHEF, NL-1009 DB Amsterdam, The Netherlands
 - 3 University of Michigan, Ann Arbor, MI 48109, USA
 - 4 Laboratoire d'Annecy-le-Vieux de Physique des Particules, LAPP, IN2P3-CNRS, BP 110, F-74941 Annecy-le-Vieux CEDEX, France
 - 5 Johns Hopkins University, Baltimore, MD 21218, USA
 - 6 Institute of High Energy Physics, IHEP, 100039 Beijing, China
 - 7 INFN-Sezione di Bologna, I-40126 Bologna, Italy
 - 8 Tata Institute of Fundamental Research, Bombay 400 005, India
 - 9 Boston University, Boston, MA 02215, USA
 - 10 Northeastern University, Boston, MA 02115, USA
 - 11 Institute of Atomic Physics and University of Bucharest, R-76900 Bucharest, Romania
 - 12 Central Research Institute for Physics of the Hungarian Academy of Sciences, H-1525 Budapest 114, Hungary[†]
 - 13 Harvard University, Cambridge, MA 02139, USA
 - 14 Massachusetts Institute of Technology, Cambridge, MA 02139, USA
 - 15 INFN Sezione di Firenze and University of Florence, I-50125 Florence, Italy
 - 16 European Laboratory for Particle Physics, CERN, CH-1211 Geneva 23, Switzerland
 - 17 World Laboratory, FBLJA Project, CH-1211 Geneva 23, Switzerland
 - 18 University of Geneva, CH-1211 Geneva 4, Switzerland
 - 19 Chinese University of Science and Technology, USTC, Hefei, Anhui 230 029, China
 - 20 SEFT, Research Institute for High Energy Physics, P.O. Box 9, SF-00014 Helsinki, Finland
 - 21 University of Lausanne, CH-1015 Lausanne, Switzerland
 - 22 Los Alamos National Laboratory, Los Alamos, NM 87544, USA
 - 23 Institut de Physique Nucléaire de Lyon, IN2P3-CNRS, Université Claude Bernard, F-69622 Villeurbanne Cedex, France
 - 24 Centro de Investigaciones Energeticas, Medioambientales y Tecnológicas, CIEMAT, E-28040 Madrid, Spain
 - 25 INFN-Sezione di Milano, I-20133 Milan, Italy
 - 26 Institute of Theoretical and Experimental Physics, ITEP, Moscow, Russia
 - 27 INFN-Sezione di Napoli and University of Naples, I-80125 Naples, Italy
 - 28 Department of Natural Sciences, University of Cyprus, Nicosia, Cyprus
 - 29 University of Nymegen and NIKHEF, NL-6525 ED Nymegen, The Netherlands
 - 30 Oak Ridge National Laboratory, Oak Ridge, TN 37831, USA
 - 31 California Institute of Technology, Pasadena, CA 91125, USA
 - 32 INFN-Sezione di Perugia and Università Degli Studi di Perugia, I-06100 Perugia, Italy
 - 33 Carnegie Mellon University, Pittsburgh, PA 15213, USA
 - 34 Princeton University, Princeton, NJ 08544, USA
 - 35 INFN-Sezione di Roma and University of Rome, "La Sapienza", I-00185 Rome, Italy
 - 36 Nuclear Physics Institute, St. Petersburg, Russia
 - 37 University of California, San Diego, CA 92093, USA
 - 38 Dept. de Fisica de Particulas Elementales, Univ. de Santiago, E-15706 Santiago de Compostela, Spain
 - 39 Shanghai Institute of Ceramics, SIC, Shanghai, China
 - 40 Bulgarian Academy of Sciences, Institute of Mechatronics, BU-1113 Sofia, Bulgaria
 - 41 Center for High Energy Physics, Korea Advanced Inst. of Sciences and Technology, 305-701 Taejon, Republic of Korea
 - 42 University of Alabama, Tuscaloosa, AL 35486, USA
 - 43 Purdue University, West Lafayette, IN 47907, USA
 - 44 Paul Scherrer Institut, PSI, CH-5232 Villigen, Switzerland
 - 45 DESY-Institut für Hochenergiephysik, 15738 Zeuthen, FRG
 - 46 Eidgenössische Technische Hochschule, ETH Zürich, CH-8093 Zürich, Switzerland
 - 47 University of Hamburg, 22761 Hamburg, FRG
 - 48 High Energy Physics Group, Taiwan, China
- § Supported by the German Bundesministerium für Forschung und Technologie
† Supported by the Hungarian OTKA fund under contract number 2970.
‡ Also supported by CONICET and Universidad Nacional de La Plata, CC 67, 1900 La Plata, Argentina

References

- [1] S.L. Glashow, Nucl. Phys. **22** (1961) 579;
S. Weinberg, Phys. Rev. Lett. **19** (1967) 1264;
A. Salam, “Elementary Particle Theory”, Ed. N. Svartholm, Stockholm, “Almqvist and Wiksell” (1968), 367.
- [2] M. Gell-Mann, Acta Phys. Austriaca , Suppl. **IX** (1972) 733;
H. Fritzsch and M. Gell-Mann, 16th International Conference on High Energy Physics, Batavia, 1972; editors J.D. Jackson and A. Roberts, National Accelerator Laboratory (1972);
H. Fritzsch, M. Gell-Mann and H. Leutwyler, Phys. Lett. **B 47** (1973) 365;
D.J. Gross and F. Wilczek, Phys. Rev. Lett. **30** (1973) 1343;
D.J. Gross and F. Wilczek, Phys. Rev. **D 8** (1973) 3633;
H.D. Politzer, Phys. Rev. Lett. **30** (1973) 1346;
G. 't Hooft, Nucl. Phys. **B 33** (1971) 173.
- [3] L3 Collab., B. Adeva *et al.*, Z. Phys. **C 51** (1991) 179.
- [4] L3 Collab., O. Adriani *et al.*, Physics Reports **236** (1993) 1.
- [5] ALEPH Collab., D. Decamp *et al.*, Z. Phys. **C 53** (1992) 1;
ALEPH Collab., D. Buskulic *et al.*, Z. Phys. **C 59** (1993) 369;
ALEPH Collab., D. Buskulic *et al.*, CERN-PPE/94-30;
DELPHI Collab., P. Abreu *et al.*, Nucl. Phys. **B 367** (1991) 511;
DELPHI Collab., P. Abreu *et al.*, CERN-PPE/94-08;
DELPHI Collab., P. Abreu *et al.*, CERN-PPE/94-31;
OPAL Collab. G. Alexander *et al.*, Z. Phys. **C 52** (1991) 175;
OPAL Collab. P.D. Acton *et al.*, Z. Phys. **C 58** (1993) 219;
OPAL Collab. R. Akers *et al.*, CERN-PPE/93-146.
- [6] L3 Collab., B. Adeva *et al.*, Nucl. Inst. Meth. **A 289** (1990) 35.
- [7] R. Brun *et al.*, “GEANT 3”, CERN DD/EE/84-1 (Revised), September 1987.
- [8] H. Fesefeldt, RWTH Aachen Preprint PITHA 85/02 (1985).
- [9] S. Jadach and B.F.L. Ward, Phys. Rev. **D 40** (1989) 3582.
- [10] S. Jadach *et al.*, Phys. Lett. **B 268** (1991) 253;
S. Jadach *et al.*, Comp. Phys. Comm. **70** (1992) 305.
- [11] M. Böhm, A. Denner and W. Hollik, Nucl. Phys. **B 304** (1988) 687;
F.A. Berends, R. Kleiss and W. Hollik, Nucl. Phys. **B 304** (1988) 712.
- [12] F.A. Berends and R. Kleiss, Nucl. Phys. **B 186** (1981) 22.
- [13] W. Beenakker and B. Pietrzyk, Preprint CERN-TH.6760/92, CERN, 1992.
- [14] O. Adriani *et al.*, Nucl. Inst. Meth. **A 302** (1991) 53.
- [15] T. Sjöstrand, Comp. Phys. Comm. **39** (1986) 347;
T. Sjöstrand and M. Bengtsson, Comp. Phys. Comm. **43** (1987) 367.

- [16] G. Marchesini and B. Webber, Nucl. Phys. **B 310** (1988) 461;
G. Marchesini *et al.*, Comp. Phys. Comm. **67** (1992) 465.
- [17] S. Jadach, B.F.L. Ward and Z. Wąs, Comp. Phys. Comm. **66** (1991) 276.
- [18] F.A. Berends, P.H. Daverveldt and R. Kleiss, Nucl. Phys. **B 253** (1985) 441.
- [19] D. Bardin *et al.*, FORTRAN package ZFITTER, and preprint CERN-TH. 6443/92;
D. Bardin *et al.*, Z. Phys. **C 44** (1989) 493;
D. Bardin *et al.*, Nucl. Phys. **B 351** (1991) 1;
D. Bardin *et al.*, Phys. Lett. **B 255** (1991) 290;
J. Fleischer *et al.*, Phys. Lett. **B 293** (1992) 437;
S. Jadach *et al.*, Phys. Lett. **B 280** (1992) 129;
B. Kniehl *et al.*, Phys. Lett. **B 209** (1988) 337;
R. Barbieri *et al.*, CERN-TH-6713-92.
- [20] J.H. Field, Preprint UGVA-DPNC 1993/9-160, University of Geneva, 1993, to be published in Phys. Lett. B.
- [21] W. Beenakker, F.B. Berends and S.C. van der Marck, Nucl. Phys. **B 349** (1991) 323.
- [22] The working group on LEP energy, L. Arnaudon *et al.*,
Preprint CERN-PPE/92-125, CERN, 1992; Preprint CERN-SL/93-21 (DI), CERN, 1993.
- [23] L3 Collab., O. Adriani *et al.*, Phys. Lett. **B 315** (1993) 494.
- [24] The LEP Collaborations, Phys. Lett. **B 307** (1993) 187.
- [25] The LEP collaborations: ALEPH, DELPHI, L3, OPAL and the LEP Electroweak Working Group, Updated Parameters of the Z Resonance from Combined Preliminary Data of the LEP Experiments, Preprint CERN-PPE/93-157, CERN, 1993.
- [26] F.A. Berends *et al.*, in “Z Physics at LEP 1”, CERN Report CERN 89-08 (1989), eds G. Altarelli, R. Kleiss and C. Verzegnassi, Vol. 1, p. 89.
- [27] M. Böhm *et al.*, in “Z Physics at LEP 1”, CERN Report CERN 89-08 (1989), eds G. Altarelli, R. Kleiss and C. Verzegnassi, Vol. 1, p. 203.
- [28] M. Consoli *et al.*, in “Z Physics at LEP 1”, CERN Report CERN 89-08 (1989), eds G. Altarelli, R. Kleiss and C. Verzegnassi, Vol. 1, p. 7.
- [29] G. Burgers *et al.*, in “Z Physics at LEP 1”, CERN Report CERN 89-08 (1989), eds G. Altarelli, R. Kleiss and C. Verzegnassi, Vol. 1, p. 55.
- [30] F. James, CERN Program Library Long Writeup D506 MINUIT, CERN, 1993.
- [31] G. Isidori, Phys. Lett. **B 314** (1993) 139.
- [32] M. Grünewald, S. Kirsch, Preprint CERN-PPE/93-188, CERN, 1993.
- [33] L3 Collab., B. Adeva *et al.*, Phys. Lett. **B 275** (1992) 209;
L3 Collab., O. Adriani *et al.*, Phys. Lett. **B 292** (1992) 463;
OPAL Collab, M.Z. Akrawy *et al.*, Z. Phys. **C 50** (1991) 373;
ALEPH Collab., D. Buskulic *et al.*, Phys. Lett. **B 313** (1993) 520.

- [34] S. Jadach *et al.*, in “Z Physics at LEP 1”, CERN Report CERN 89-08 (1989), eds G. Altarelli, R. Kleiss and C. Verzegnassi, Vol. 1, p. 235.
- [35] L3 Collab., O. Adriani *et al.*, Phys. Lett. **B 294** (1992) 466.
- [36] J. Kühn *et al.*, in “Z Physics at LEP 1”, CERN Report CERN 89-08 (1989), eds G. Altarelli, R. Kleiss and C. Verzegnassi, Vol. 1, p. 267.
- [37] L3 Collab., O. Adriani *et al.*, Phys. Lett. **B 292** (1992) 454.
- [38] L3 Collab., O. Adriani *et al.*, Phys. Lett. **B 307** (1993) 237.
- [39] G. Passarino, Phys. Lett. **B 313** (1993) 213.
- [40] P. Tipton, *The Top Search at CDF*; N. Hadley, *The Top Search at D0*;
Talks presented at the 1993 International Symposium on Lepton-Photon Interactions at High Energies, Cornell, August 10-15, to appear in the proceedings.
- [41] CDF Collab., F. Abe *et al.*, Phys. Rev. Lett. **65** (1990) 2243.
CDF Collab., F. Abe *et al.*, Phys. Rev. **D 43** (1991) 2070.
UA2 Collab., J. Alitti *et al.*, Phys. Lett. **B 276** (1992) 354.
- [42] G. Altarelli and R. Barbieri, Phys. Lett. **B 253** (1990) 161;
G. Altarelli, R. Barbieri and S. Jadach, Nucl. Phys. **B 369** (1993) 3;
G. Altarelli, R. Barbieri and F. Caravaglios, Preprint CERN-TH. 6770/93, CERN, 1993.

List of Figures

- 1 Distributions of variables used for the selection of luminosity $e^+e^- \rightarrow e^+e^-(\gamma)$ events, comparing the 1992 data to the simulated Monte-Carlo Bhabha events. Only the statistical errors on the data are shown. The statistical errors on the Monte-Carlo simulation are approximately twice as large. (a) The average reconstructed radial impact coordinate, $(R_{+z} + R_{-z})/2$. The wiggles in the distributions are due to the changing angular resolution across the face of each crystal. (b) The maximum of the reconstructed energies in the two luminosity calorimeters, E_{\max} , normalized to the beam energy, E_{beam} . The position of the selection cut is indicated by the vertical arrow. For energies below the cut, the errors on the data points are large, because the background, which has been subtracted, is significant.
- 2 The energy of photon candidates in radiative luminosity Bhabha events, E_γ , normalized to the beam energy, and compared to the simulated Monte-Carlo Bhabha events. Only the statistical errors on the data are shown. The statistical errors on the Monte-Carlo simulation are approximately twice as large.
- 3 Distributions of variables used for the selection of $e^+e^- \rightarrow \text{hadrons}(\gamma)$ events, comparing the 1992 data to the simulated signal and background Monte-Carlo events. The position of the selection cuts are indicated by vertical arrows. (a) The total visible energy, E_{vis} , normalized to the center-of-mass energy, \sqrt{s} , for hadronic events. (b) The parallel energy imbalance, $|E_{\parallel}|$, normalized to the visible energy. (c) The perpendicular energy imbalance, E_{\perp} , normalized to the visible energy. (d) The number of reconstructed calorimetric clusters, N_{clusters} , for events with the thrust axis in the barrel region ($|\cos \theta_t| \leq 0.74$).
- 4 A high energy muon seen in the different subdetectors of L3, with a track in the central tracking chamber (TEC), a low energy cluster in the electromagnetic calorimeter (BGO), a hit in the scintillation counters (SCNT), a track of low energy hits in the hadron calorimeter (HCAL) and hits in the inner muon chamber (MUCH).
- 5 Distributions of variables used for the selection of $e^+e^- \rightarrow \mu^+\mu^-(\gamma)$ events, comparing the 1992 data to the simulated signal and background Monte-Carlo events. The position of the selection cuts are indicated by vertical arrows. (a) The $\cos \theta$ values for both muons of an event, showing the muons identified in the muon spectrometer (87.6%) and the muons identified as MIPs (12.4%). (b) The maximum reconstructed muon momentum for events with at least one reconstructed track in the muon chambers, P_{\max} , normalized to the beam energy. (c) The acollinearity angle, ξ , between the directions of the two muons for events with at least one reconstructed track in the muon chambers. (d) Same as (c) for events with no reconstructed track in the muon chambers.

- 6 The differential cross section, $d\sigma_\mu/d\cos\theta$, as a function of the polar scattering angle, $\cos\theta$, of the final-state fermion for $e^+e^- \rightarrow \mu^+\mu^-(\gamma)$ events on the Z peak (1992 data).
- 7 Distributions of variables used for the selection of $e^+e^- \rightarrow \tau^+\tau^-(\gamma)$ events, comparing the 1992 data to the simulated signal and background Monte-Carlo events. The position of the selection cuts are indicated by vertical arrows. (a) The acollinearity angle, ξ , between the directions of the two highest energy jets. (b) The maximal separation in azimuth, $\Delta\phi$, between a track in the central tracking chamber and the nearest jet.
- 8 The differential cross section, $d\sigma_\tau/d\cos\theta$, as a function of the polar scattering angle, $\cos\theta$, of the final-state fermion for $e^+e^- \rightarrow \tau^+\tau^-(\gamma)$ events on the Z peak (1992 data).
- 9 Distributions of variables used for the selection of $e^+e^- \rightarrow e^+e^-(\gamma)$ events, comparing the 1992 data to the simulated signal and background Monte-Carlo events. The position of the selection cuts are indicated by vertical arrows. (a) The energy of the highest energy cluster in the electromagnetic calorimeter, E_{\max} , normalized to the beam energy. (b) The energy sum of the four highest energy clusters in the electromagnetic calorimeter, E_{BGO} , normalized to the center-of-mass energy. The background at (a) $E_{\max} \approx E_{\text{beam}}$ and (b) $E_{\text{BGO}} \approx \sqrt{s}$ is due to the process $e^+e^- \rightarrow \gamma\gamma(\gamma)$.
- 10 Distributions of quantities used for the charge assignment in $e^+e^- \rightarrow e^+e^-(\gamma)$ events. (a) Scatter plot of $\sin\Delta\phi$ versus $\Delta\rho$ (defined in the text) for all events selected for the forward-backward asymmetry measurement. The upper right cluster, C_+ , corresponds to events with the higher energy cluster being a positron, the lower left cluster, C_- , to events where it is an electron. (b) Distribution of the quantity $\mathcal{P} = d_-/(d_+ + d_-)$ calculated from the weighted distances, d_\pm , of the event to the centers of the two clusters, C_\pm , as explained in the text.
- 11 The differential cross section, $d\sigma_e/d\cos\theta$, as a function of the polar scattering angle, $\cos\theta$, of the final-state fermion for $e^+e^- \rightarrow e^+e^-(\gamma)$ events on the Z peak (1992 data).
- 12 The correlation between the mass of the Z boson, m_Z , and the hadronic γZ -interference term, J_{had} . The 68% and 95% confidence-level contours for the two parameters are shown. The band shows the prediction for J_{had} according to the SM, using $\alpha_s = 0.123 \pm 0.006$ and taking $m_t = 150 \pm 50$ GeV, $m_H = 300_{-240}^{+700}$ GeV.
- 13 The cross section, $\sigma_{\text{had}}(s)$, for the process $e^+e^- \rightarrow \text{hadrons}(\gamma)$ as a function of \sqrt{s} . Points with error bars are the measured values. The solid line is the result of the fit to the combined cross-section and forward-backward asymmetry data, assuming lepton universality. Also shown is the ratio of the measured cross section to the fitted cross section for all center-of-mass energy points.

- 14 The cross section, $\sigma_\mu(s)$, for the process $e^+e^- \rightarrow \mu^+\mu^-(\gamma)$ as a function of \sqrt{s} . Points with error bars are the measured values. The solid line is the result of the fit to the combined cross-section and forward-backward asymmetry data, assuming lepton universality. Also shown is the ratio of the measured cross section to the fitted cross section for all center-of-mass energy points.
- 15 The cross section, $\sigma_\tau(s)$, for the process $e^+e^- \rightarrow \tau^+\tau^-(\gamma)$ as a function of \sqrt{s} . Points with error bars are the measured values. The solid line is the result of the fit to the combined cross-section and forward-backward asymmetry data, assuming lepton universality. Also shown is the ratio of the measured cross section to the fitted cross section for all center-of-mass energy points.
- 16 The cross section, $\sigma_e(s)$, for the process $e^+e^- \rightarrow e^+e^-(\gamma)$ as a function of \sqrt{s} . Points with error bars are the measured values. The solid line is the result of the fit to the combined cross-section and forward-backward asymmetry data, assuming lepton universality. The lines showing the contributions of the s channel, t channel and s/t interference are computed with the ALIBABA program. Also shown is the ratio of the measured cross section to the fitted cross section for all center-of-mass energy points.
- 17 The forward-backward asymmetry, $A_{\text{fb}}^\mu(s)$, for the process $e^+e^- \rightarrow \mu^+\mu^-(\gamma)$ as a function of \sqrt{s} . Points with error bars are the measured values. The solid curve is the result of the fit to the combined cross-section and forward-backward asymmetry data, assuming lepton universality.
- 18 The forward-backward asymmetry, $A_{\text{fb}}^\tau(s)$, for the process $e^+e^- \rightarrow \tau^+\tau^-(\gamma)$ as a function of \sqrt{s} . Points with error bars are the measured values. The solid curve is the result of the fit to the combined cross-section and forward-backward asymmetry data, assuming lepton universality.
- 19 The forward-backward asymmetry, $A_{\text{fb}}^e(s)$, for the process $e^+e^- \rightarrow e^+e^-(\gamma)$ as a function of \sqrt{s} . Points with error bars are the measured values. The solid curve is the result of the fit to the combined cross-section and forward-backward asymmetry data, assuming lepton universality. The lines showing the contributions of the s channel, $\sigma_f^s - \sigma_b^s$, t channel, $\sigma_f^t - \sigma_b^t$, and s/t interference, $\sigma_f^{s/t} - \sigma_b^{s/t}$, normalized to the total cross section, $\sigma^s + \sigma^t + \sigma^{s/t}$, are computed with the ALIBABA program.
- 20 Correlation between the effective coupling constants of the neutral weak current, \bar{g}_V and \bar{g}_A , for charged leptons. The 68% confidence level contours for the two parameters are shown, for each lepton species separately (solid contours), and under the assumption of lepton universality (dotted contour). The band shows the prediction according to the SM, using the fitted Z mass, $m_Z = 91.195 \pm 0.009$ GeV, $\alpha_s = 0.123 \pm 0.006$ and taking $m_t = 150 \pm 50$ GeV, $m_H = 300_{-240}^{+700}$ GeV.

- 21 Correlation between the strong coupling constant, α_s , and the mass of the top quark, m_t , with m_H fixed to 300 GeV. The 68% and 95% confidence level contours for the two parameters are shown, together with our measurement of α_s from hadronic event topologies and tau decays ($\alpha_s = 0.123 \pm 0.006$), and the limit on m_t from direct searches ($m_t > 113$ GeV).
- 22 Correlation between the parameters ϵ_1 and ϵ_3 (see text). The 68% and 95% confidence level contours for the two parameters are shown. The band shows the prediction according to the SM, using the fitted Z mass, $m_Z = 91.195 \pm 0.009$ GeV, $\alpha_s = 0.123 \pm 0.006$ and taking $m_t = 150 \pm 50$ GeV, $m_H = 300_{-240}^{+700}$ GeV.

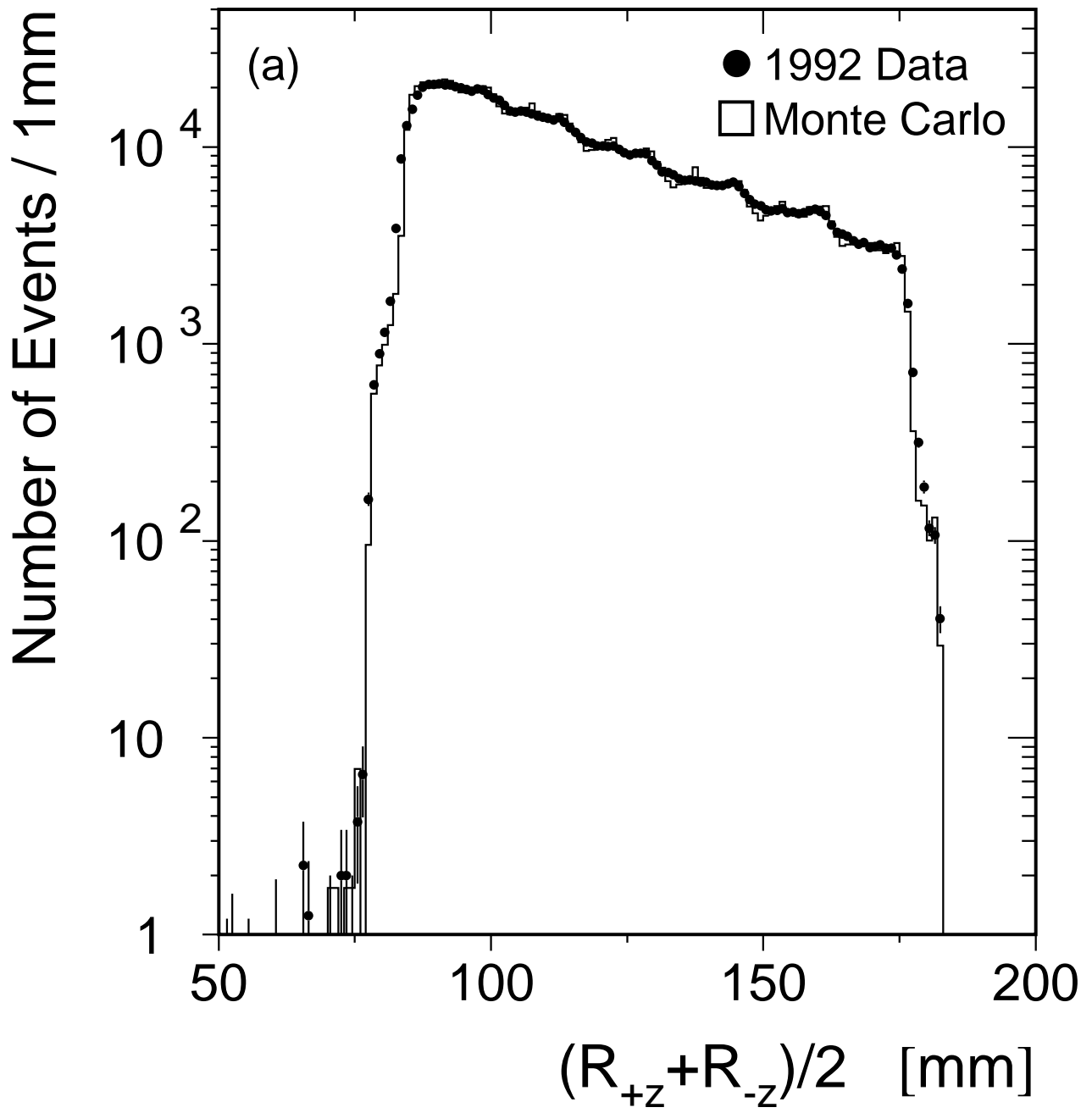


Figure 1a

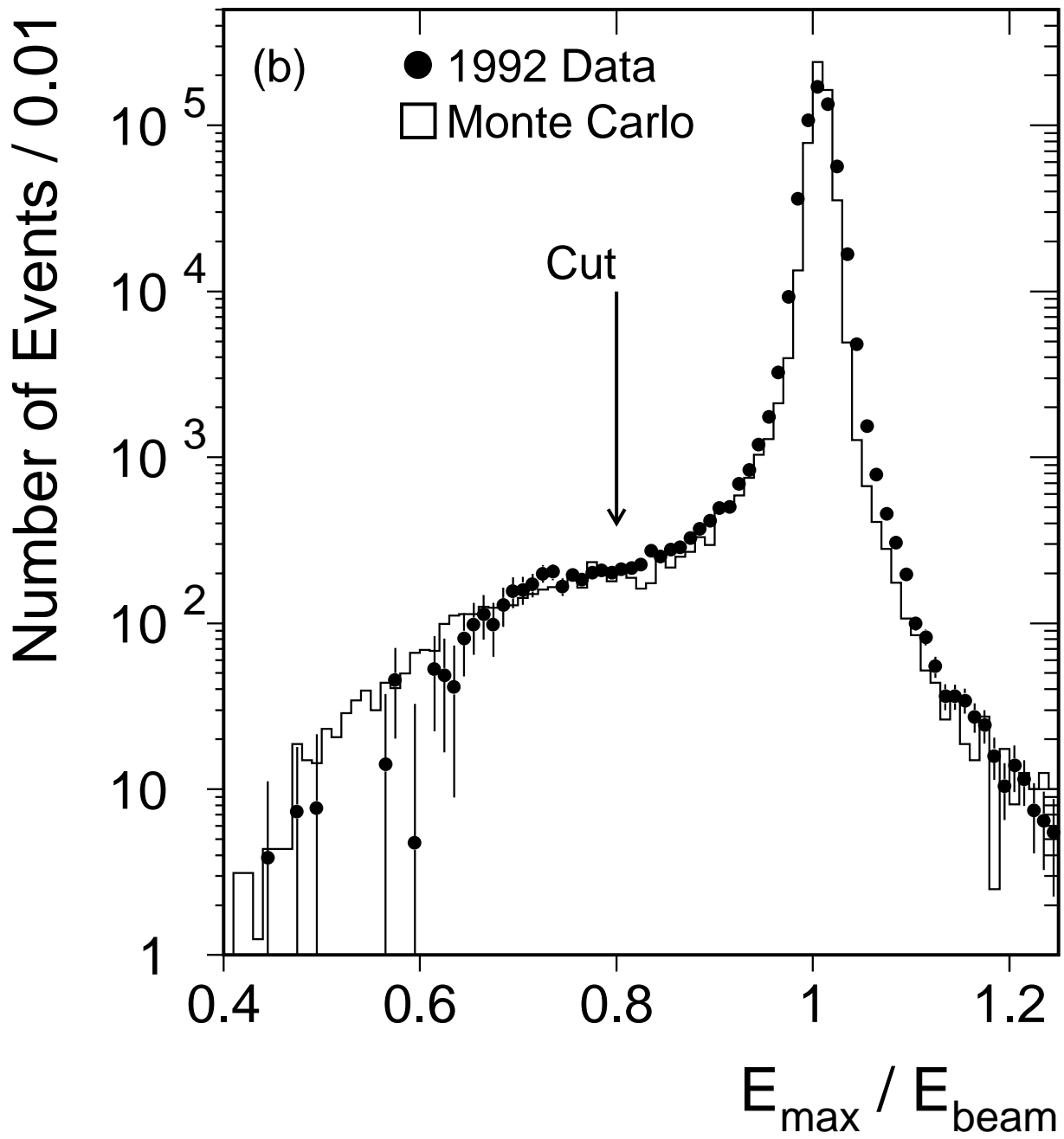


Figure 1b

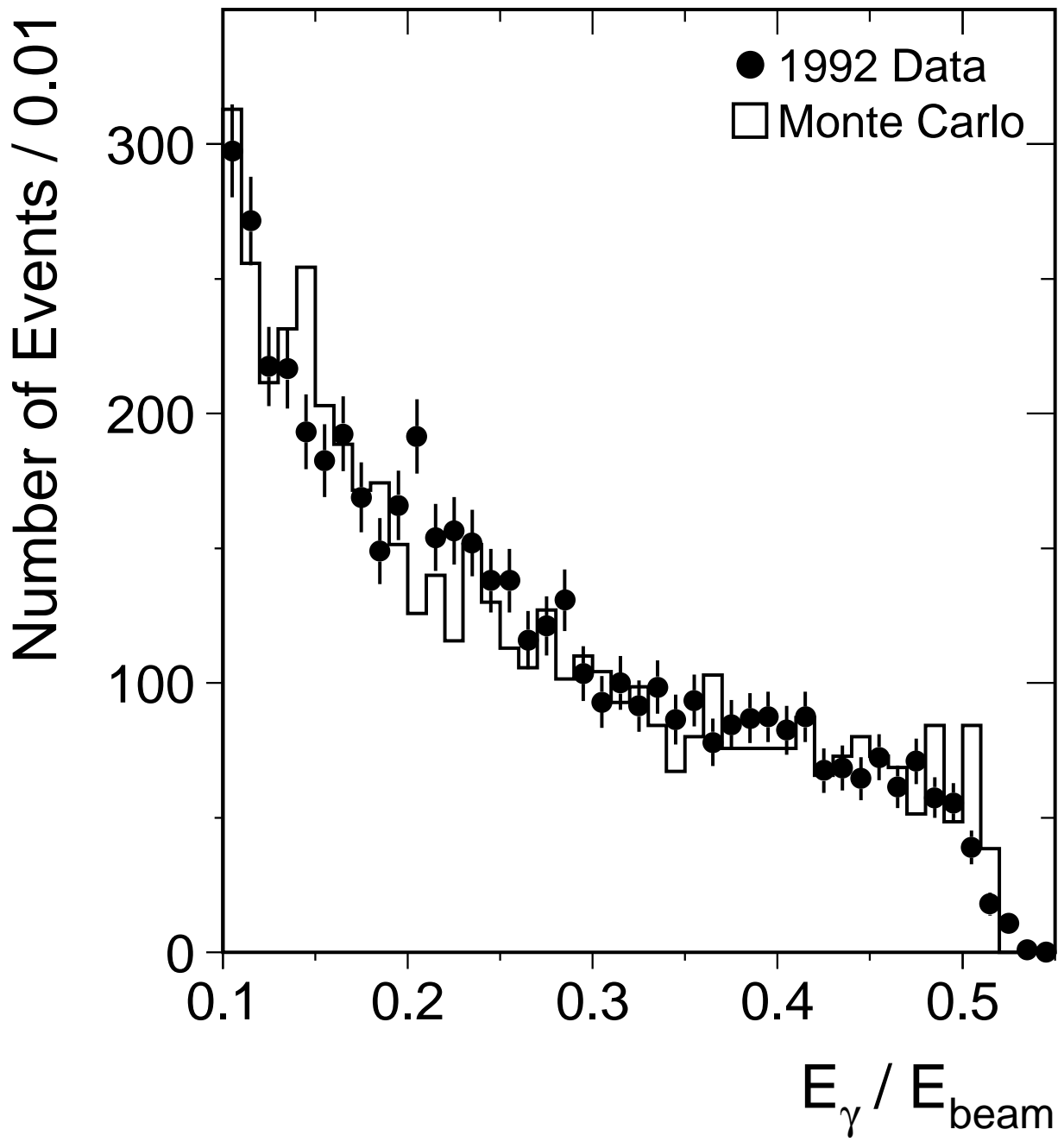


Figure 2

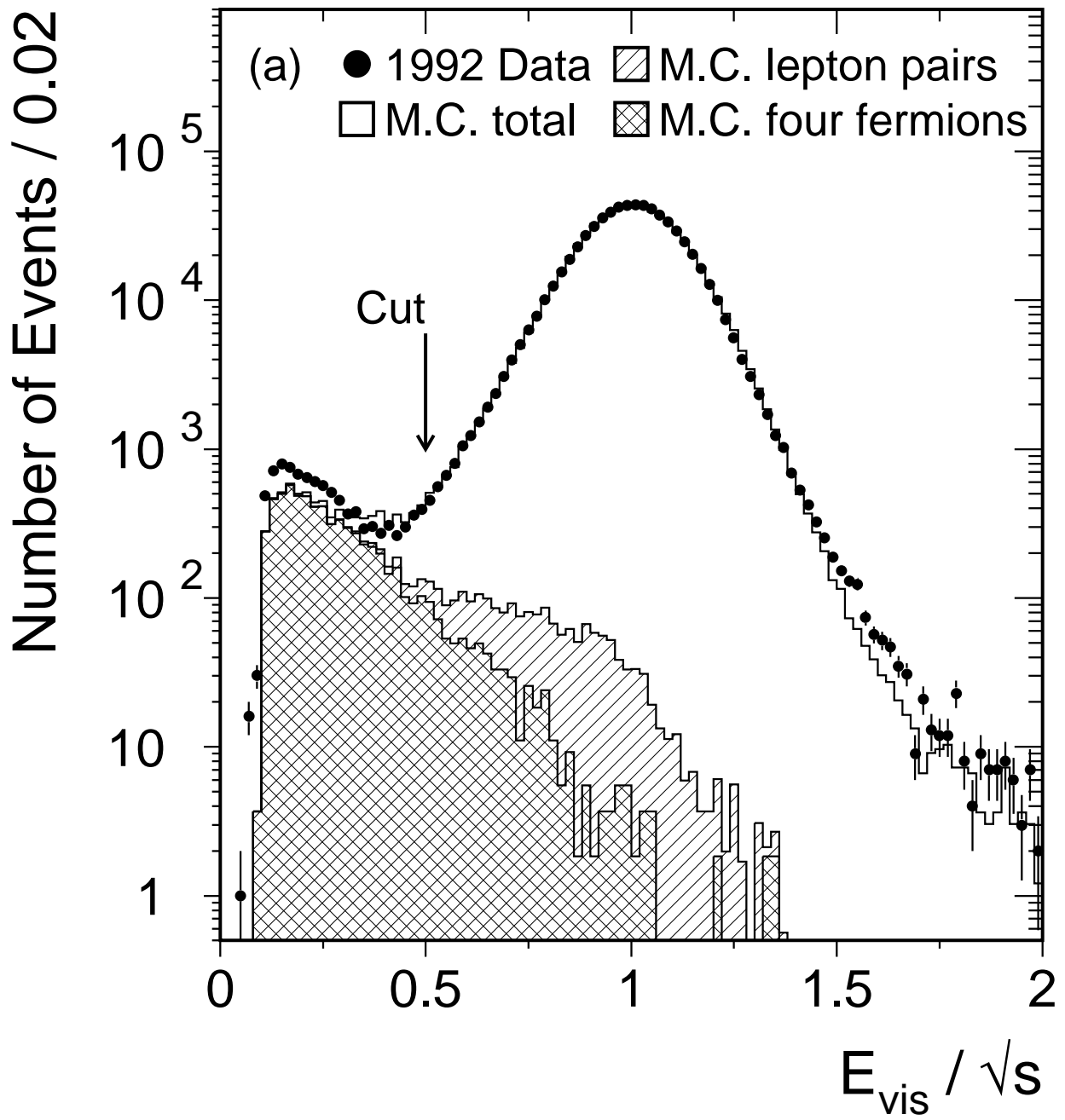


Figure 3a

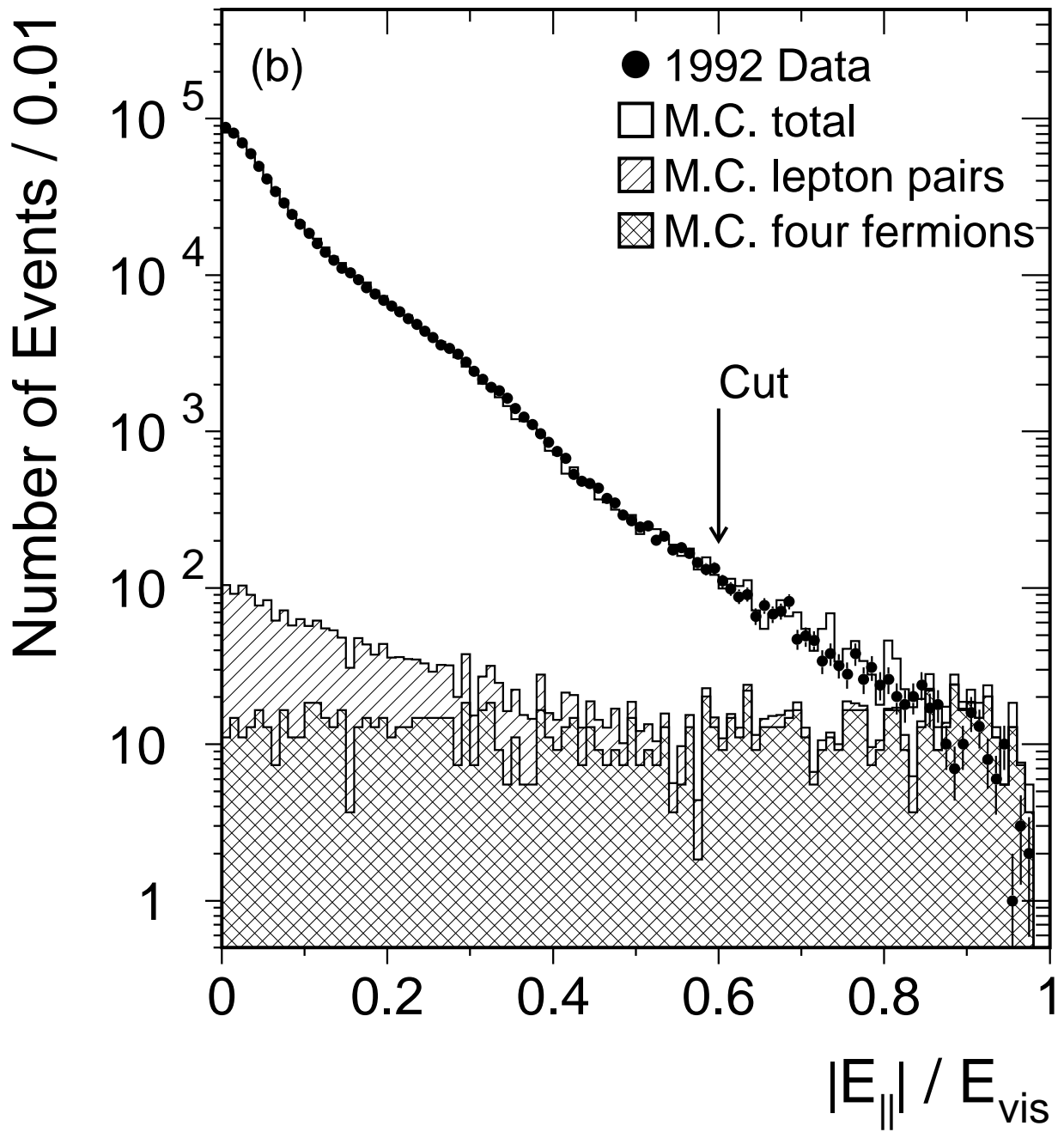


Figure 3b

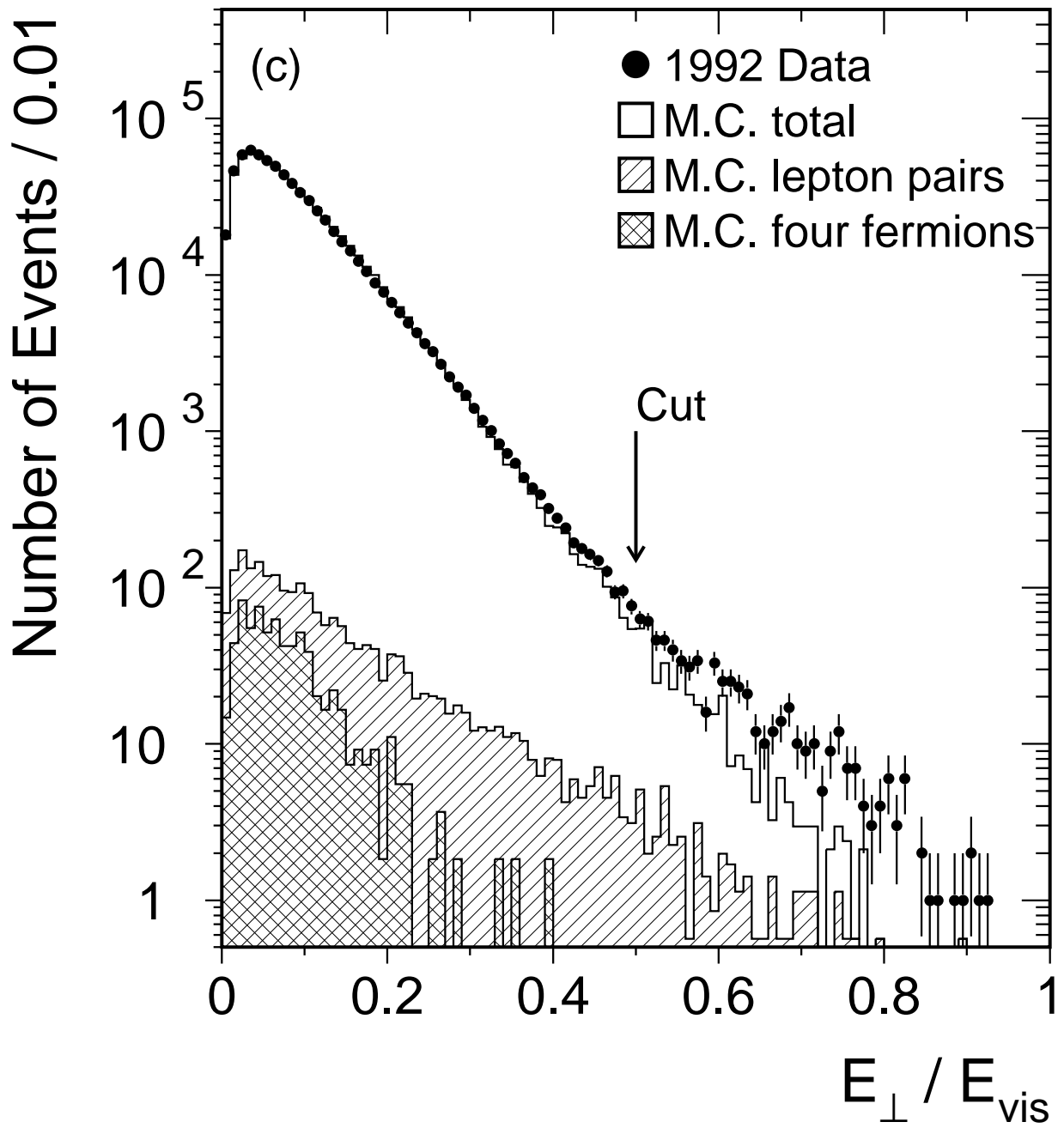


Figure 3c

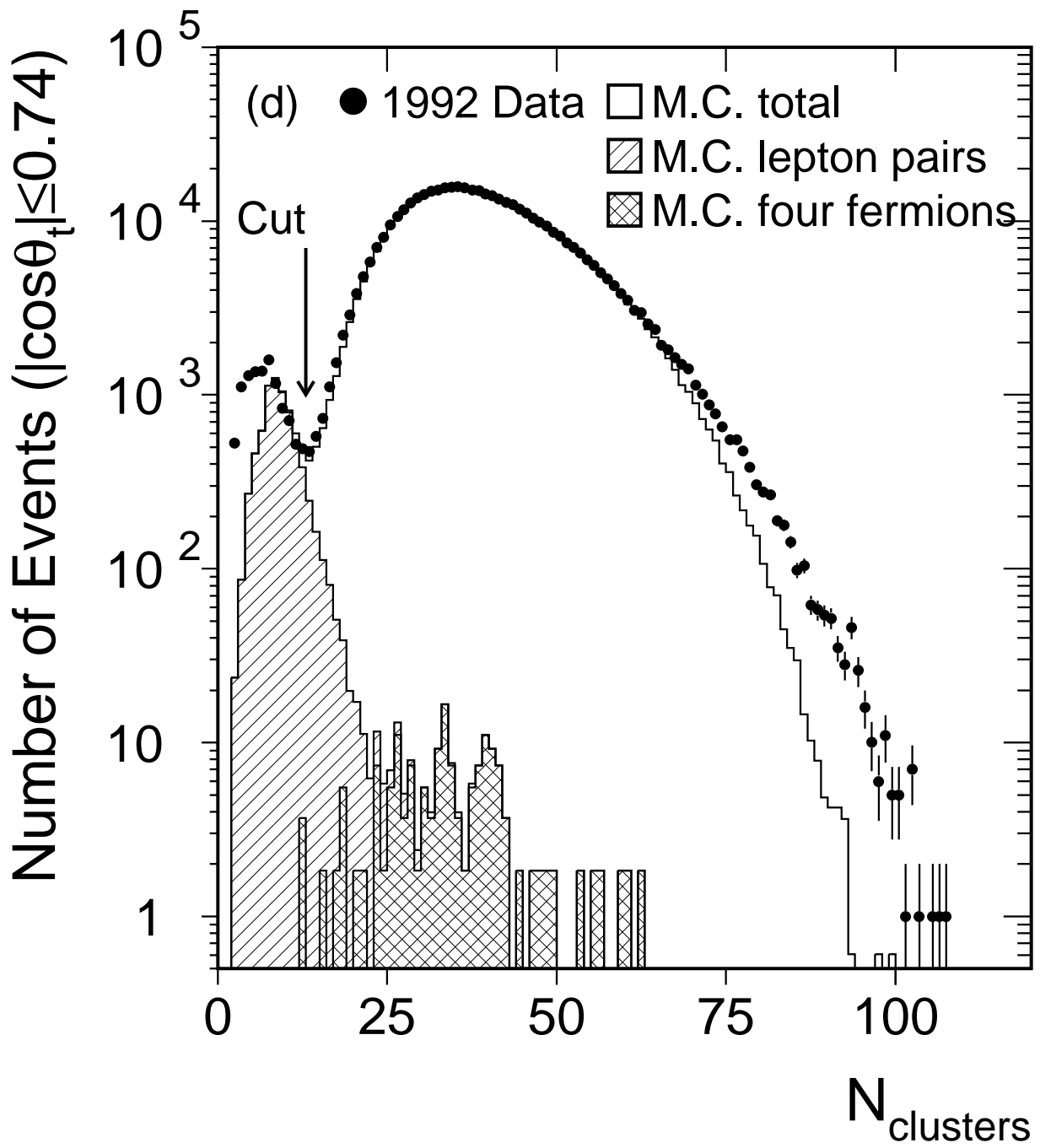


Figure 3d

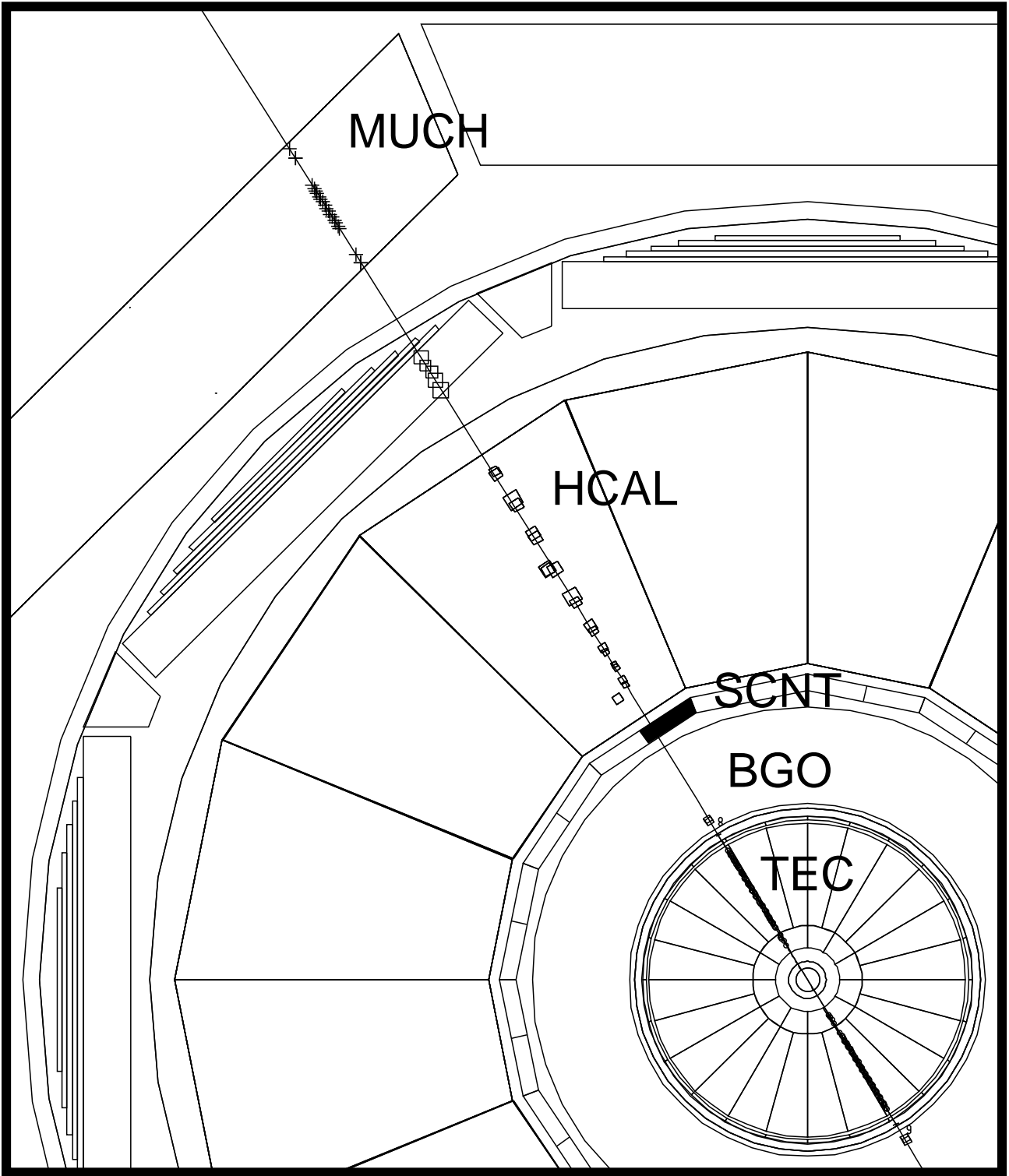


Figure 4

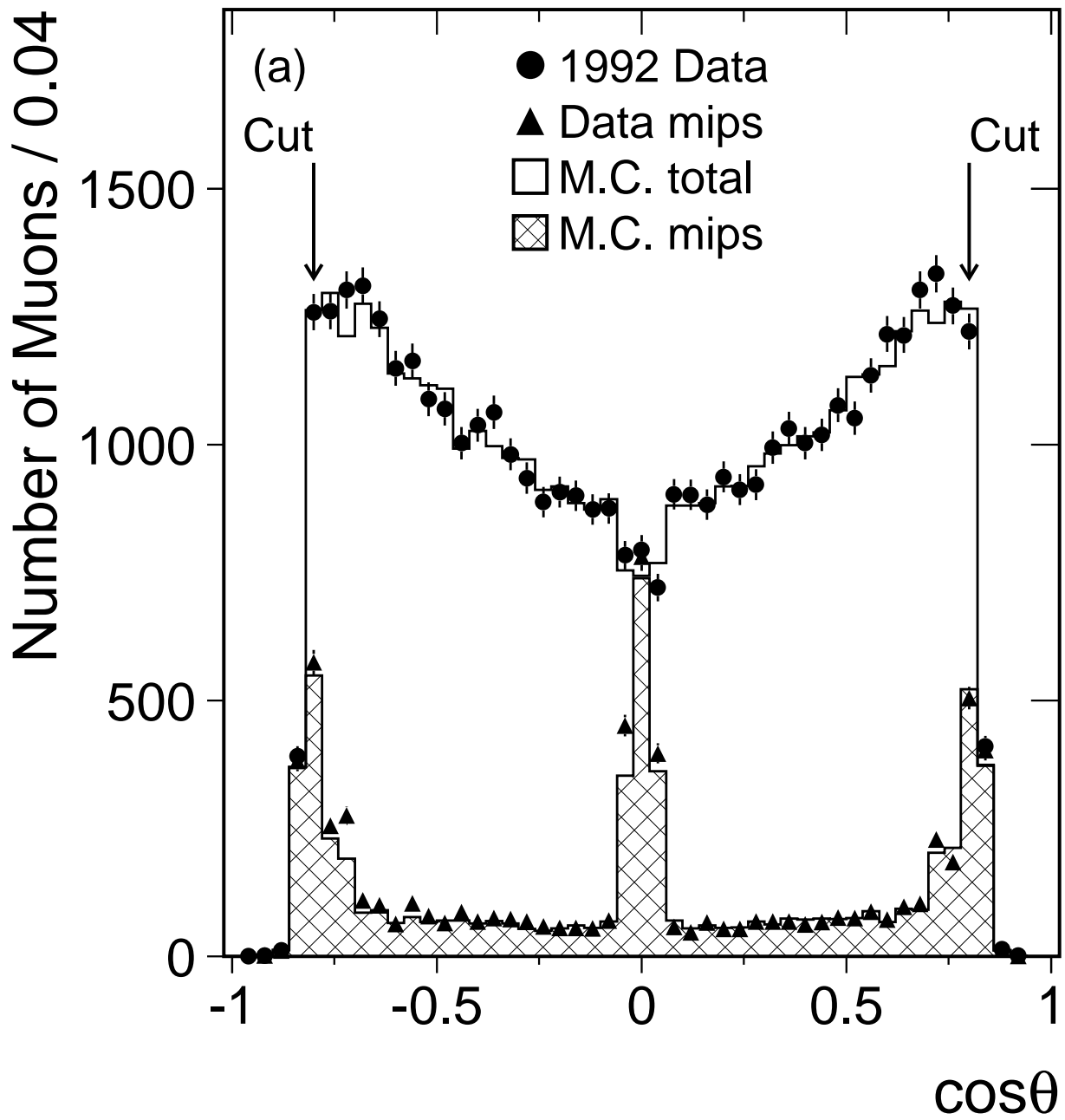


Figure 5a

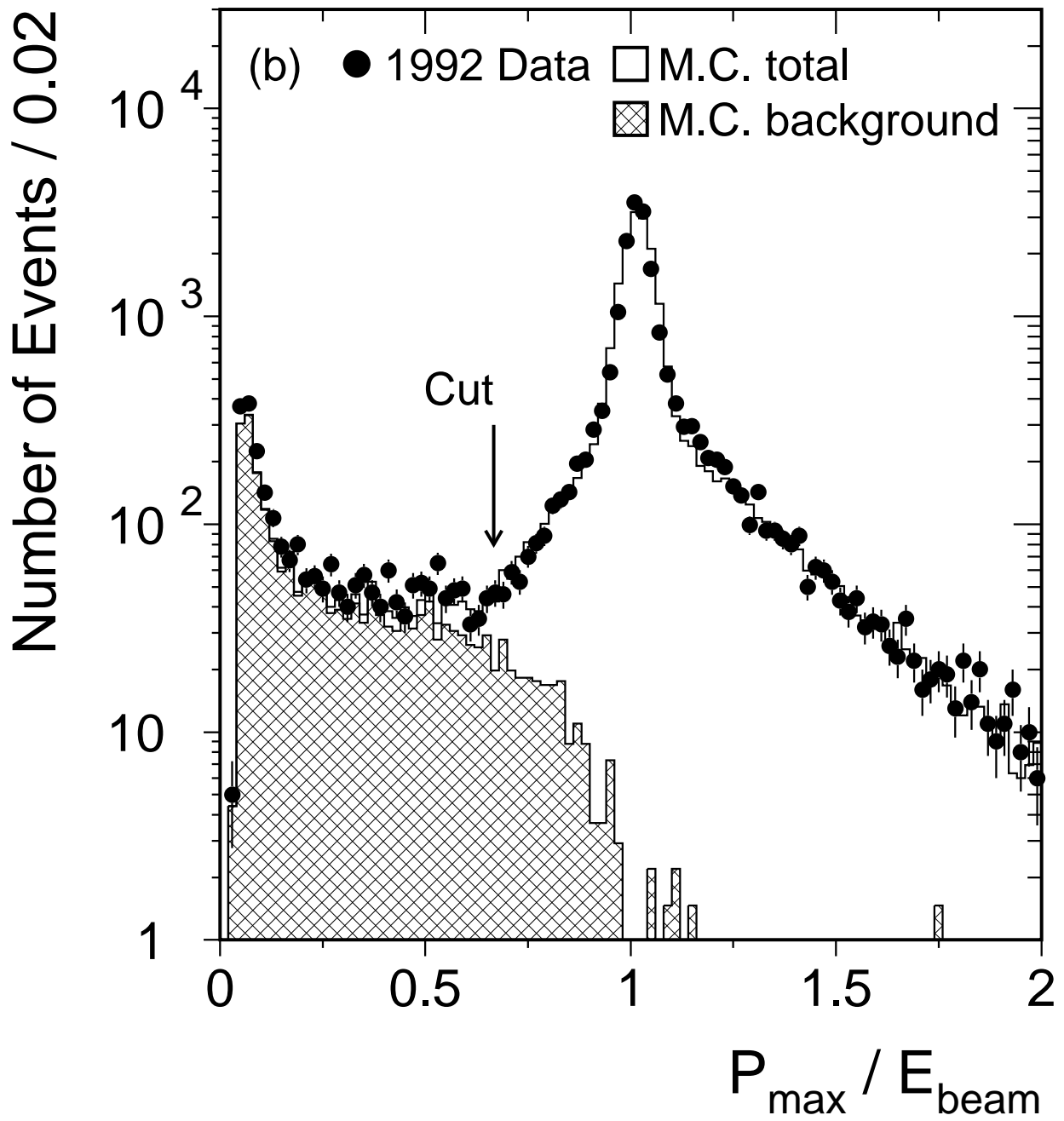


Figure 5b

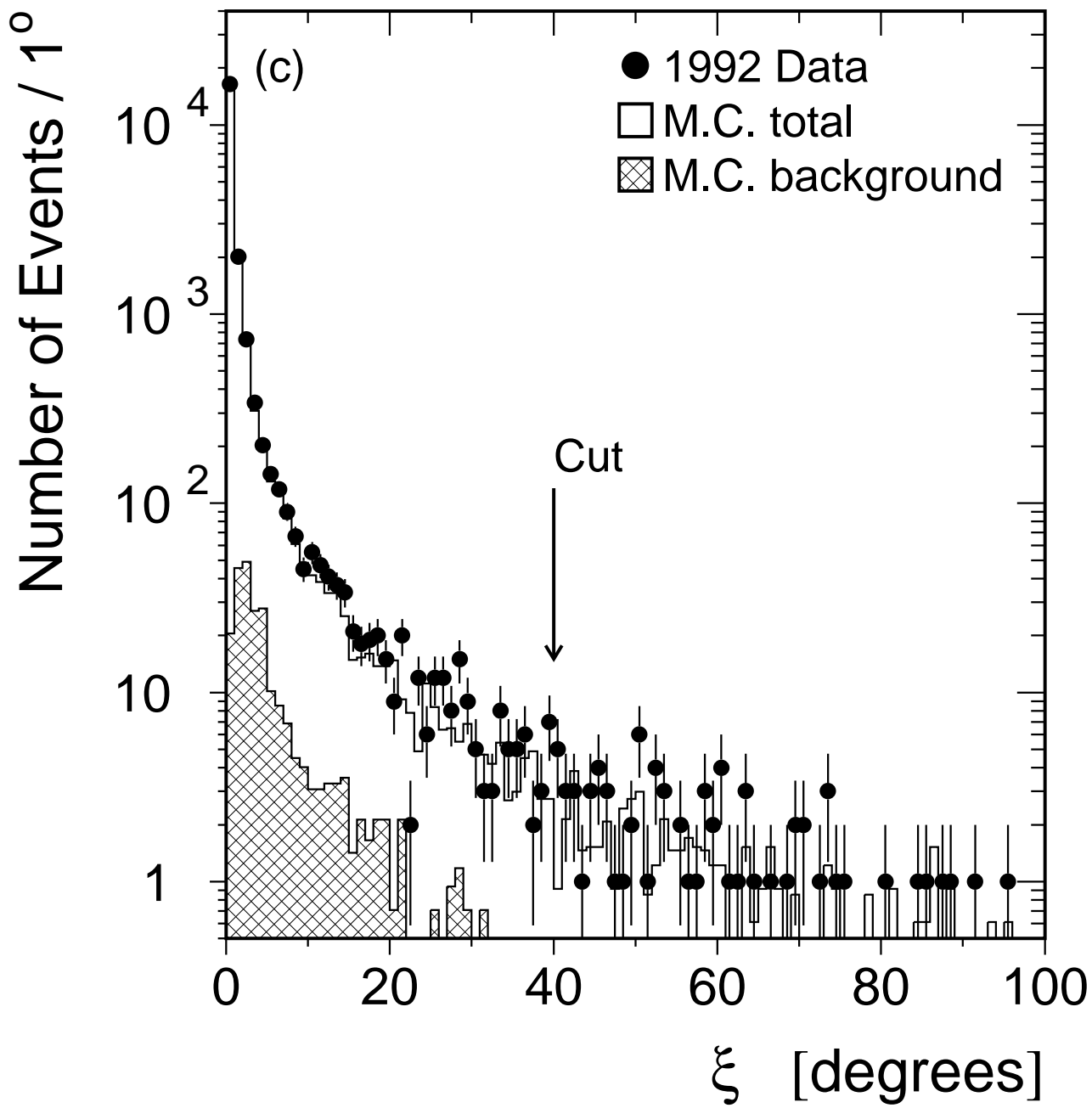


Figure 5c

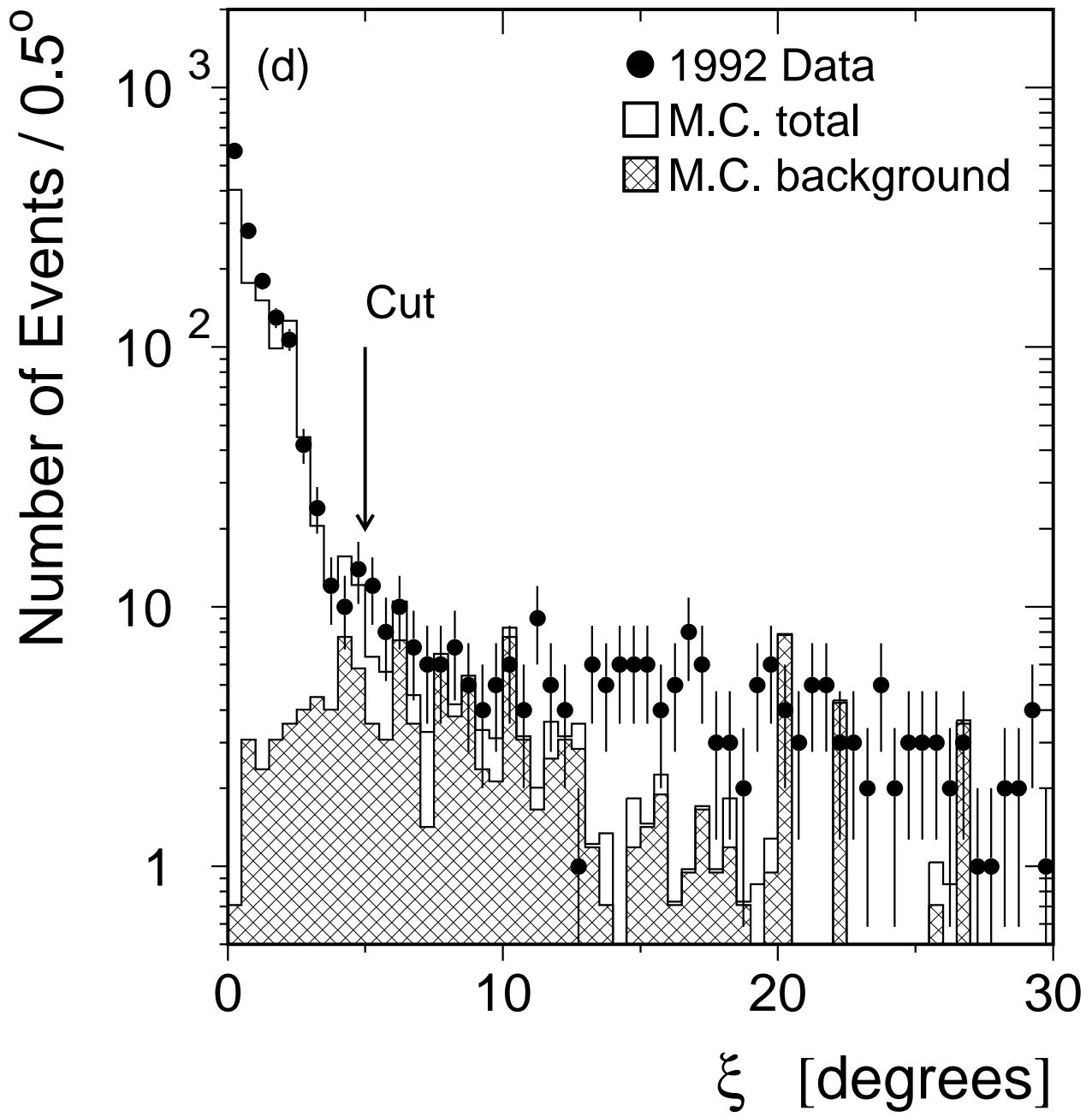


Figure 5d

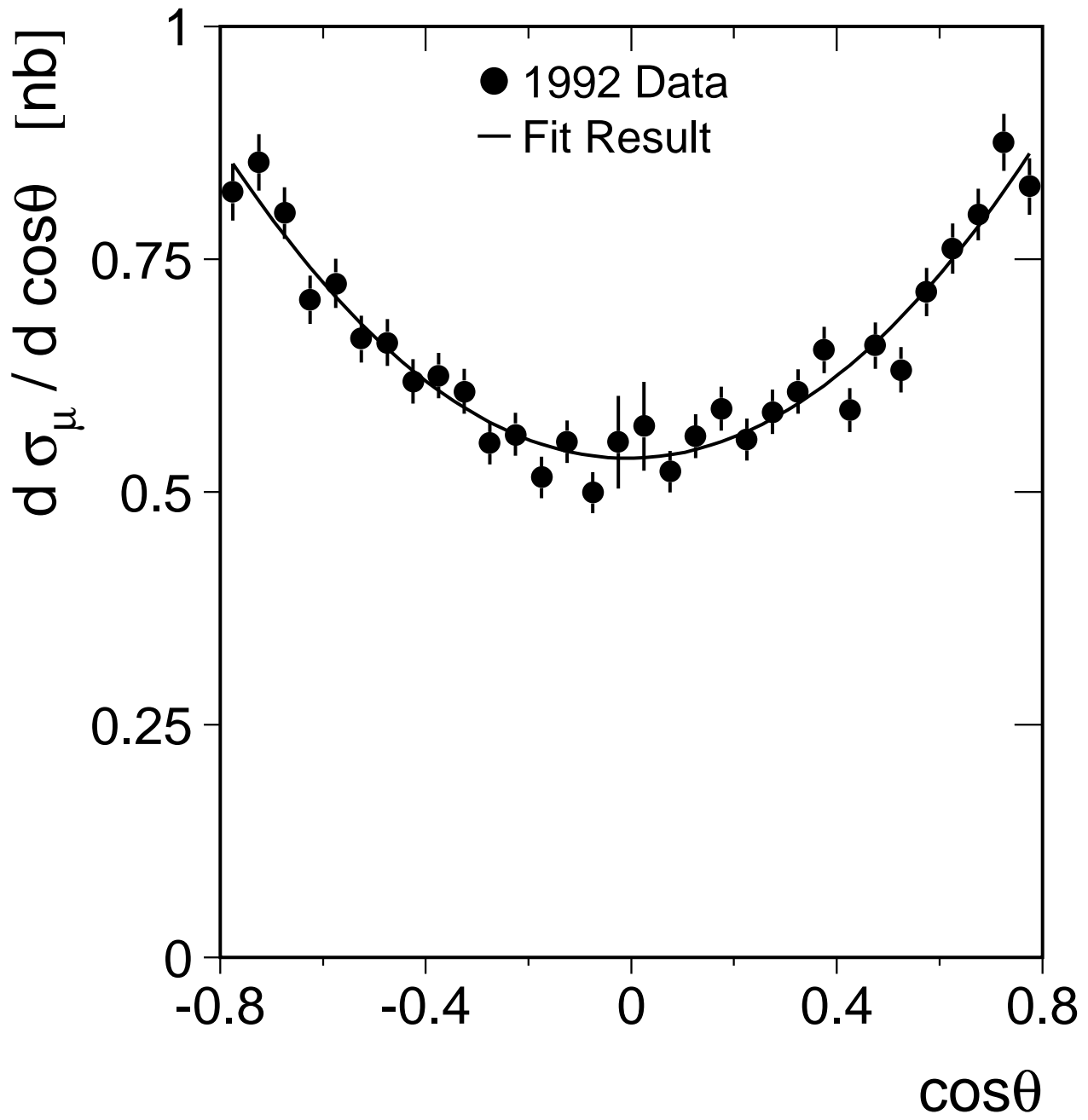


Figure 6

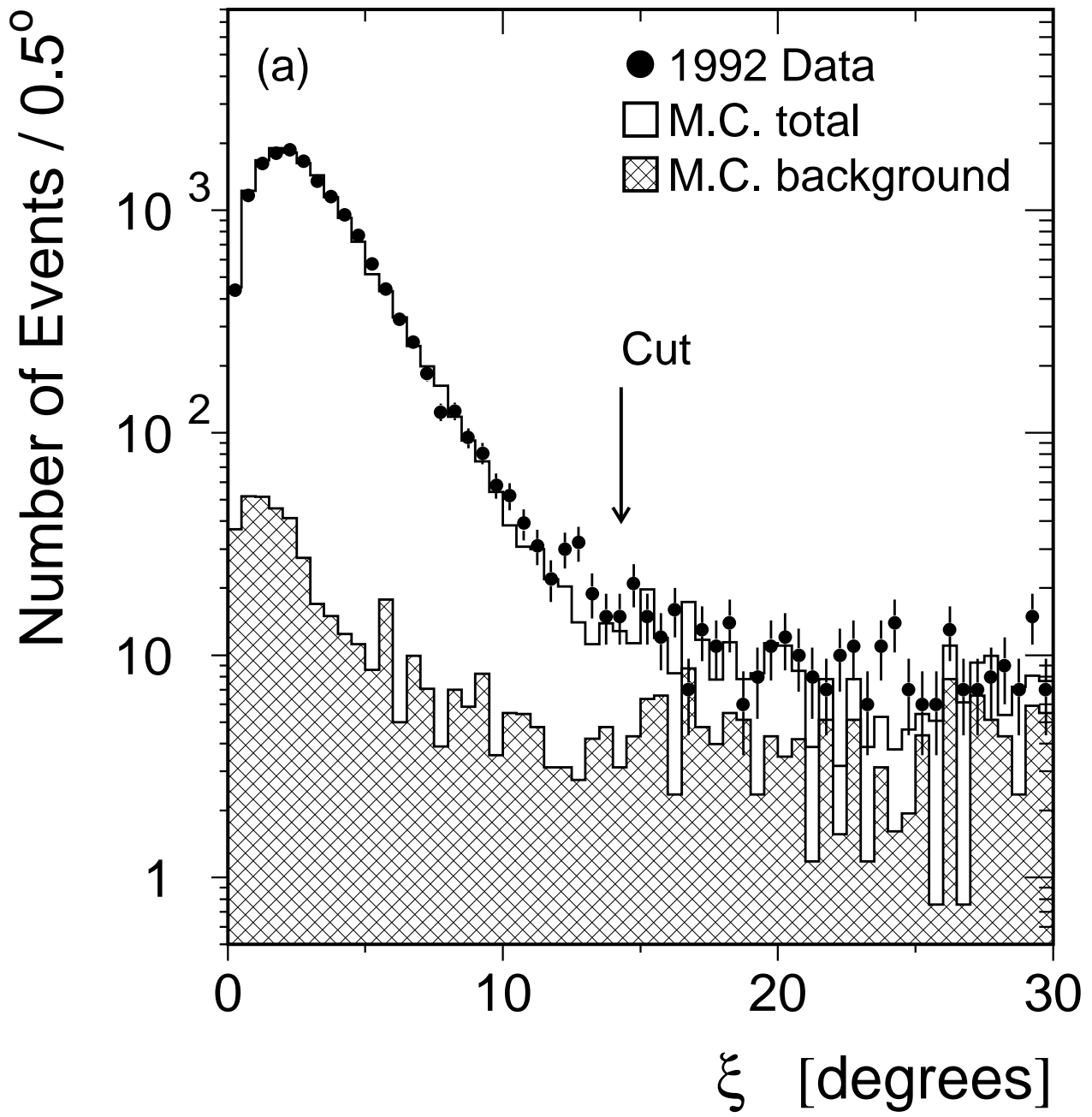


Figure 7a

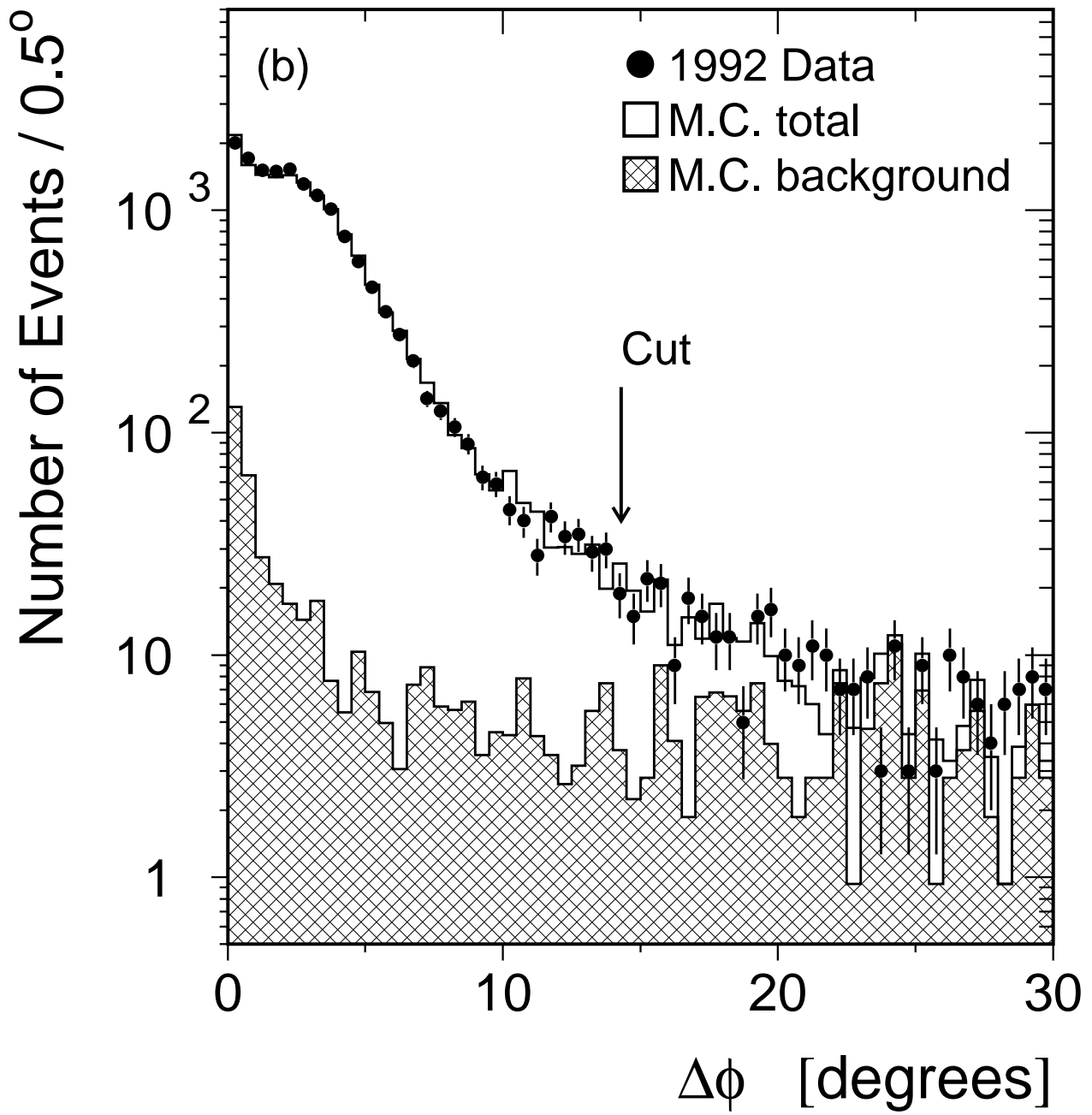


Figure 7b

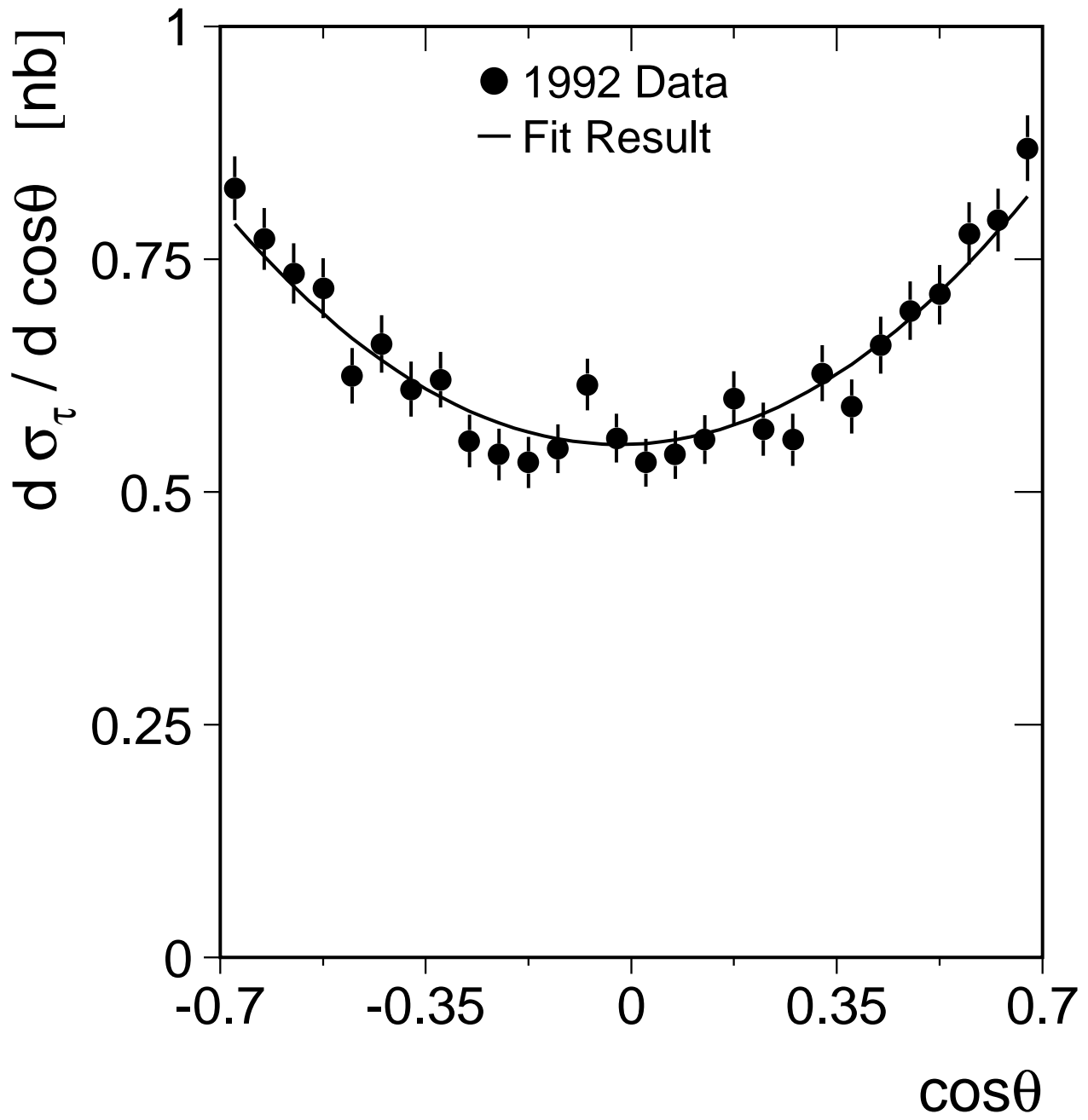


Figure 8

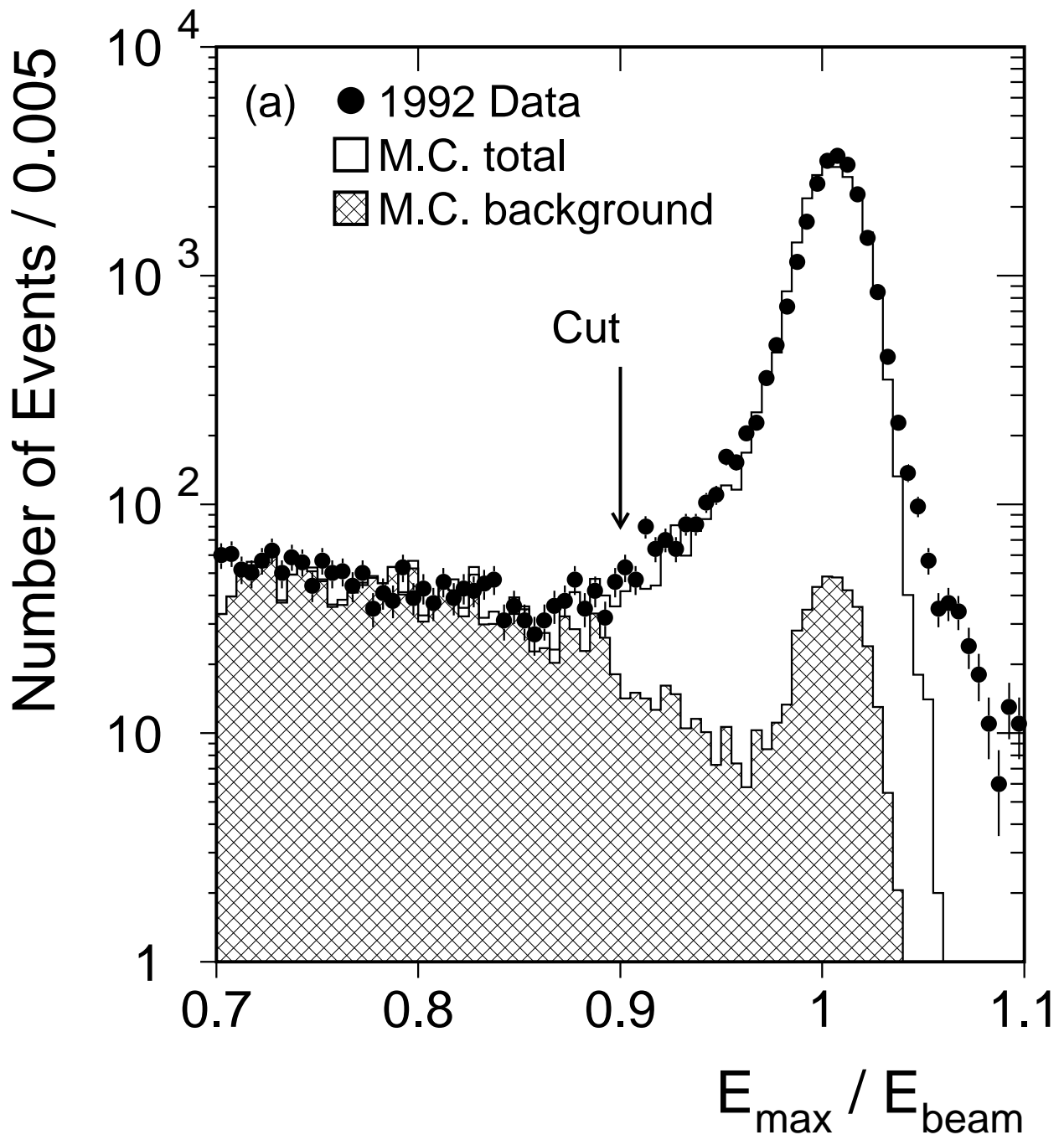


Figure 9a

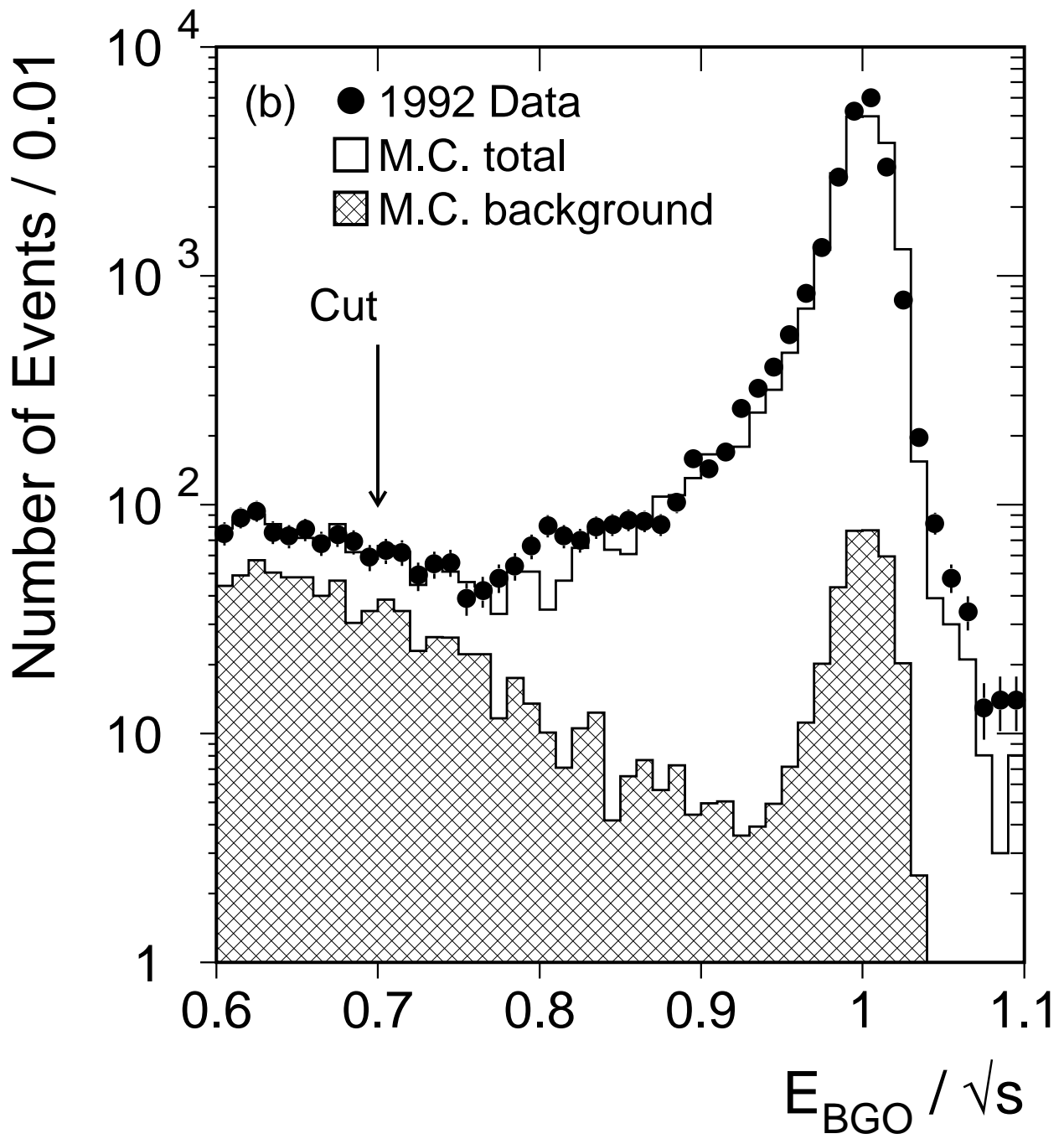


Figure 9b

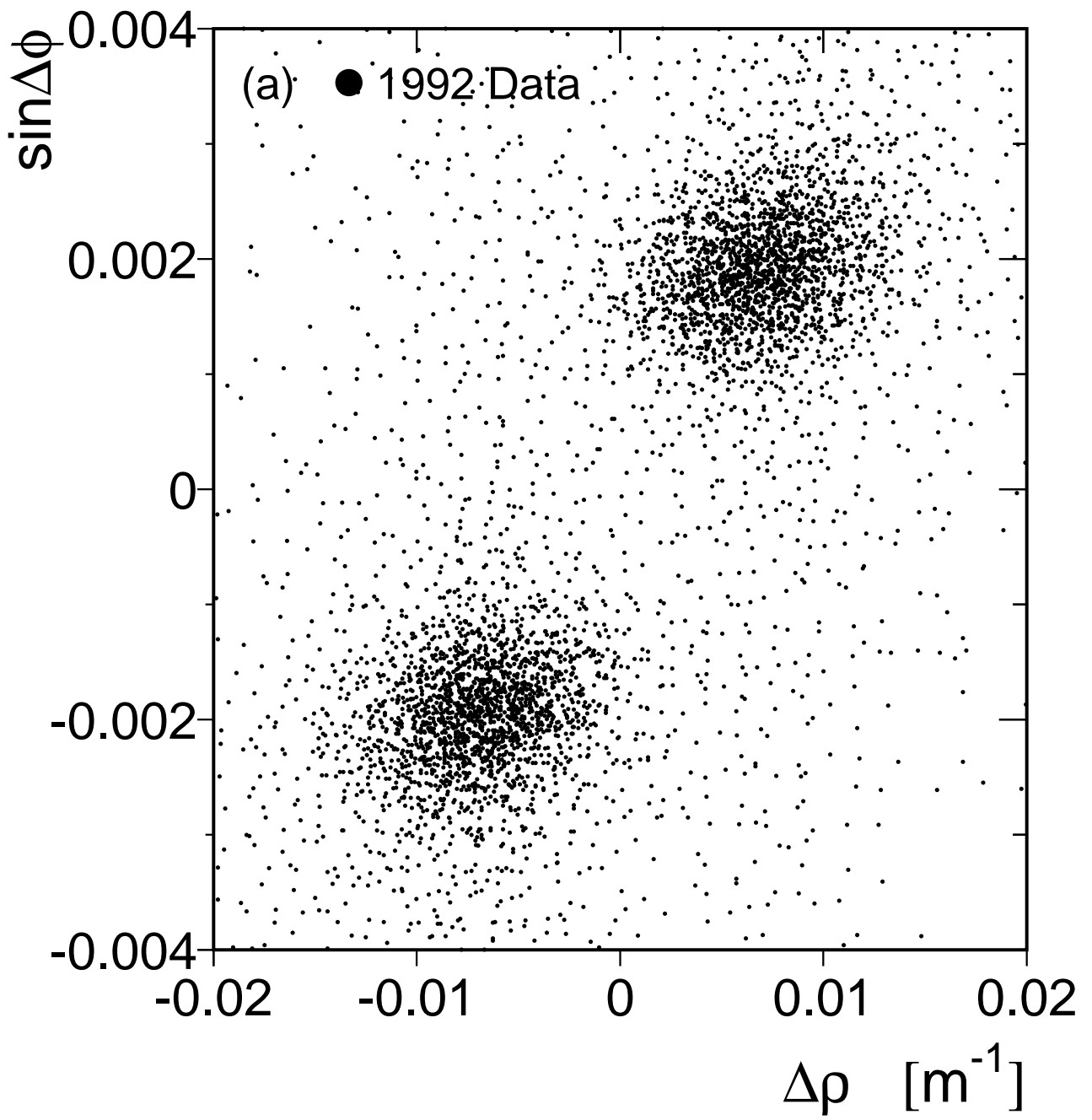


Figure 10a

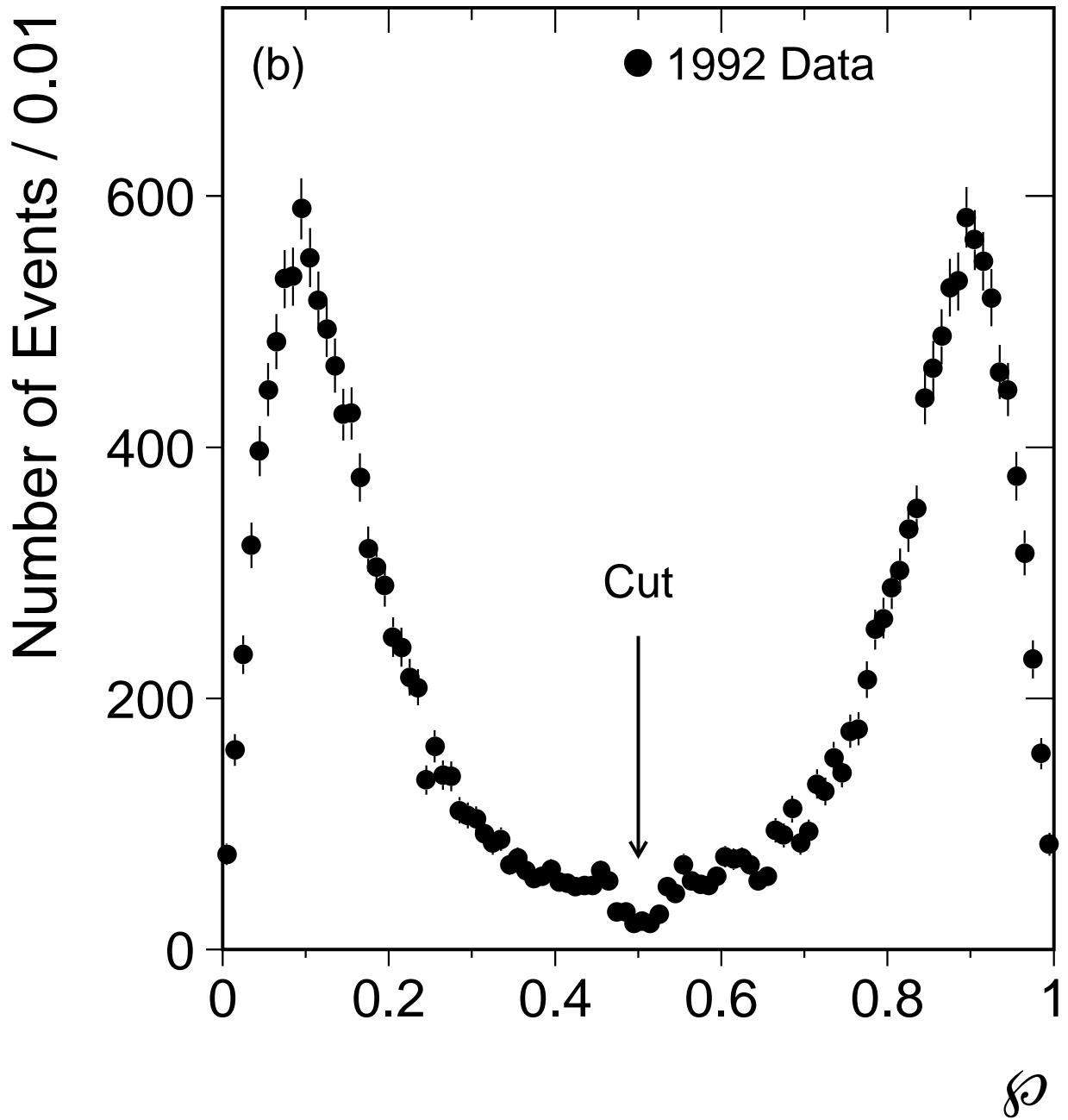


Figure 10b

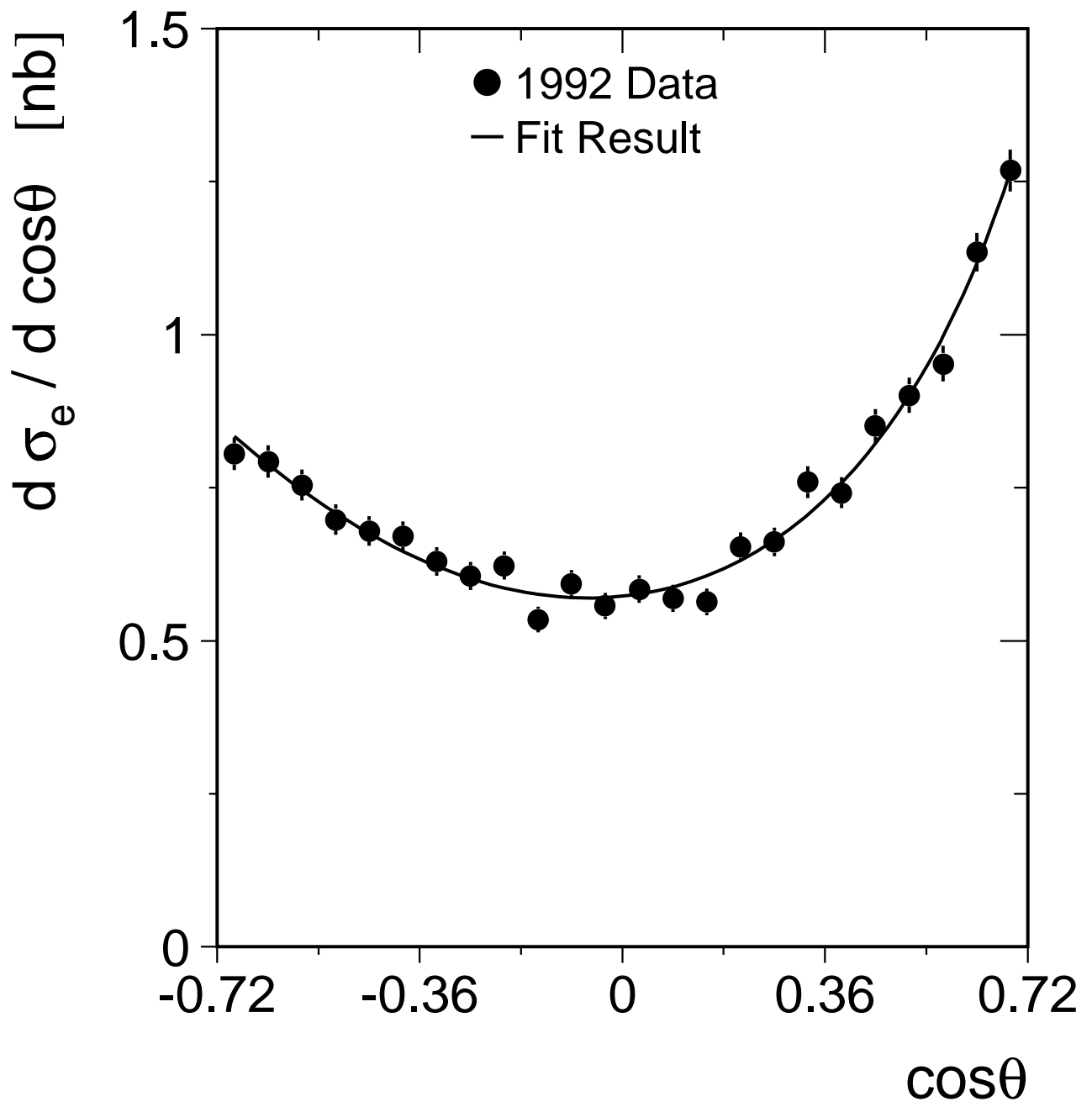


Figure 11

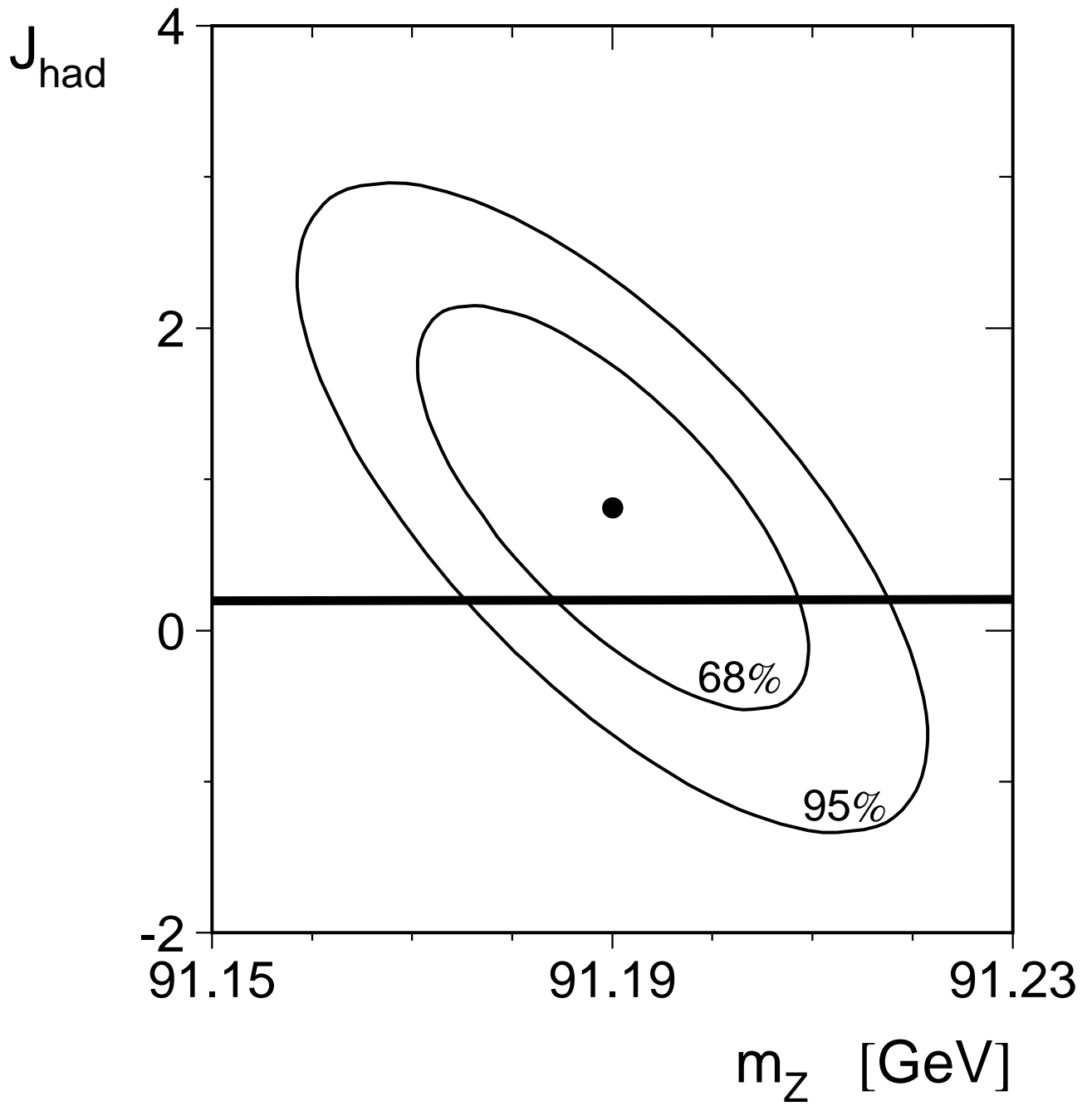


Figure 12

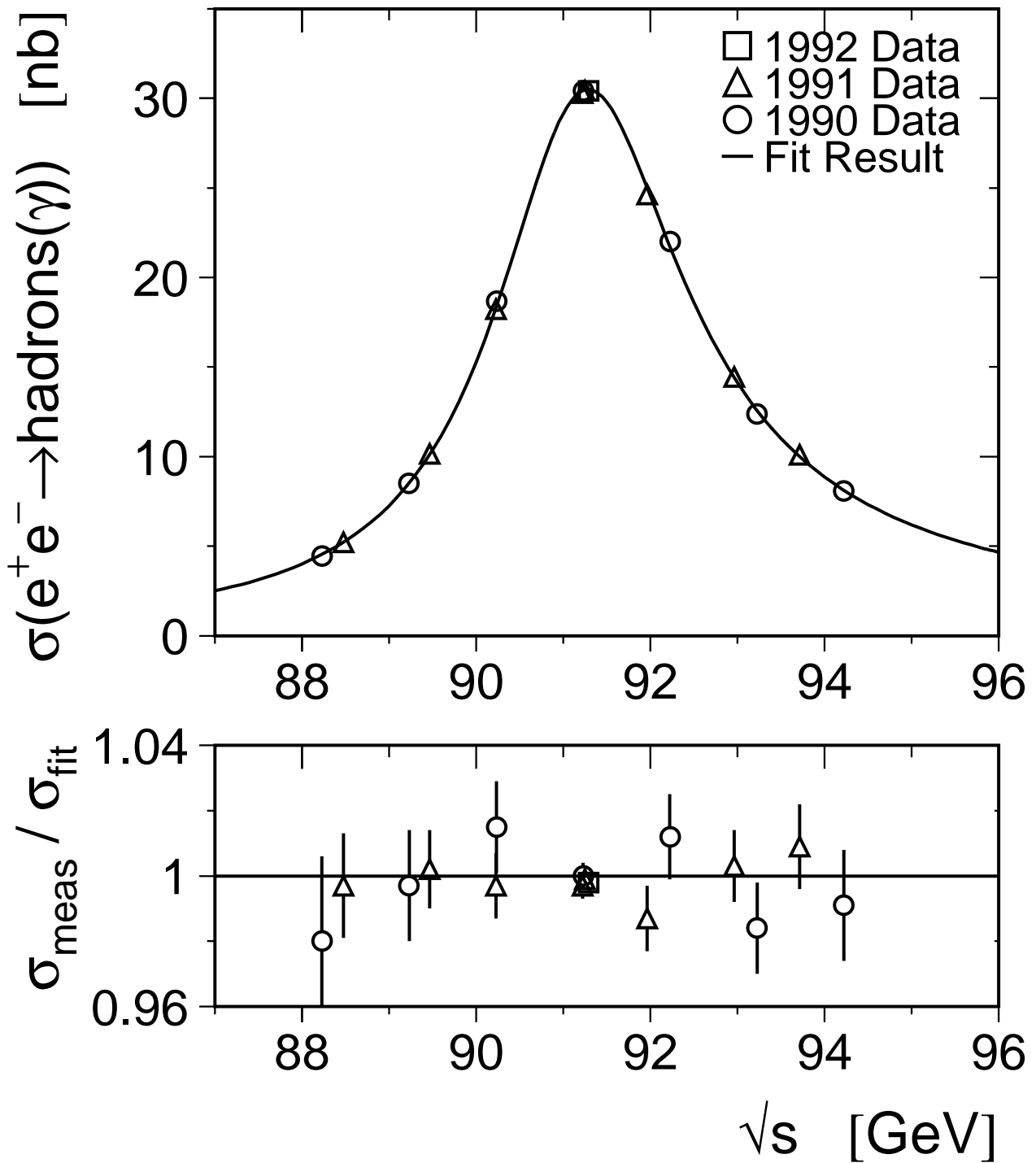


Figure 13

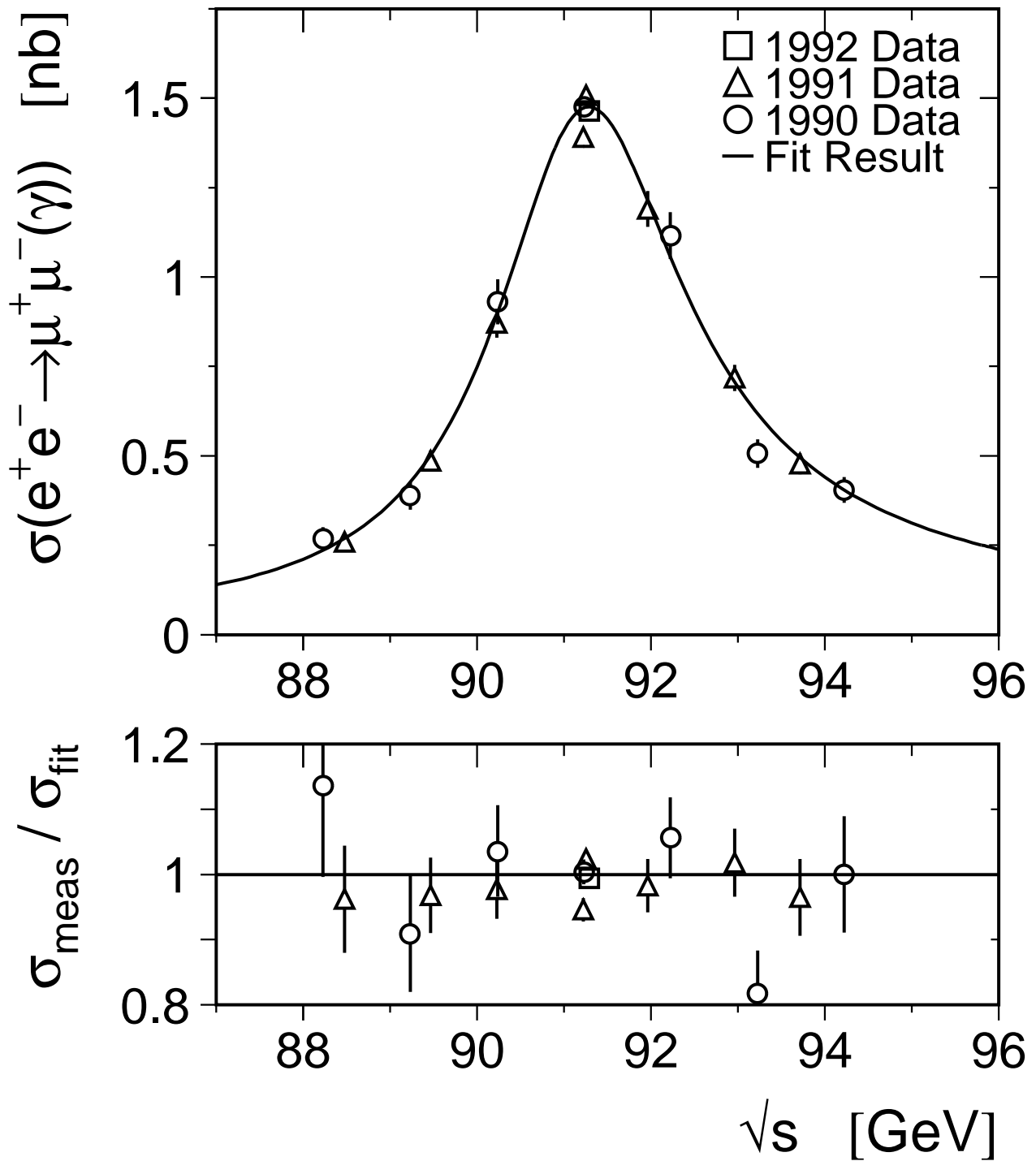


Figure 14

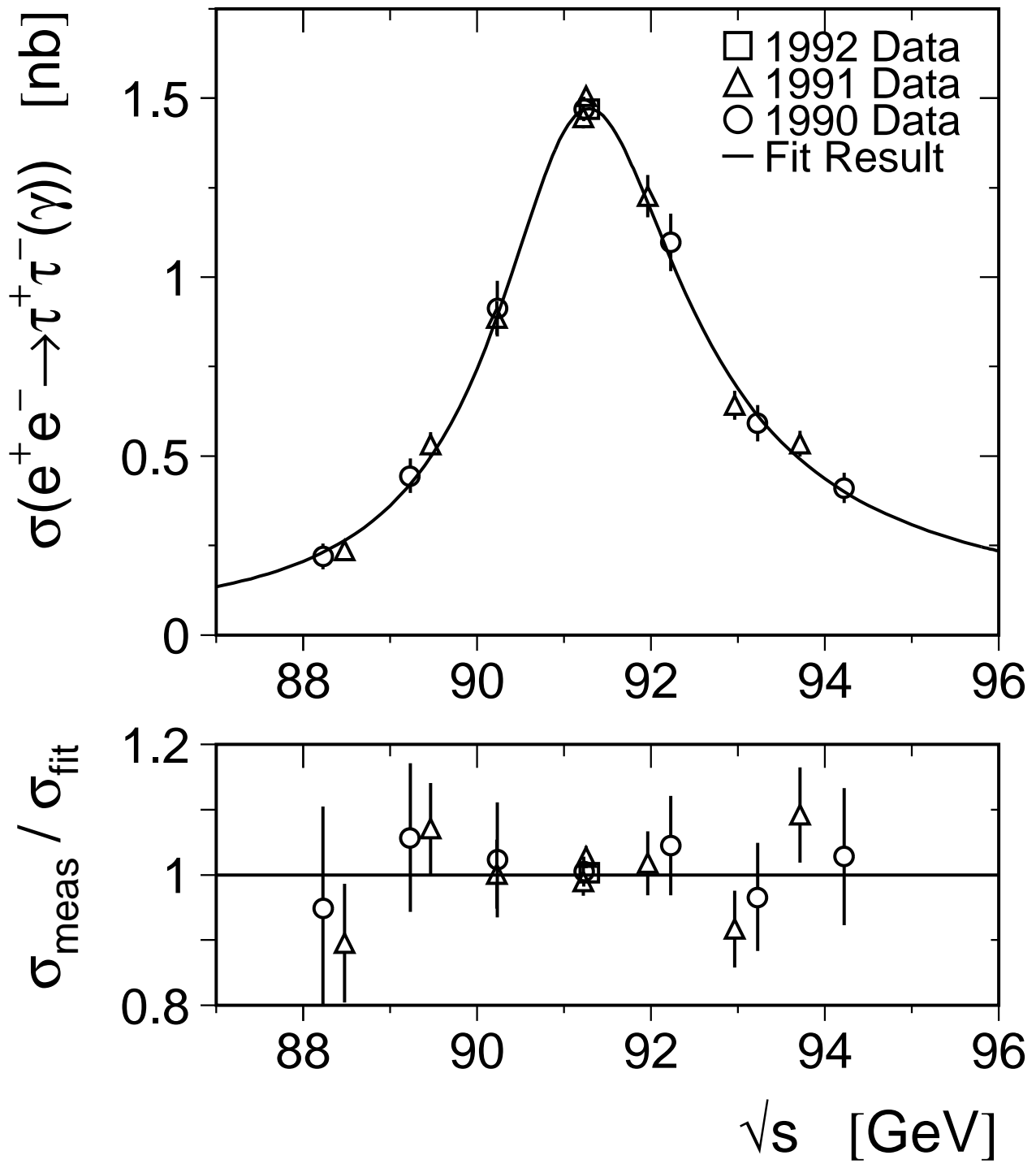


Figure 15

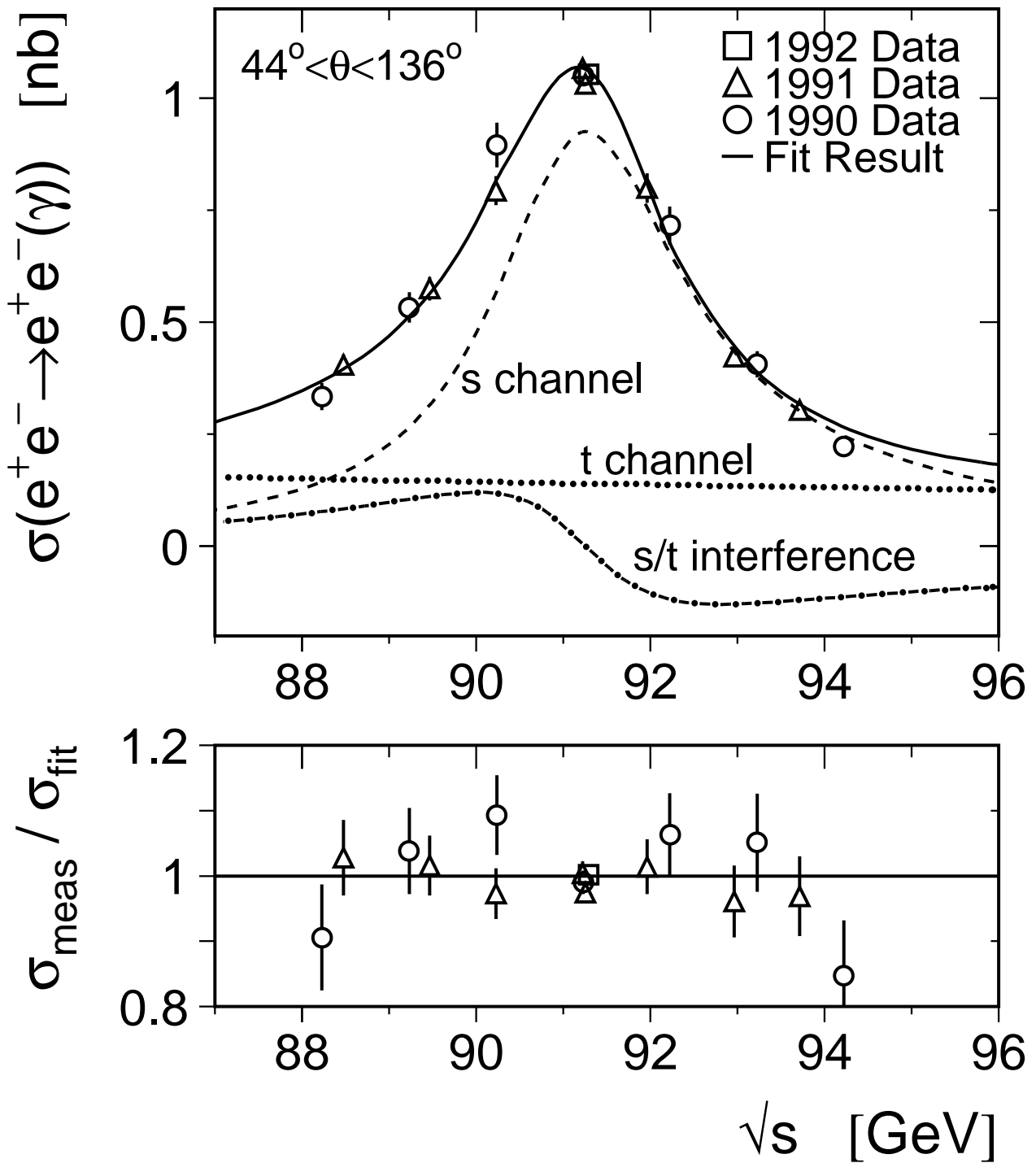


Figure 16

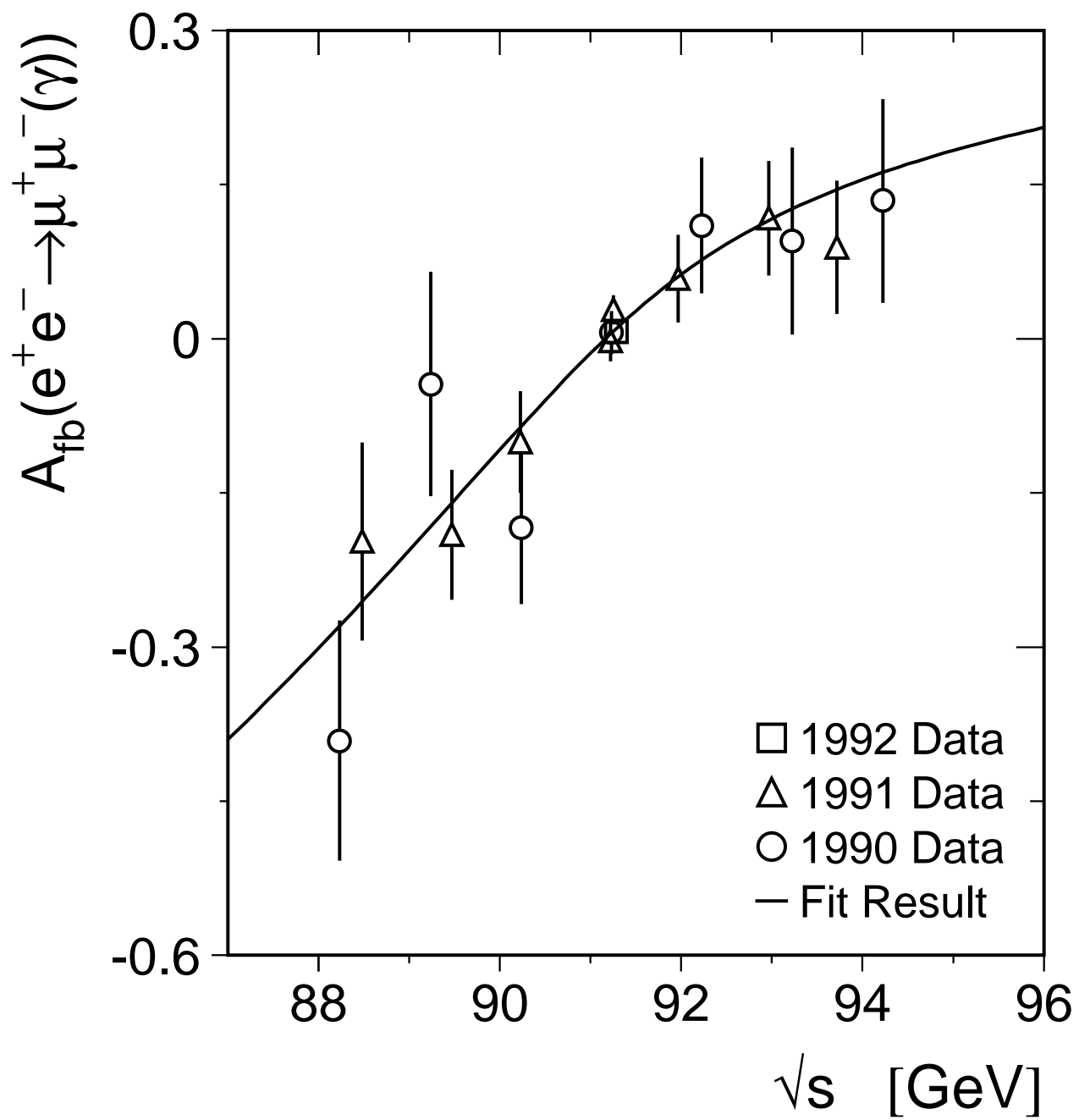


Figure 17

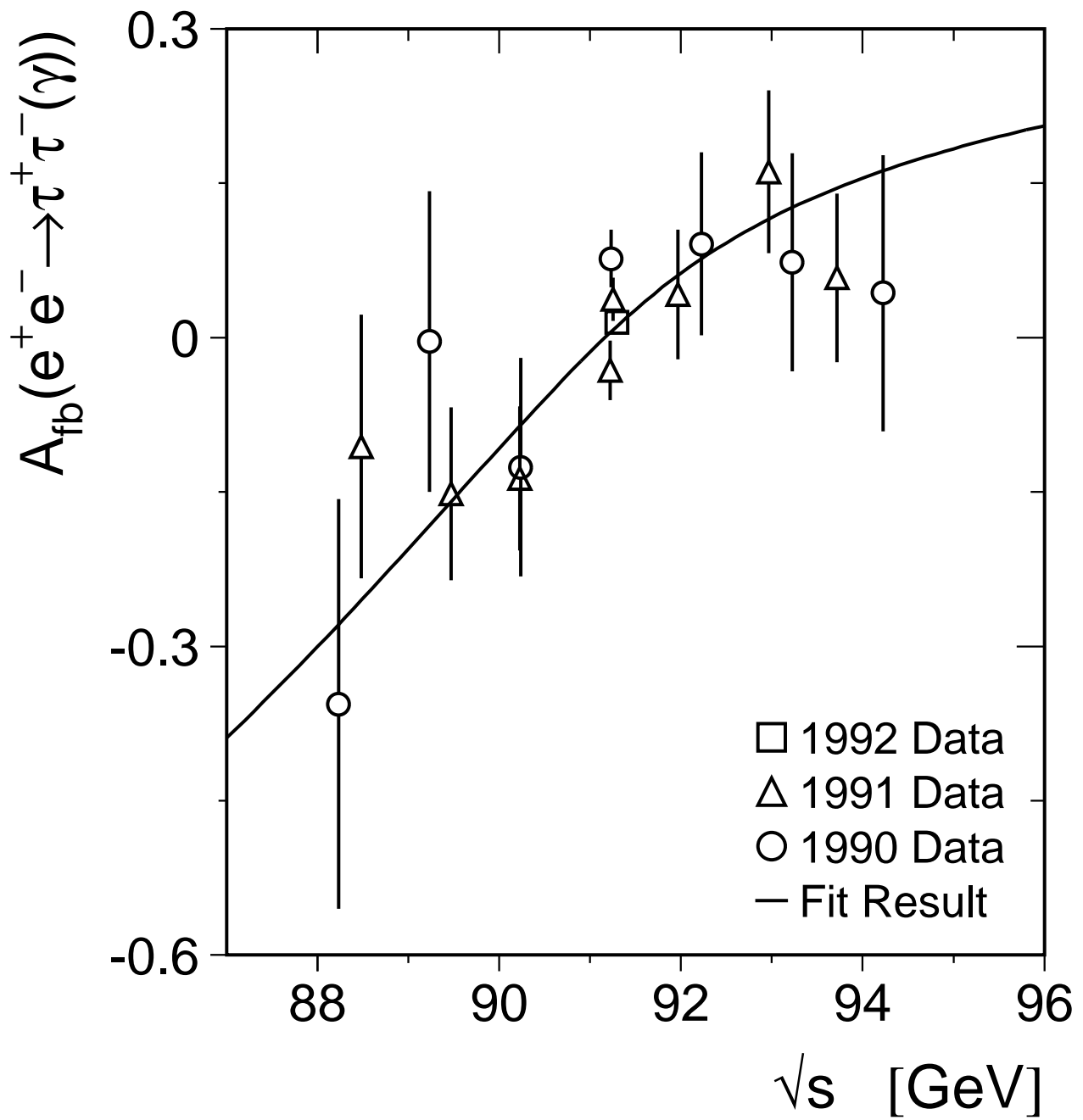


Figure 18

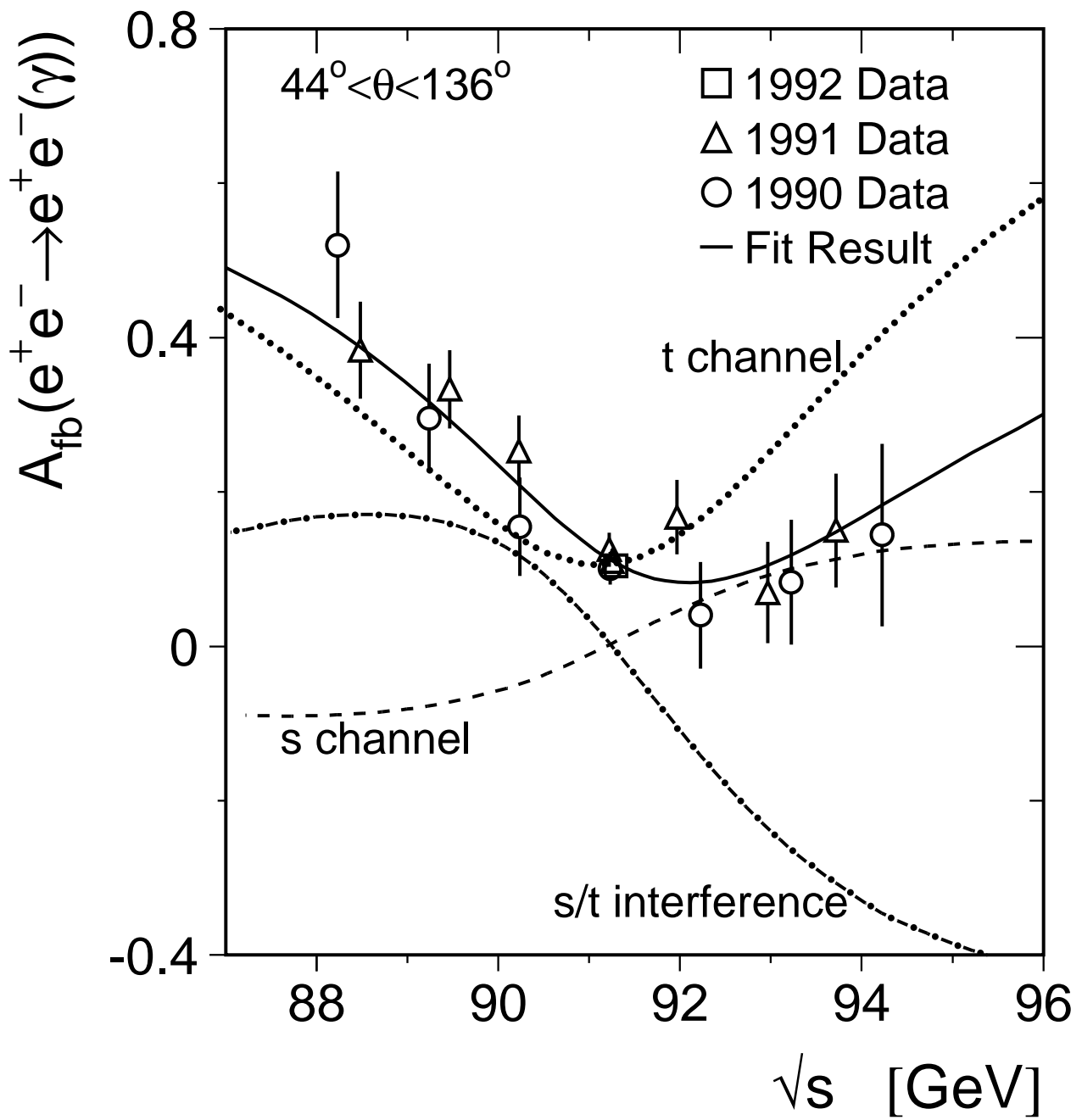


Figure 19

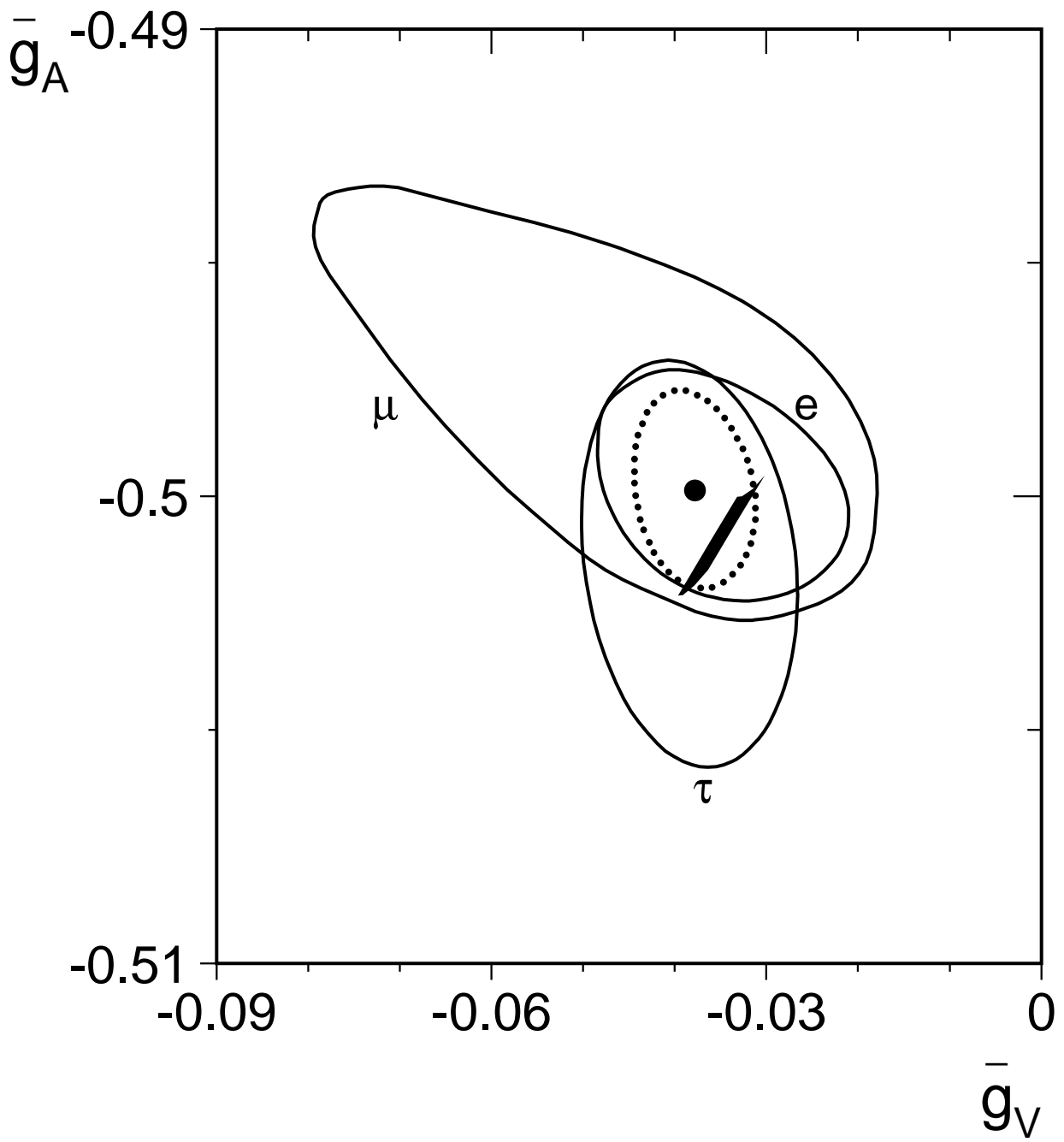


Figure 20

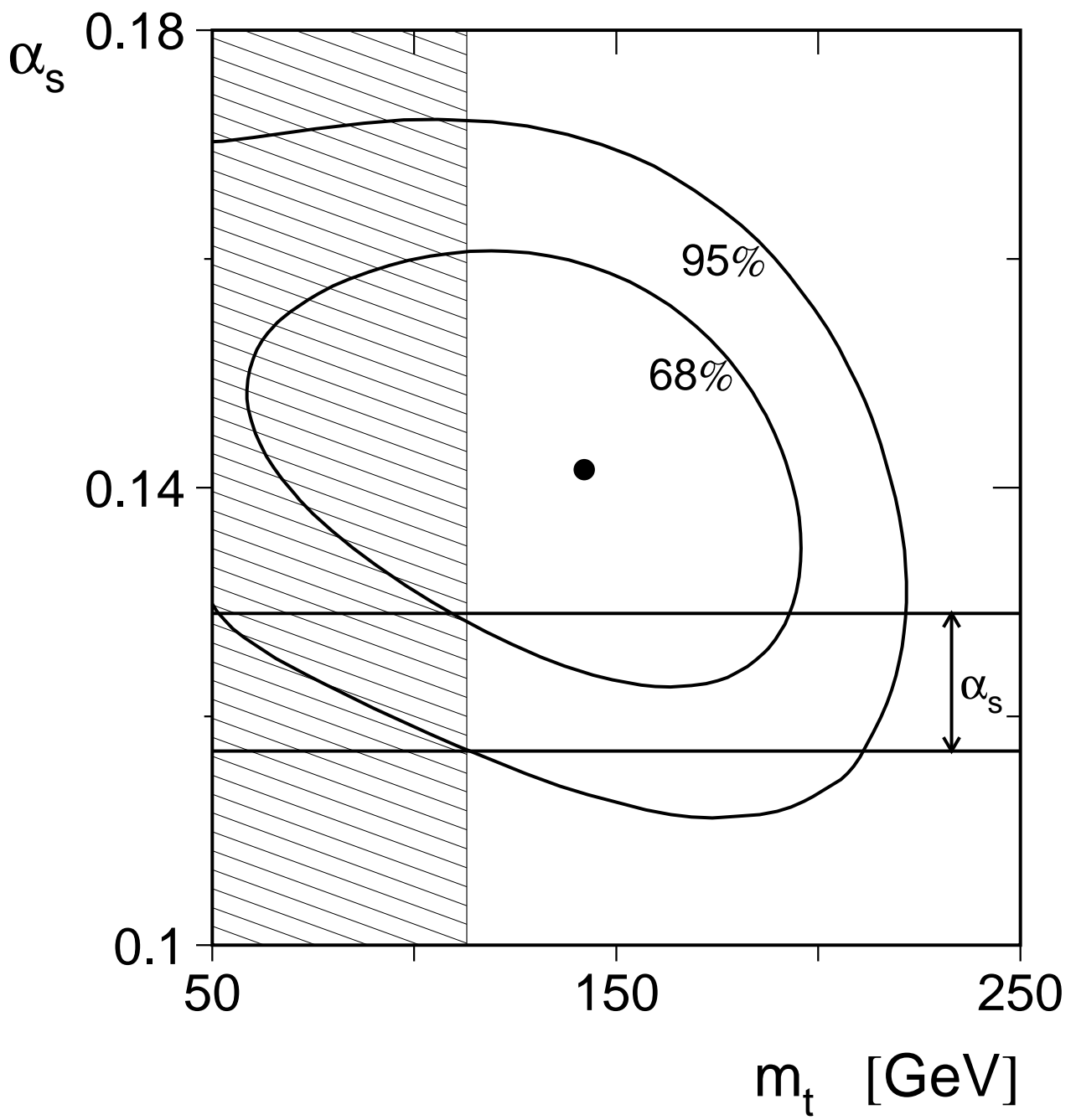


Figure 21

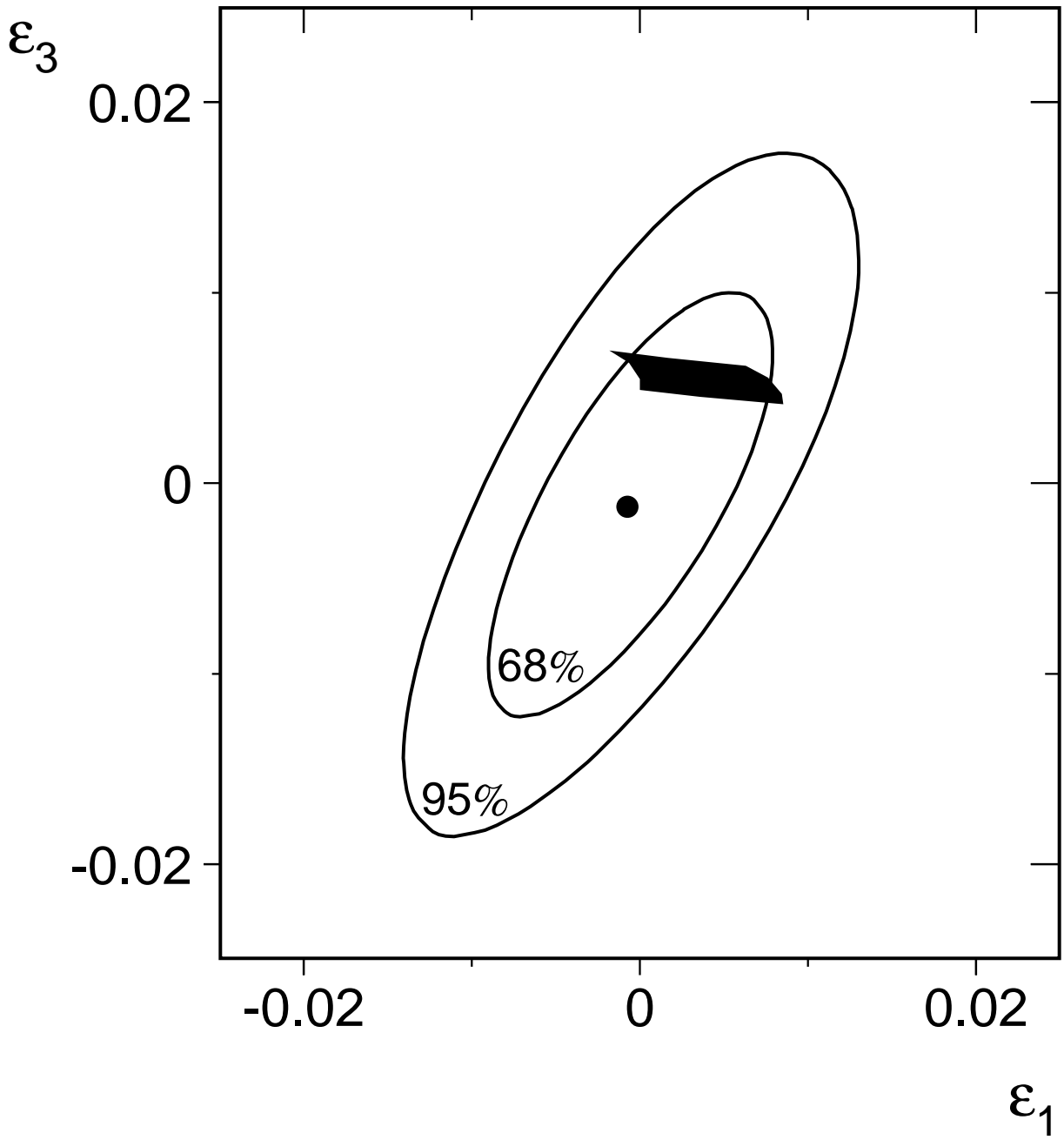


Figure 22